

NUMERICAL INVESTIGATION AND COMPARATIVE ANALYSIS OF MULTI
JET IMPINGEMENT COOLING SYSTEM WITH OPTIMIZED HEAT SINKS

A Thesis

by

PAVANROHITH GOVINDARAJU

Submitted to the Office of Graduate and Professional Studies of
Texas A&M University
in partial fulfillment of the requirements for the degree of
MASTER OF SCIENCE

Chair of Committee,	Jorge L. Alvarado
Committee Members,	Diego Donzis
	Michael Pate
Department Head,	Andreas Polycarpou

August 2021

Major Subject: Mechanical Engineering

Copyright 2021 Pavanrohith Govindaraju

ABSTRACT

In this study a multi jet array cooling device with different heat sink configurations has been proposed and optimized. The coupled effect of design parameters of jet impingement on heat transfer was studied and the usefulness of optimization schemes in the design of multi-jet manifolds and heat sinks was explored. Numerical approach using commercial CFD software Star-CCM+ was implemented and several numerous cases were simulated to understand the effects of each parameter (jet diameter, impingement height, heat sink parameters, and outlet height, among others) on heat transfer characteristics. Gradient based and Heuristic optimization techniques were used to find the optimum design for conical pin heatsink and upper manifold configuration. Topology optimization was also used on the optimal design to further enhance the heat transfer characteristics. Various designs of heat sinks were explored and compared with the base case (flat plate). Numerical results were compared with the experimental data and validated for different flow and heat flux conditions. Water was used as the working fluid both in the computational simulations and the experiments. A lowest thermal approach of 0.04 K/W was achieved at a volumetric flow rate of 2000 ml/min with a pumping power of 30 mW.

ACKNOWLEDGEMENTS

First and foremost, I would like to thank my research advisor, Dr. Jorge Alvarado for his guidance throughout my research work. Secondly, I would like to thank Nikhil Pundir, who was always available to share his knowledge.

Personally, I want to mention my friends, Syed Mohammad Hameed ul Haq and Shitiz Sehgal who kept motivating me and were always available to extend support.

Finally, I want to thank my parents Mr. Vijaykumar Govindaraju and Mrs. Sandhya Govindaraju for their continuous support and encouragement throughout my life.

CONTRIBUTORS AND FUNDING SOURCES

Contributors:

This work was supervised by a thesis committee consisting of Professor Jorge Alvarado, Professor Michael Pate of the Department of Mechanical Engineering and Professor Diego Donzis of the Department of Aerospace Engineering.

The experimental results discussed in Chapter 5 were provided by Nikhil Pundir. All other work conducted for the thesis was completed by the student independently.

Funding Sources:

Graduate study was supported by a graduate fellowship from the J. Mike Walker '66 Department of Mechanical Engineering.

NOMENCLATURE

A_b	Area of base
A_{LS}	Liquid-side surface area
c_f	Friction factor
d_j	Jet diameter
dP	Pressure drop
E	Energy per unit mass
EF	Thermal approach enhancement factor
f_b	Body forces
FS	Factor of safety
GCI	Grid convergence index
h_{LSA}	Heat transfer coefficient based on liquid-side surface area
J	Objective function
k_f	Thermal conductivity of fluid
k_{TIM}	Thermal conductivity of thermal interface material
l_{TIM}	Thickness of thermal interface material
N	Number of mesh elements
p	pressure
q	Heat flux
\dot{Q}	Heat input
r	Distance along the diagonal from the center of the heat sink
Re	Reynolds number
$R_{\theta_A}^*$	Normalized thermal approach with respect to base area

$R^*_{\theta v}$	Normalized thermal approach with respect to volume of heat sink
R_{θ}	Thermal approach
R_c	Contact thermal resistance
S	Shear stress tensor
T	Temperature
t_b	Thickness of the boundary layer
T_{bulk}	Average bulk fluid temperature
T_{in}	Fluid inlet temperature
T_{out}	Fluid outlet temperature
T_s	Surface temperature
v	Velocity
v_j	Jet velocity
\dot{V}	Volumetric flow rate
V	Volume
\dot{W}^*	Normalized pumping power with respect to base area
\dot{W}	Pumping power
x_i	Input design parameter
δ	Normalized base size of the grid
μ	Dynamic viscosity
ρ	Density
σ	Stress tensor

TABLE OF CONTENTS

	Page
ABSTRACT	ii
ACKNOWLEDGEMENTS	iii
CONTRIBUTORS AND FUNDING SOURCES.....	iv
NOMENCLATURE	v
TABLE OF CONTENTS	vii
LIST OF FIGURES	ix
LIST OF TABLES	xii
1. INTRODUCTION.....	1
1.1. Motivation	3
1.2. Research Objectives	4
2. LITERATURE REVIEW.....	5
2.1. Jet Impingement Cooling	5
2.2. Optimization studies in fluid cooled systems.....	12
2.3. State of the art jet impingement/microchannel cooling technologies	16
2.4. Knowledge gaps identified in literature	22
3. DESIGN METHODOLOGY FOR MULTI-JET COOLING SYSTEM	24
3.1. System configuration of multi jet cooling system.....	24
3.2. Problem formulation and data reduction for optimization of multi jet cooling system and comparative analysis of heat sinks	29
3.3. Model implementation algorithm.....	35
4. NUMERICAL APPROACH: COMPUTATIONAL FLUID DYNAMICS, DESIGN OPTIMIZATION, TOPOLOGY OPTIMIZATION AND GRID INDEPENDENCE STUDY	38
4.1. Computational Fluid Dynamics in Multi-jet Cooling Systems.....	38
4.1.1. CFD and its advantages in the study of multi-jet cooling systems	38
4.1.2. Governing Equations in CFD analysis:	40
4.1.3. Fluid and Solid material selection	43
4.1.4. Solver selection for multi-jet fluid simulation	45
4.1.5. Convergence criteria for numerical simulations	47
4.2. Optimization study for multi-jet fluid system.....	48

4.2.1.	Latin hypercube specification for design space of multi-jet fluid system.....	48
4.2.2.	Gaussian regression for input to output variables in multi-jet cooling system.....	49
4.2.3.	Gradient based optimization techniques (Sequential Quadratic Programming).....	50
4.2.4.	Heuristic optimization technique in multi-jet fluid system.....	53
4.2.5.	Domain selection for optimization of cone pin heat sink using genetic algorithm.....	55
4.2.6.	Mesh generation for multi-jet liquid system optimization study	56
4.2.7.	Boundary conditions for the optimization study	61
4.3.	Heat sinks comparative analysis	63
4.3.1.	Domain selection for heatsink comparative analysis	63
4.3.2.	Mesh generation for comparative analysis of heat sinks.....	64
4.3.3.	Boundary conditions for heat sink comparative analysis.....	66
4.4.	Topology optimization	67
4.5.	Methodology and algorithm for grid independence study of multi-jet impingement cooling system.....	69
5.	RESULTS AND DISCUSSION	72
5.1.	Numerical grid independence in the case of flat plate heat sink system design	73
5.2.	Experimental validation of pressure drop in case of flat plate heat sink....	75
5.3.	Validation of effectiveness of using flow distributor structure across cylindrical jets in multi-jet cooling system	76
5.4.	Parametric analysis of the conical pin heat sink in multi-jet cooling system.....	78
5.4.1.	Effect of jet diameter on thermal approach and pumping power.....	78
5.4.2.	Effect of impingement height on thermal approach and pumping power	82
5.4.3.	Effect of cone height on thermal approach and pumping power	85
5.4.4.	Effect of cone angle on thermal approach and pumping power.....	88
5.5.	Optimization analysis of conical pin fin heat sink and upper manifold....	91
5.5.1.	Single objective optimization of conical pin fin heat sink and upper manifold using sequential quadratic programming	91
5.5.2.	Multi-objective optimization of conical pin fin heat sink and upper manifold using genetic algorithm.....	93
5.6.	Comparative analysis of heat sink designs.....	96
5.7.	Topology optimization of conical pin fin heat sink	110
6.	CONCLUSIONS AND SCOPE FOR FUTURE WORK	112
6.1.	Conclusions	112
6.2.	Scope for future work.....	114
	REFERENCES	115

LIST OF FIGURES

	Page
Figure 1 Liquid cooling of electronic chips [1].....	2
Figure 2 Axisymmetric flow field formed by confined impinging jet [2]	5
Figure 3 Front and top view of jet impingement with local fluid extraction [11].....	9
Figure 4 CAD geometry of optimized heat sink [25].....	14
Figure 5 Liquid jet hierarchical manifold [30].....	16
Figure 6 Schematic diagram of a) jet impingement body cooling b) hybrid body cooling c) traditional jet impingement surface cooling [39]	19
Figure 7 Benchmarking state of the art liquid cooling systems [29]	21
Figure 8 Exploded view of the multi jet cooler assembly	24
Figure 9 Components of multi jet cooler and fluid flow path	25
Figure 10 Design parameters of the multi-jet array cooling system	33
Figure 11 Optimization algorithm.....	37
Figure 12 Standard methodology for CFD analysis.....	39
Figure 13 Latin hyper cube sampling design space for two design parameters [47] .	48
Figure 14 a) Fluid Domain b) Solid Domain	56
Figure 15 a) Fluid domain before surface mesh b) fluid domain with triangular surface mesh	57
Figure 16 Volume mesh cells.....	58
Figure 17 a) interface region with prism layer cells b) interface region without prism layer cells	59
Figure 18 Location of a) boundary conditions in fluid domain and b) solid domain; c) heat flux direction on the heat sink bottom surface.....	61
Figure 19 Components considered for comparative study of heatsinks.....	63
Figure 20 Cross section view of volume mesh generated for all heat sinks considered for comparative analysis.....	65
Figure 21 Adjoint solver-based topology optimization algorithm.....	68

Figure 22 Grid convergence index algorithm [48]	70
Figure 23 Average temperature of heat sink bottom surface with respect to number of mesh elements	74
Figure 24 Pressure drop across the multi-jet impingement cooling system with flat plate heat sink	75
Figure 25 Positions of a) jets, and b) cut section	76
Figure 26 Velocity contours of the cut section a) without flow distributor and b) with flow distributor	77
Figure 27 Variance of volumetric flow rate across the nine cylindrical jets.....	77
Figure 28 Variation of thermal approach and pumping power with jet diameter	80
Figure 29 Variation of heat transfer coefficient with jet diameter	80
Figure 30 Velocity contours of cross section for Jet diameter of a) 2 mm b) 4 mm..	81
Figure 31 Variation of thermal approach and pumping power with impingement height	83
Figure 32 Variation of heat transfer coefficient with impingement height.....	83
Figure 33 Velocity contours of cross section for impingement height of a) 3.5 mm b) 7.5 mm; Temperature contours of solid-liquid interface for impingement height of c) 3.5 mm d) 7.5 mm	84
Figure 34 Variation of thermal approach and pumping power with cone height.....	86
Figure 35 Variation of heat transfer coefficient with cone height	86
Figure 36 Velocity contours of cross section for cone height of a) 1.5 mm b) 3.5 mm; Temperature contours of solid-liquid interface for cone height of c) 1.5 mm d) 3.5 mm.....	87
Figure 37 Variation of thermal approach and pumping power with cone angle.....	89
Figure 38 Variation of thermal approach and pumping power with cone angle.....	89
Figure 39 Velocity contours of cross section for cone angle of a) 55° b) 75°; Temperature contours of solid-liquid interface for cone angle of c) 55° d) 75°	90
Figure 40 Single objective optimization with multi-start approach.....	92
Figure 41 Pareto front of multi-objective optimization of conical pin fin heat sink..	93

Figure 42 Optimized manifold and heat sink parameters using multi-objective genetic algorithm	94
Figure 43 Variation of thermal approach with respect to volumetric flow rate	97
Figure 44 Variation of heat transfer coefficient and Nusselt number with respect to Reynolds number	97
Figure 45 Surface velocity contours for different heat sink configurations for a volumetric flow rate of 600 ml/min.....	99
Figure 46 Variation of thermal approach with liquid-side surface area.....	102
Figure 47 Variation of heat transfer coefficient and Nusselt number with liquid-side surface area.....	102
Figure 48 Comparison of radially aligned and square pin fin configurations.....	104
Figure 49 Variation of heat transfer coefficient and Nusselt number with input heat flux at a volumetric flow rate of 600 ml/min	105
Figure 50 Variation of pumping power with respect to volumetric flow rate.....	106
Figure 51 Variation of friction factor with respect to Reynolds number	106
Figure 52 Variation of normalized thermal approach with respect to volumetric flow rate	107
Figure 53 Variation of enhancement factor with respect to volumetric flow rate ...	108
Figure 54 Comparison of normalized thermal approach and pumping with benchmarking data.....	109
Figure 55 Topology optimized conical pin fin heat sink	110
Figure 56 Surface temperature contours of topology optimized heat sink.....	111
Figure 57 Comparison of heat transfer coefficient in case of topology optimized heat sink for a heat flux of 15 W/cm ² and an inlet volumetric flow rate of 300 ml/min	111

LIST OF TABLES

	Page
Table 1 Heat sink designs for comparative analysis	26
Table 2 List of design parameters and bounds	35
Table 3 Design constraints	35
Table 4 Physical properties of water at 300K	43
Table 5 Physical properties of ABS at 300K used in upper and lower manifold	44
Table 6 Physical properties of copper at 300K	44
Table 7 Solver options and models used in the CFD study	45
Table 8 Solution method options used in the CFD study	46
Table 9 Gaussian Process Regression model properties	49
Table 10 Parameters used in multi-objective genetic algorithm	54
Table 11 Parameters of the surface mesh	57
Table 12 Parameters of the volume mesh	59
Table 13 Boundary conditions of fluid and solid domain	62
Table 14 Surface and volume mesh parameters in comparative analysis study	64
Table 15 Mesh count and normalized base size for grid independence study of flat plate heat sink	73
Table 16 GCI and extrapolated temperature values at various flow rates.....	74
Table 17 Comparison of optimized design vectors between sequential quadratic programming and genetic algorithm approaches.....	95
Table 18 Average fluid velocity and standard deviation at a vertical distance of 0.25 mm for a volumetric flow rate of 600 ml/min	100
Table 19 Liquid-side surface area for different heat sink configurations	101
Table 20 Comparison of radially aligned and square pin fin configurations	103

1. INTRODUCTION

The rapid increase in the spatial density of electronic devices has resulted in a dramatic increase in heat loads both at the chip and module levels, as seen in Figure 1. As a result, heat dissipation in electronic devices has become a highly challenging task. Different cooling schemes have been developed to manage thermal loads in electronic cooling systems. Nowadays, most electronic cooling systems rely on air or electronic cooling liquid as heat transfer fluids. Given the high levels of heat dissipation, the use of liquid cooled systems has become more popular and acceptable by users. However, liquid cooled systems still need to be optimized so that a greater cooling efficiency can be achieved.

Some of the most widely studied liquid cooling methods are spray cooling, microchannel flow, and jet impingement cooling. Considerable efforts have been devoted to the study of jet impingement in heat sink cooling. Recently, increased attention has been given to the study of liquid jet impingement, as heat transfer coefficient can be increased to several orders of magnitude compared to other convective heat transfer approaches. Compared with conventional convection cooling that rely on confined flow parallel to the cooled surface, jet impingement produces heat transfer coefficients that are up to three times higher at a given maximum flow, because the impingement boundary layers are much thinner. Furthermore, the radial dispersion of impinged flow could lead to flow perturbations within the surrounding fluid that enhance the overall heat transfer process. Moreover, when the jet strikes the target surface, it forms a very thin stagnation zone boundary layer, which offers little

resistance to heat flow. Jet impingement cooling also generates its own flow field, often without the need for using channels or other modifications on the heated surface.

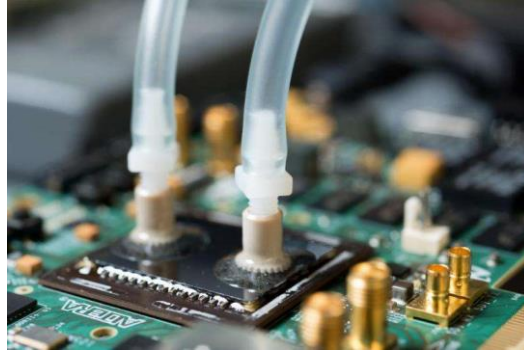


Figure 1 Liquid cooling of electronic chips (Reprinted from [1])

Liquid jets can also result in extremely high heat fluxes if the velocities are such as to produce a high stagnation pressure. They are characterized by heat transfer coefficients ranging from 10 to 100 kW/(m²K) for single phase jets. Two types of jets used in cooling are: free surface liquid jets and submerged jets. In this study submerged jets were considered since electronic systems should not be exposed to any liquids directly

With the advancements in additive manufacturing techniques, the targeted surface or heat sink can be modified and reconfigured with the goal of enhancing the overall heat transfer performance. Additive manufacturing or 3D printing is regarded as a promising technique for fabricating complex geometries that enable the implementation of intricate designs with complex internal geometries in jet impingement coolers. Therefore, the study of the interactions of liquid jets with modified 3D printed heat sinks should be pursued.

1.1. Motivation

Jet impingement cooling is widely used in many industrial systems such as gas turbine cooling, laser cooling, sheet metal industry and rocket launcher cooling. In conventional jet impingement schemes, jets of liquid impinge on a heated surface. In most common configurations, the heat transfer fluid flows over the surface and exits through the sides of the array. In such configurations, many factors affect the performance of jet impingement arrays, including the inter-jet spacing, jet diameter, and height of impingement. For jets starting at a considerable height above the target, the kinetic energy of the jet diminishes as it travels to the surface, resulting in over a 20% reduction in the average Nusselt number. At small spacings, jet-to-jet interactions may result in lower heat transfer efficiencies. Also, interference between closely spaced jets can also reduce the impinging velocity, thereby decreasing the overall heat transfer rate.

Effect of these parameters has been studied individually but limited research results are available for their combined effects on heat transfer performance of systems that make use of jet impingement arrays. Therefore, understanding the combined effects and designing an optimized system, which considers the overall thermal performance should be pursued. Therefore, the current study of jet impingement heat transfer focuses on optimizing the manifold configuration and heat sink topology to develop an optimal heat transfer system for electronic cooling.

Computational Fluid Dynamics (CFD) simulations offer a myriad of benefits in the analysis of jet impingement cooling. CFD may be used to obtain a better insight into flow patterns that are difficult to study using experimental techniques. Furthermore, CFD allows for the exploration of different design variables without

having to rely on experimental methods. CFD also reduces the number of experiments and overall cost with data generation and collection, and instrumentation. In summary, a CFD study has been undertaken to investigate numerically the heat transfer characteristics of jet impingement cooling with different optimized system designs.

1.2. Research Objectives

The main objective of this study is to understand the combined effect of design parameters of jet impingement on heat transfer while exploring the usefulness of optimization schemes in the design of multi-jet manifolds and heat sinks. To achieve these objectives, numerous cases were simulated using commercial software Star-CCM+ to understand the effects of each parameter (jet diameter, impingement height, heat sink parameters, and outlet height, among others) on heat transfer characteristics. Once the design space was explored and major design parameters were identified, the objective functions – thermal approach (indicates the overall thermal resistance of the system) and pumping power were minimized using the heuristic technique (Multi objective genetic algorithm). The overall goal was to maximize heat transfer while keeping the pumping power to a minimum.

Topology optimization was also used on the optimal design to further enhance the heat transfer characteristics of the system. Various designs of heat sinks were explored and compared with the base case (flat plate). Numerical results of pressure drop were compared with the experimental data and validated for different fluid flow conditions. Water was used as the working fluid both in the computational simulations and the experiments.

2. LITERATURE REVIEW

Based on the study objectives mentioned in Chapter 1, a survey of the existing literature has been conducted, which includes literature review of jet impingement cooling, optimization studies and state of the art liquid cooling technologies. Knowledge gaps in the current literature were also identified, which are discussed in this chapter.

2.1. Jet Impingement Cooling

Impinging jets have been used in very diverse applications in industry. Recently, liquid jet impingement has been considered for use in the cooling of electronic components. Increased power densities per device have necessitated the search for innovative techniques of heat dissipation. Numerous studies have been carried to understand the thermal-fluid behavior of impinging jets. For instance, axisymmetric flow field in a confined jet impingement case was studied by Guo *et al.* [2]. They undertook a detailed investigation of the influence of confinement on the flow field and radial wall jet development. The conducted research was among the first studies of the effect of confinement on self-similar structure of a radial wall jet.

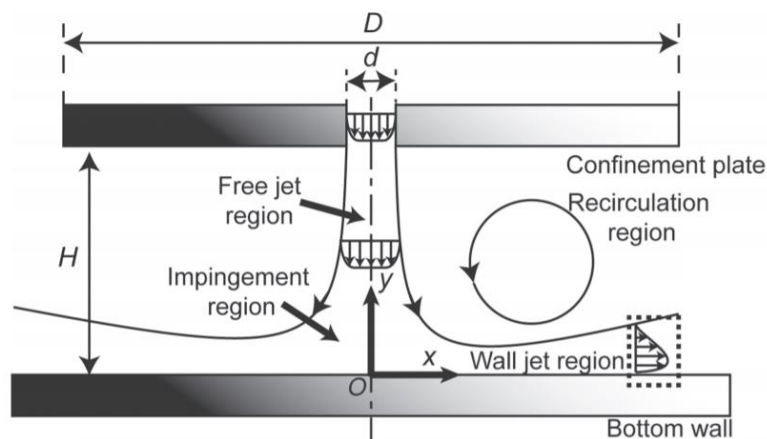


Figure 2 Axisymmetric flow field formed by confined impinging jet

(Reprinted from [2])

Since then, experimental, and numerical investigations of flow and heat transfer characteristics under single and multiple impinging jets have remained a very dynamic research area. Several design parameters such as jet-to-target plate spacing, nozzle diameters, jet-to-jet spacing in case of multi jet impingement, shape of the nozzles, and several target plate configurations were studied and discussed in the literature. Garimella *et al.* in [3] conducted experiments to determine the effect of nozzle geometry (diameter and aspect ratio) on the local heat transfer coefficients for a confined submerged liquid jet of FC-77. A single jet with hydraulic diameters ranging from 0.79-6.35 mm and different aspect ratios ranging from 0.25-12 were tested. It was observed that the local heat transfer coefficients were higher for smaller aspect ratios (<1). As the aspect ratios increased from 1 to 4 the heat transfer coefficient (htc) values dropped sharply. Further increasing the aspect ratio from 8 to 12, the htc values gradually increased. The possible explanation for this is the flow separation at the nozzle entrance and its effect on the exit velocity profiles.

Similarly, numerical studies were also conducted by Ibrahim *et al.* [4] for jet impingement over solid surfaces. Different design parameters such as jet-target spacing, and jet diameter were considered for flat, convex, and concave shaped target plates. κ - ϵ , κ - ω and v^2f models were compared with experimental data available in the literature to determine their heat transfer effectiveness.

Heat flux uniformity is also an important factor in reducing the hotspots on the target surface. Forouzanmehr *et al.* [5] developed a numerical algorithm to obtain an optimized array of four laminar impinging slot jets. Root mean square deviation of Nusselt number was considered as the objective function. Jet width, jet-to-jet, jet-to-surface spacing, and overall flowrate were considered as design variables. The

numerical study was verified with experimental results using Mach-Zehnder interferometer. Nozzle geometries also play a critical role in maintaining the uniformity of surface temperatures on the target heat sink. Wen *et al.* [6] conducted a comparative study to determine the effects of nozzle geometry and arrangement effects on impinging jets heat transfer to help design a ground fast cooling device. SST κ - ω turbulence model was used in their CFD analysis. Various nozzle shapes such as circular, square, elliptical, cross and a combination of all the configurations were considered in the optimization study as well. A performance factor based on average surface heat flux, normalized extreme heat flux differences and standard deviation of the surface heat flux was considered for the objective function.

In addition to uniformity in heat transfer characteristics, nozzle shapes also contribute to the enhancement in heat transfer. Rau *et al.* [7] measured heat transfer distributions under confined impinging jets from a cross shaped orifice. It was observed that in a single-phase operation, coolest surface temperatures correspond to areas with high liquid velocities. Cross shaped orifices were found to achieve local heat transfer coefficients that exceeded the corresponding stagnation point value of a circular jet of equivalent cross-sectional area by up to 1.5 times with an increase in pressure drop of only 1.1 times of circular jet cases.

Choo *et al.* in [8] investigated heat transfer and fluid flow characteristics of a submerged jet impingement on a flat plate. Air and water were used as working fluids. The effects of nozzle-to-plate spacing ($H/d = 0.1 - 40$) on the Nusselt number and stagnation pressure were considered. It was observed that Nusselt number and pressure characteristics could be categorized into three different regions namely, jet deflection region ($H/d \leq 0.6$), potential core region ($0.6 \leq H/d \leq 7$) and free jet region ($H/d > 7$).

The study revealed that Nusselt number and stagnation pressure drastically increased with decreasing nozzle-to-plate spacing. In region 2, that effect was found to be negligible. In region 3, the Nusselt number and pressure monotonically decreased with increasing nozzle-to-plate spacing.

In addition to heat transfer enhancement, another important factor in jet impingement cooling is the pressure drop across the system. Several studies were conducted using nozzles with the aim of reducing pressure drop. For example, Brignoni *et al.* [9] studied the effects of nozzle inlet chamfering on pressure drop and heat transfer in confined air jet impingement. Chamfered nozzles were compared with square edged nozzles of the same diameter. The heat transfer coefficient and pressure drop enhancements were found to increase by as much as 30%. Moreover, the best performance was found using a nozzle with narrow chamfering (low angle chamfer).

Another interesting study involving the effects of extended jet holes (i.e., hollow cylinders instead of using a flat orifice plate) on heat transfer performance were conducted by Tepe *et al.* [10]. Results showed that average Nusselt numbers on the rib roughened surface could be increased up to 40% by using hollow cylindrical or extended jet holes to generate liquid jets before the fluid impinged on the target surface.

One of the advantages of using jet impingement cooling is the increase in heat transfer performance near the stagnation region. This advantage can be further exploited by relying on local fluid extraction near the heat sink region. In this regard, Bandhauer *et al.* [11] developed a micro jet impingement device with parallel inlet and outlet ports as shown in Figure 3. Impinging jets with a diameter of 300 μm , jet height-to-diameter ratio of 2.5, and jet spacing-to-diameter ratio of 8 were considered.

Heat transfer coefficients as high as $30 \text{ kW}/(\text{m}^2\text{K})$ were observed for a flow rate of 1 LPM.

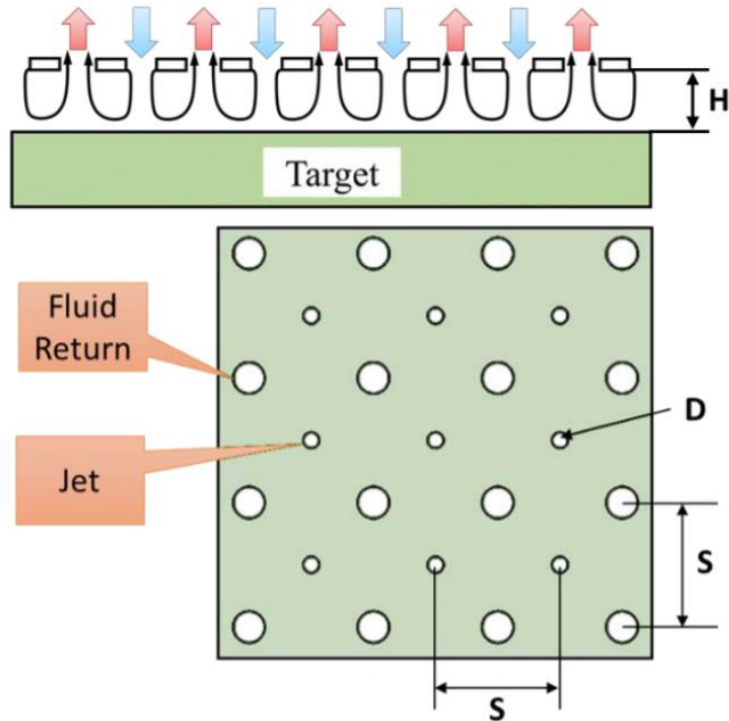


Figure 3 Front and top view of jet impingement with local fluid extraction (Reprinted from [11])

This was also studied by Rattner *et al.* [12] who performed a general characterization of jet impingement array heat sinks with interspersed fluid extraction. Numerical simulations were performed for a range of Reynolds numbers and geometries. The results were compared with micro channel heat sinks and conventional co-flow jet impingement heat sinks. Interspersed fluid extraction geometry was found to have lower pressure drop and lower average surface temperatures compared to the other two cases.

Target plate or heat sink design also plays a major role in the heat transfer enhancement in addition to jet or nozzle design parameters. Several studies have been conducted with various heat sink configurations, most of which focused on ribbed or pin fin heat sinks. Ndao *et al.* [13] conducted an experimental investigation on a single-phase jet impingement system with smooth and micro pin fin structures using water and R134a. The experiments were carried out for a single jet of 2 mm diameter over a wide range of Reynolds numbers. Micro pin fins with diameters as low as 125 μm and heights of 230 μm and pitch of 250 μm were fabricated. Enhancement factors as high as 3 or 200% increase in heat transfer coefficients were observed.

With the introduction of pin fins in heat sinks, the arrangement of the pin fins (in line with the jet arrays or offset or staggered to jet arrays) also affects the overall thermal performance of cooling systems. Andrews *et al.* [14] also studied the effect of impingement pitch-to-hole diameter ratio on heat transfer characteristics in the case of rib obstacle (rectangular pin fin) heat sink. It was observed that the in-line jets (pins found below the impinging jets) had significantly better heat transfer characteristics than offset jets because of the better surface coverage with the impingement flow.

Wiriyasart *et al.* [15] conducted a study to investigate the cooling performance of liquid jet impingement of a cold plate heat sink with different fin geometries. Rectangular, circular, and tapered heat sinks were considered as part of a parametric analysis study. It was observed that irrespective of the pin fin shape, the larger heating area had a significant effect on the heat transfer rate.

Similarly, Dobbertean *et al.* [16] conducted a numerical study of steady state heat transfer for jet impingement on patterned surfaces. Comparison of different rectangular step and triangular rib configurations were conducted. The effect of using

different plate materials were also explored for rectangular step cases. It was observed that increasing the indentation depth for the rectangular surface led to a decrease in local heat transfer coefficient whereas for the triangular patterns, a higher depth resulted in higher heat transfer coefficients. Although the thermal conductivity of the plate has an impact on the temperature of the plate, in thin plates thermal conductivity did not play a significant role in the temperature distribution within the material.

A simple case of cone heat sink with a single air jet was studied numerically by Tang *et al.* [17]. SST κ - ω turbulence scheme was validated and adopted in their study. Flow and thermal performances were investigated with the Reynolds numbers ranging from 5000 to 23000 and cone angles ranging from 40°-70°. It was found that the average Nusselt numbers were higher in a conical protuberance than in flat plates. The maximum increase was 14 % when the cone angle was set at 60° and Reynolds number is 23000.

In general, recent experimental and numerical studies have revealed that the performance of cooling systems that make use of liquid jets is superior when compared with other cooling strategies. Studies have shown that several design and flow parameters affect the performance of jet impingement cooling systems. Most of the studies focused on their individual effects. Future studies should consider the coupled effect of design parameters to provide a better understanding into the complex physics of jet impingement cooling.

2.2. Optimization studies in fluid cooled systems

Due to the complex nature of the jet impingement cooling, several factors affect the overall performance of such cooling systems. Each design variable such as parameters related to jets or orifices, parameters related to target heat sink, have a significant effect on the thermal and flow characteristics. The need for optimizing the design variables and producing an optimal design have been pursued by many researchers. Below are some examples of optimization studies present in the literature.

Ramphueiphad *et al.* [18] performed a multi objective optimization of a multi cross section pin fin heatsink for use in electronic devices. Junction temperature and fan pumping power were considered as objective functions in the optimization study.

A silicon based micro jet impingement heat sink was developed and studied by Husain *et al.* [19]. Pressure drop and thermal characteristics were studied numerically through parametric and optimization analysis. Arrays of micro jets (2x2, 3x3, 4x4, staggered) with nozzle diameters ranging from 50 μm to 100 μm were analyzed at various flow rates and heat inputs. Optimization of the nozzle array with 3 parameters were conducted and a configuration with 13 jet arrays was found to exhibit optimum thermal and pressure drop characteristics.

Shah *et al.* [20] conducted a numerical study to optimize the fin shape of jet impingement heat sinks. Seventeen different designs were compared, and an optimum shape was reported. It was found that a stepped heat sink could result in a lower die temperature compared to a parallel fin heat sink.

Among various optimization techniques, the genetic algorithm is one of the most popular used optimization algorithms because of its ability to optimize multiple

objective functions. Yang *et al.* [21] considered hybrid linked jet impingement cooling channels, which involved both parallel linked jets and serial linked jets. Systematic analysis was conducted using CFD and response surface methodology was used to focus on the influence of topology on the performance. It was observed that among the tested topologies, serial linked jet design had significantly higher heat transfer and pressure drop than the traditional parallel linked jet impingement.

Similarly, Ndao *et al.* [22] presented a multi objective thermal design optimization and comparative study of electronics cooling technologies. The cooling technologies considered were, continuous parallel micro channel heat sinks, in-line, staggered circular pin-fin heat sinks, offset strip fin heat sinks, single and multiple submerged impinging jets. Water and HFE-7000 were used as coolants. MATLAB's multi-objective genetic algorithm was utilized to determine the optimal design of each technology based on thermal resistance and pumping power. It was observed that, in general, the offset strip fin heat sink outperformed the other cooling technologies. It was concluded that even though jet impingement cooling gives high heat transfer coefficients, to exploit the full potential of the technology, it should be coupled with sufficiently large heat transfer surface area, A , and a high value of the convective heat transfer coefficient, h (i.e., the product of $h \cdot A$ should be as large as possible).

Yildizeli *et al.* [23] conducted a multi-objective genetic algorithm-based optimization study on a pneumatic contactless levitation system utilizing impinging jet arrays. Three design parameters with temperature and pressure drop as objective functions were considered.

Optimization of heat sink parameters were also studied and discussed in literature focusing on pin fin heat sinks. Yang *et al.* [24] conducted a numerical study

and optimization of pin fin heat sink with non-uniform fin height design. It was concluded that an adequate non-uniform fin height design could decrease the junction temperature and increase the enhancement of the thermal performance simultaneously. The results also showed a potential for optimizing the non-uniform fin height design.

Another evolving area of research involves the use of topology optimization for heat sink designs. This is a numerical approach where the optimizer generates geometries based on an objective function, which includes minimization of the thermal resistance or pumping power in a cold plate as a performance objective. Dede *et al.* [25] conducted a topology optimization and experimental testing of an air-cooled heat sink. A post processing procedure was used to obtain an optimal manifold. A prototype structure was fabricated out of AlSi₁₂ using additive manufacturing. The CAD geometry of the optimized heat sink is shown in Figure 4.

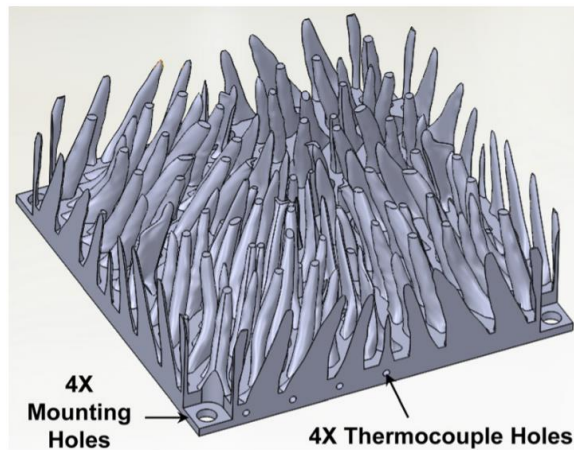


Figure 4 CAD geometry of optimized heat sink (Reprinted from [25])

Similar study was conducted by Koga *et al.* [26]. Topology optimization was applied to a domain, to obtain an optimized channel based on a given multi objective

function that combined pressure drop minimization and heat transfer maximization. The topology optimization procedure implemented in this study [26] combined the finite element method and sequential linear programming.

Similarly shape optimization of a multi jet array cooling system with a dimpled pin heat sink was conducted by Negi *et al.* [27]. Bezier polynomial formulation was incorporated to generate profile shapes for the dimples. Commercial software Star-CCM+ was used to conduct the CFD analysis. Three different turbulent simulation schemes namely, κ - ϵ , SST κ - ω and v^2f were used and it was found that SST κ - ω showed a consistent agreement with the experimental data in predicting Nusselt number. The optimized profile was found to be sensitive to jet-to-plate spacings. Hence there is a need to consider the effect of manifold parameters in the heat sink geometry optimization study.

A Multiphysics topology optimization method was conducted by Dede *et al.* [28]. Multiple surface topologies were utilized as building blocks in the development of three-dimensional cooling structures. COMSOL Multiphysics software was used to perform the topology optimization study. Conjugate heat transfer and fluid flow results indicated that the optimized jet impingement surface reduced device temperature at the cost of increased pressure drop since the study was conducted using a single objective function.

Parametric and topology optimization of manifold and heat sinks have been studied by others as shown in the literature [18-28]. However, most of them have focused on air cooling systems and microchannels in case of liquid cooling systems. In addition to the papers presented above, several studies on hybrid cooling technologies such as the use of both jet impingement and microchannel trenches can

be found in the literature. Such systems and their practical applications are discussed below.

2.3. State of the art jet impingement/microchannel cooling technologies

In the literature and electronic cooling industry, a large variety of multi jet impingement coolers fabricated with different materials is available. Wei *et al.* [29] designed, fabricated, and experimentally characterized a high efficiency polymer based direct multi jet cooling system consisting of a 4x4 nozzle array. The multi jet cooler achieved a heat transfer coefficient of $6.25 \cdot 10^4 \text{ W}/(\text{m}^2\text{K})$ with a pumping power of 0.3W. Brunswiler *et al.* [30] demonstrated that silicon processing could be used to fabricate complex microjet array impingement coolers with branched hierarchical parallel fluid delivery and return architectures with 50,000 inlet/outlet nozzles. Such a configuration can exhibit a heat transfer coefficient of $8.7 \cdot 10^4 \text{ W}/(\text{m}^2\text{K})$ with 1.43 W of pump power. A hierarchical tree-like branching manifold was considered in their study as shown in Figure 5. However, such a system with multiple microscale nozzle diameters can lead to significant pressure drop across the system.

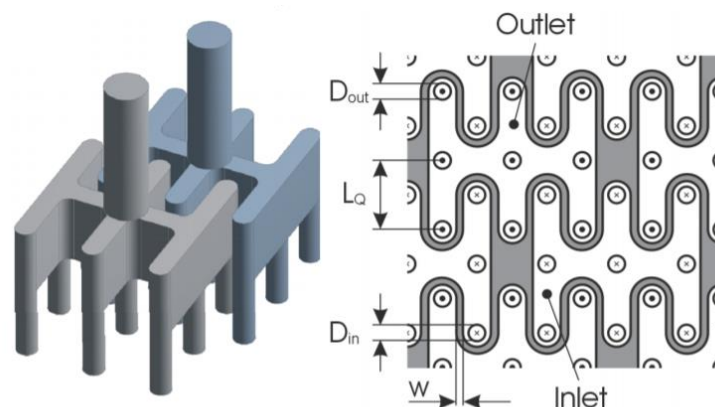


Figure 5 Liquid jet hierarchical manifold (Reprinted from [30])

A comparison of the cooling performance among cold plates, microchannel cooling, and jet impingement cooling using experimental results was conducted by Gould *et al.* [31]. The experimental study showed that for a constant device junction temperature of 175 °C, the power dissipation capability of the cold plate can be increased to 99 W and 167 W (from 60 W) for a microchannel cooler and a jet impingement cooler, respectively. Acikalin and Schroeder [32] from Intel Labs developed a stainless-steel direct liquid contact microchannel cold plate for bare die packages. The junction-to-fluid thermal resistance of 0.21 K/W for a water flow rate of 1 LPM through cold plate was achieved.

Whelan *et al.* [33] developed a miniature 3-D printed jet array water block using 49 individual 1-mm jets with the aim of achieving a cooling capacity of 200 W for a surface area of 8.24 cm². An overall thermal resistance of 0.18 K/W was achieved requiring 1.5W of hydraulic power.

Due to the advancements in additive manufacturing techniques, flow channels with composite material structures that are not possible with traditional machining processes can be made with ease. In this context, Robinson *et al.* [34] developed a micro-heat sink designed with microchannels and an array of fins with integrated microjets using a metallic additive manufacturing process resulting in a heat transfer coefficient of $30 \cdot 10^4$ W/m²·K. Simulation driven design using Ansys Fluent CFD software was undertaken to design a micro heat exchanger. The device exhibited an estimated overall thermal conductance of 300 kW/(m²K) with an associated pressure drop of 160 kPa for a flow rate of 0.5 LPM. This is equivalent to a measured base temperature of 54 °C for an applied heat flux of 1000 W/cm² assuming 20 °C water at the inlet.

Silicon based fabrication techniques have been used to make microjet and microchannel used in electronic cooling. Such fabrication techniques involve etching to make nozzles with small diameters. Han *et al.* [35] developed a hybrid system jet-based/microchannel silicon micro cooler with multiple drainage micro trenches. In the hybrid system developed by Han *et al.* [35], 0.05 W pumping power led to a heat dissipation of 260 W/cm².

Colgan *et al.* [36] tested silicon-based microchannel coolers. Using multiple heat exchanger zones and optimized cooler fin designs, a unit thermal resistance 10.5 K · mm²/W from the cooler surface to the inlet water was demonstrated with a fluid pressure drop of 35 kPa.

Han *et al.* [37] from IME proposed a package-level hotspot cooling solution for GaN transistors using a Silicon microjet/microchannel hybrid heat sink, which can enable a high spatially average heat transfer coefficient of $18.9 \cdot 10^4$ W/(m²K) with a low pumping power of 0.17 W for a flow rate of 400 ml/min. The hybrid heat sink combines the benefits of micro channel flow and micro jet impingement. COMSOL Multiphysics software was used to perform finite element analysis to evaluate the effects of design parameters of the nozzle array, micro channels, and heat sink.

Kim *et al.* [38] explored the cooling performance associated with single phase hybrid micro channel/micro jet impingement cooling method. A parametric study on the geometrical and operating parameters of the hybrid cooling was numerically investigated. An optimized geometry with 5 jet inlets of 0.19 mm diameter each, achieved a heat transfer coefficient of up to 11,152 W/m²·K. It was also observed that with decreasing the jet diameter, number of jets and increasing the mass flow rate, heat transfer coefficients of the micro channel's bottom wall increased.

Wu *et al.* [39] studied single jet and multi-jet impingement cooling programmable thermal test chips and high-power electronic devices with 500 μm inlet nozzles and distributed outlet nozzles. Three different configurations namely, jet impingement body cooling, hybrid body cooling and jet impingement surface cooling were studied as shown in Figure 6. A total thermal resistance of 0.041 K/W was achieved for a flow rate of 1800 ml/min for the jet impingement body cooling configuration. It was also observed that when the jet diameter increased, the jet impingement convective heat transfer decreased, but the channel cooling convective heat transfer coefficient did not change.

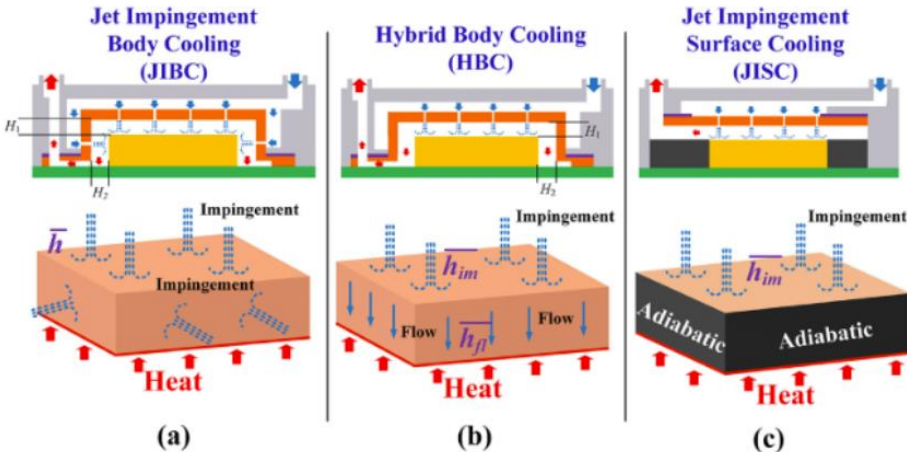


Figure 6 Schematic diagram of a) jet impingement body cooling b) hybrid body cooling c) traditional jet impingement surface cooling (Reprinted from [39])

Recently, Jorg *et al.* [40] introduced and analyzed cost-efficient cooling solution for a single MOSFET semiconductor based on a single-jet direct impingement cooler. This single chamber cooler with relatively larger nozzle diameter and simplified injection manifold can achieve heat transfer coefficients of $1.2 \cdot 10^4 \text{ W/m}^2 \cdot \text{K}$ for a pumping power of 0.9 W. However, in single-jet cooling, single hot spots can

form given the non-uniform distribution of heat transfer. Moreover, cooling efficiency of single jets quickly decays from the stagnation/impingement point toward the wall jet region.

A package level bare die liquid jet impingement was presented by Wei *et al.* [41]. This impingement cooling method was applied over a 23x23 mm² die with 285 W of power dissipation. It was compared with a standard air-cooled finned heat sink, and it was observed that the liquid cooling system performed five times more effective than air-cooled fin heat sink.

Tsunekane *et al.* [42] studied a vertical water jet impingement cooling system consisting of a circular 10 mm diameter compact heat sink. Numerical and experimental analyses were conducted with pin fin (0.14 - 0.5 mm in diameter) and flat plate configurations. A thermal resistance of 0.24 K/W was obtained in an area of 5 mm diameter of the heat sink with a flowrate of 2 LPM.

Since the literature data of the cooling and hydraulic performance are reported for different chip sizes, the data needed to be normalized to compare the intrinsic cooling performance of the different cooling systems [29]. The thermal resistance scale is inversely proportional to the chip size (resulting in low thermal resistance values for large chips). The pumping power scale is directly proportional to chip size (resulting in high pumping power values for large chips)

$$R_{\theta_v}^* = R_{\theta} \cdot A_b \quad (1a)$$

$R_{\theta_v}^*$ - Normalized thermal approach with respect to base area (K · cm²/W)

R_{θ} - thermal approach (K/W)

A_b - Base area of chip to be cooled (cm²)

$$\dot{W}^* = \frac{\dot{W}}{A_b} \quad (1b)$$

\dot{W}^* – Normalized pumping power with respect to base area $\left(\frac{\text{kW}}{\text{m}^2}\right)$

\dot{W} – pumping power (W)

Figure 7 shows the summary of the benchmarking assessment of all the state-of-the-art cooling systems discussed in the papers discussed above. As Figure 7 shows, there is a need to decrease the thermal resistance and pumping power in chip cooling and other applications.

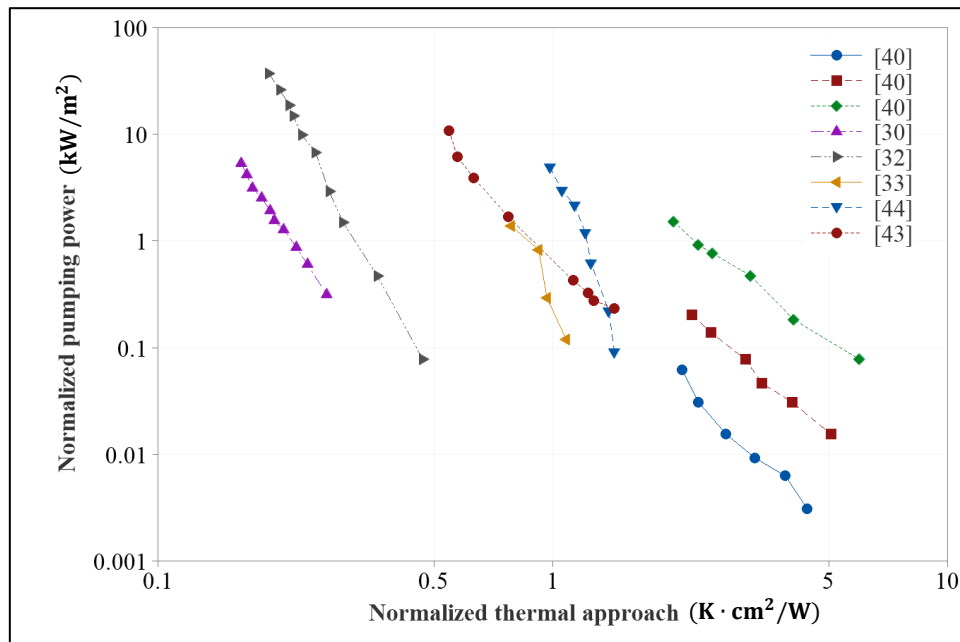


Figure 7 Benchmarking state of the art liquid cooling systems (Adapted from [29])

2.4. Knowledge gaps identified in literature

There has been a significant number of studies reported in the literature for jet impingement cooling systems, optimization studies of nozzle arrays and pin fin heat sinks. Most of the optimization studies have focused on air jets and their parametric optimization. Limited research publications are available on optimization of jet impingement cooling systems using liquid as coolant. Furthermore, all the parametric studies available in the literature have centered around individual design parameters such as jet-to-jet spacing, jet shapes, and target plate-to-jet spacing, among others. Limited research is available in the optimization and parametric study of interaction effects of orifice or manifold and heatsink parameters. The current study not only focuses on the parametric analysis of design parameters pertaining to heat sink and orifice manifolds, individually, it also considers their coupled effects.

Topology optimization has been another interesting optimization technique which can modify the shape of the jet impingement cooling system components, mainly the target heat sink with respect to a prescribed objective function. Limited research is available in topology optimization pertaining to jet impingement cooling. Most of the literature has been focused on shape modification in micro channels or natural convective heat sinks. The current study focuses on topology optimization of heat sink and the enhancement in heat transfer characteristics observed due to optimization.

In addition to the above research objectives, several heat sink designs were numerically and experimentally studied with specific emphasis on rectangular or circular pin fin configurations. Due to the advent of additive manufacturing techniques, 3D printing of copper and aluminum heat sinks has proven to be a useful technique in

the manufacturing of complex shapes to improve the heat transfer characteristics of jet impingement cooling systems altogether. The current study focuses on the numerical analysis of various heat sink designs, comparison with respect to the traditional flat plate and pin fin heat sinks and their experimental validation. The aim of this study is to identify the benefits and drawbacks of different heat sink designs considering the requirements set by jet impingement cooling. The experimental validation for this work was conducted by Nikhil Pundir [45] as part of his MS thesis and the data in it were used to validate the numerical simulation results of pressure drop shown in this study.

3. DESIGN METHODOLOGY FOR MULTI-JET COOLING SYSTEM

In this chapter description of the multi jet impingement system and various heatsinks considered for numerical analysis and optimization is presented. Additionally, the problem formulation for the optimization aspect of the study is introduced and discussed.

3.1. System configuration of multi jet cooling system

A liquid based multi jet cooling system was selected for the study given its potential in electronic cooling systems with heat loads over 70 W. The key elements of the liquid based multi jet cooling system are: Upper manifold, heat sink and lower manifold as shown in Figure 8.

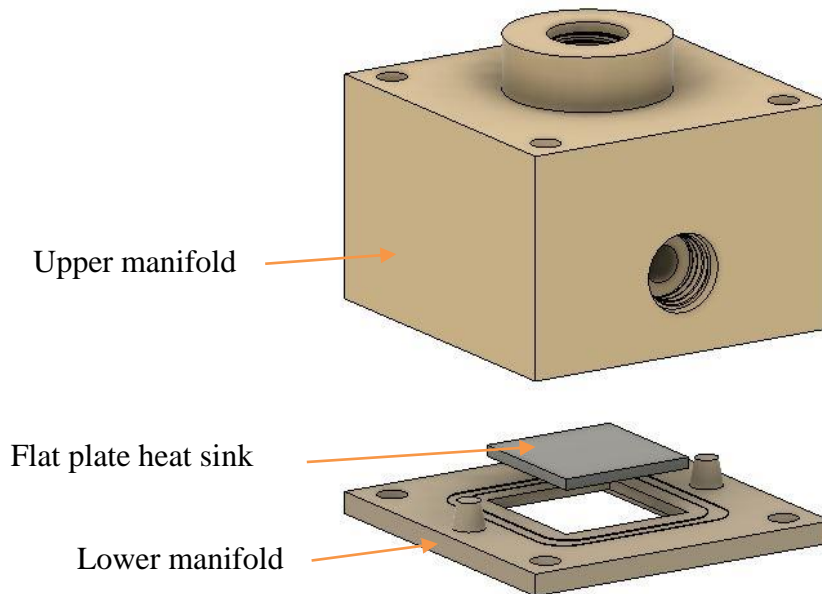


Figure 8 Exploded view of the multi jet cooler assembly

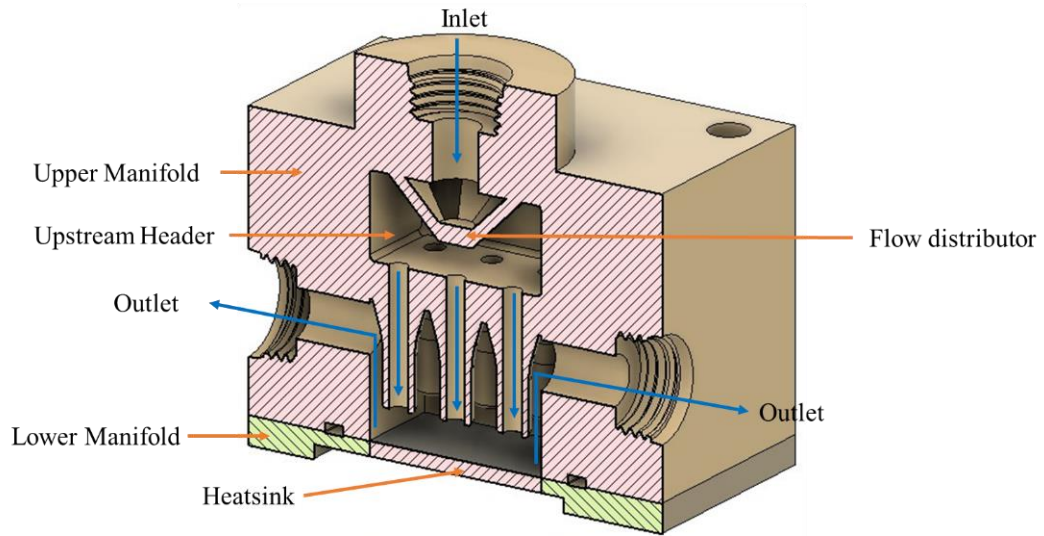
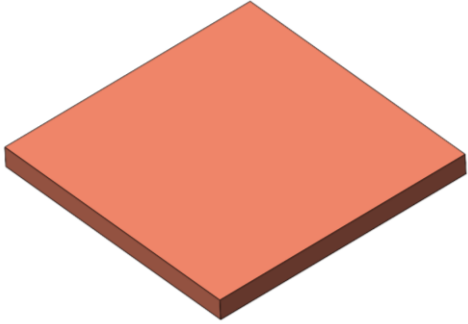
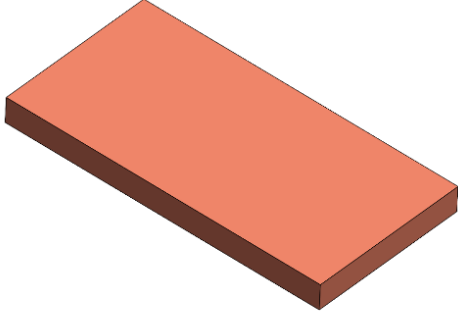
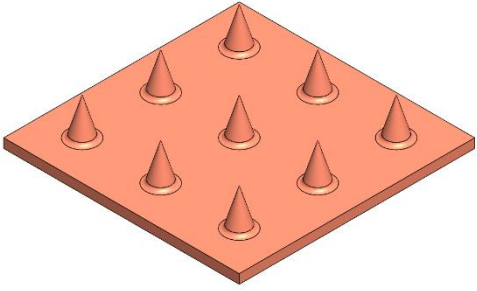
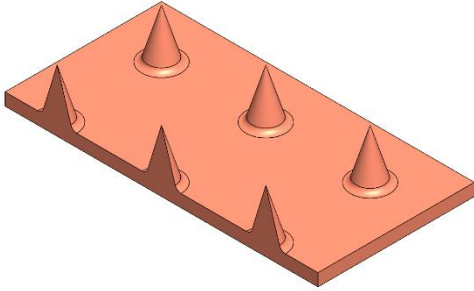
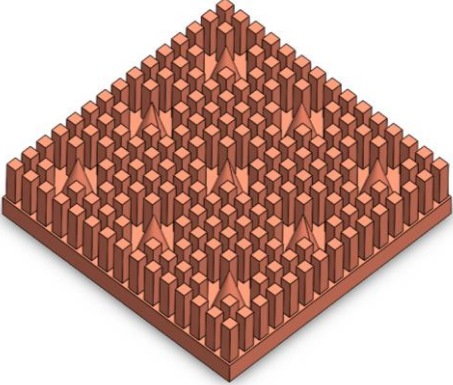
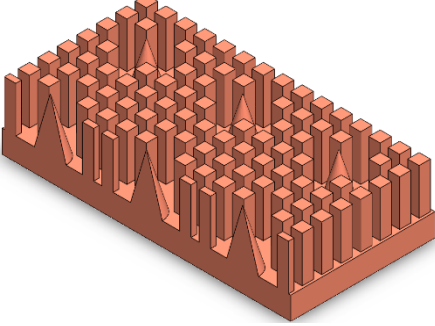


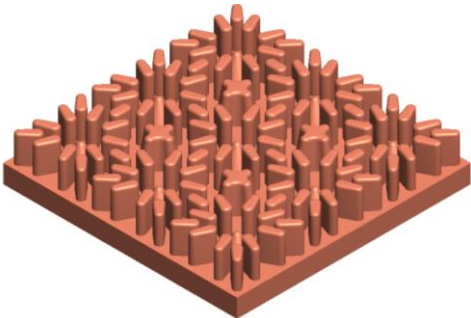
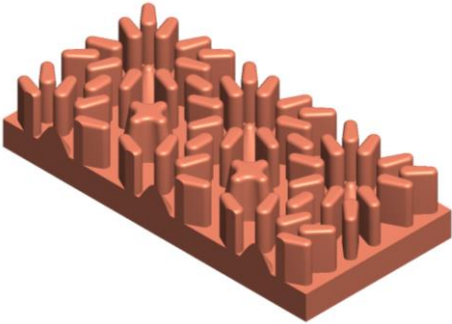
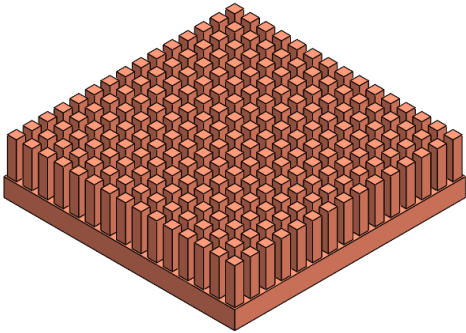
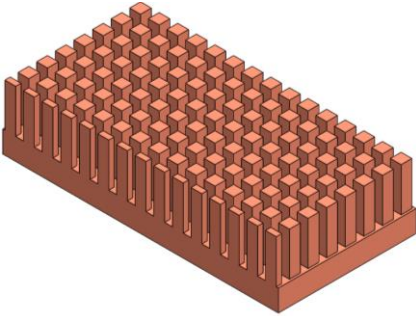
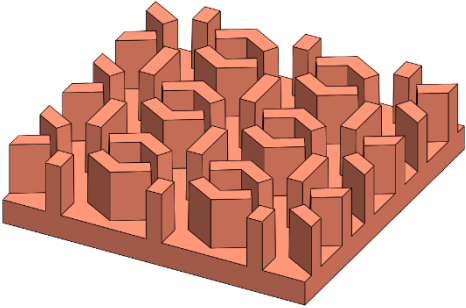
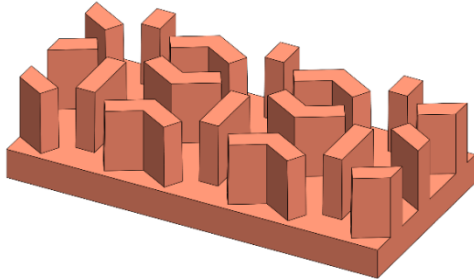
Figure 9 Components of multi jet cooler and fluid flow path

The upper manifold consists of a 3x3 array of jets with local extraction ports. The fluid enters through the inlet into the upstream header and gets distributed into 9 parallel cylindrical channels, which leads to the formation of liquid jets. The liquid flow path is shown in Figure 9. The upstream header acts as a distribution chamber and helps in distributing the flow into nine orifices and cylindrical channels. After impingement on the heat sink, the test fluid moves up through the extraction ports into the middle chamber before exiting the system.

All the heat sinks used in the study were made of copper to interact directly with the 3x3 array of liquid jets. Both the upper and lower manifolds along with various heat sink designs were considered in the numerical study, and the parametric and topology optimization steps. The dimensions of the copper heat plate were 25.4 mm x 25.4 mm with a thickness of 2 mm. Designs of the heat sinks considered for the numerical analysis are shown in Table 1.

Table 1 Heat sink designs for comparative analysis

Isometric view	Section view
<p data-bbox="326 394 509 428">a) Flat plate</p>  An isometric view of a flat, rectangular plate heat sink, colored in a reddish-brown hue. It is shown from a perspective that highlights its thin profile.	 A section view of the flat plate heat sink, showing its uniform thickness and rectangular shape from a side-on perspective.
<p data-bbox="326 861 581 894">b) Conical pin fin</p>  An isometric view of a heat sink with a flat base and several conical pin fins protruding from its surface. The fins are arranged in a grid pattern.	 A section view of the conical pin fin heat sink, showing the profile of the conical fins and their attachment to the base plate.
<p data-bbox="326 1270 760 1304">c) Conical and Square pin fins</p>  An isometric view of a heat sink with a flat base and a dense array of pin fins. The array consists of a mix of conical and square-shaped pin fins.	 A section view of the heat sink with conical and square pin fins, showing the varying heights and shapes of the fins.

Isometric view	Section view
<p data-bbox="326 394 699 428">d) Radially aligned pin fin</p>  <p>An isometric view of a square base plate with a grid of cylindrical pin fins. The fins are oriented radially, meaning their circular faces are parallel to the radial direction of the base plate.</p>	 <p>A section view of the radially aligned pin fin array. The fins appear as a series of vertical cylindrical columns. A vertical dashed line on the right side indicates the cutting plane.</p>
<p data-bbox="326 865 574 898">e) Square pin fin</p>  <p>An isometric view of a square base plate with a grid of square pin fins. The fins are oriented such that their square faces are parallel to the base plate.</p>	 <p>A section view of the square pin fin array. The fins appear as a series of vertical rectangular columns.</p>
<p data-bbox="326 1341 646 1375">f) Rectangular pin fin</p>  <p>An isometric view of a square base plate with a grid of rectangular pin fins. The fins are oriented such that their rectangular faces are parallel to the base plate.</p>	 <p>A section view of the rectangular pin fin array. The fins appear as a series of vertical rectangular columns.</p>

As shown in Figure 9, the upper manifold also includes a flow distributor to make sure each cylindrical jet hole receives an equal amount of fluid. Without a flow distributor, the flow distribution could be non-uniform across the 9 jets due to the position of the inlet. Moreover, without the flow distributor or considering the diameter of each cylindrical hole, the center orifice could receive a greater amount of fluid followed by middle orifices and finally the corner orifices. To obtain uniform cooling at the bottom heat plate, it was important to get uniform flow rate through each orifice or cylindrical hole.

In a multi jet cooling system, fluid flow is driven by pressure gradient. Due to the stagnation region expected directly at the impingement zone within the upstream header, the pressure inside of it could also be non-uniform. This could result in the non-uniform flow distribution across the multiple jets. To make the flow rate uniform, the stagnation zone was shifted away from the center jet as shown in Figure 9.

3.2. Problem formulation and data reduction for optimization of multi jet cooling system and comparative analysis of heat sinks

As stated in section 1.2, the main objective of this study was to maximize the heat transfer of the multi jet cooling system while keeping the required pumping power to a minimum. To compare different heat sinks under identical boundary conditions several heat transfer and fluid flow parameters were defined.

As part of the multi-objective optimization methodology, thermal approach (R_{θ}) was used in the study. Thermal approach is defined as the increase in the average surface temperature of the heat plate per unit heat input as given in Equation (2). In a nutshell, it is an indication of the overall thermal resistance of the overall multi jet array system. Maximizing the convective heat transfer of the multi jet array cooling system can be attributed to minimizing the thermal approach value as well.

$$R_{\theta} = \frac{T_s - T_{bulk}}{q'' A_s} \text{ (K/W)} \quad (2)$$

$$T_{bulk} = \frac{T_{in} + T_{out}}{2} \text{ (K)} \quad (3)$$

T_s – Average surface temperature of the heat sink bottom surface (K)

T_{in} – Fluid inlet temperature (K)

T_{out} – Fluid outlet temperature (K)

As part of the multi-objective optimization methodology, pumping power (\dot{W}) as given by Equation (4) was also chosen as an objective function, since it represents the power penalty for achieving a certain Re_θ value.

$$\dot{W} = dP \cdot \dot{V} \text{ (W)} \quad (4)$$

dP – Pressure drop across the multi-jet cooler system (Pa)

\dot{V} – Volume flow rate (m^3/s)

Additional heat transfer and fluid flow characteristic quantities such as Reynolds (Re), heat transfer coefficient based on liquid-side surface area (h_{LSA}), Nusselt number (Nu) for a 9-jet array, normalized thermal approach ($R^*_{\theta V}$), and normalized pressure drop also known as friction factor (c_f) are defined as shown below to further understand the physical behavior of the jet impingement cooling system in detail.

$$Re = \frac{\rho v_j d_j}{\mu} \quad (5)$$

ρ – fluid density (kg/m^3)

v_j – jet velocity (m/s)

d_j – jet diameter (m)

μ – dynamic viscosity of the fluid

$$h_{LSA} = \frac{\dot{Q}}{A_{LS} \cdot (T_s - T_{bulk})} \text{ (W/m}^2 \cdot \text{K)} \quad (6)$$

A_{LS} – liquid-side surface area of the fluid and solid interface (m^2)

\dot{Q} – heat input from the surface heater (W)

T_s – average surface temperature of the heat sink bottom surface (K)

T_{bulk} – bulk fluid temperature defined by the Equation 3

$$Nu = \frac{h_{LSA} \cdot d_j}{k_f} \quad (7)$$

k_f – thermal conductivity of fluid ($\text{W/m} \cdot \text{K}$)

$$R^*_{\theta V} = R_{\theta} \cdot V \quad (8)$$

R_{θ} – thermal approach defined as per Equation 2

V – solid volume of heat sink

$$C_f = \frac{dP}{\frac{1}{2} \cdot \rho \cdot v_j^2} \quad (9)$$

dP – pressure drop across the multi-jet cooling system (Pa)

$$EF = \left(\frac{R_{\theta_{\text{finned heat sink}}}}{R_{\theta_{\text{flat plate}}}} \right)^{-1} \quad (10)$$

EF – Thermal approach enhancement factor

$R_{\theta_{\text{finned heat sink}}}$ – Thermal approach of finned heat sink

$R_{\theta_{\text{flat plate}}}$ – Thermal approach of flat plate heat sink

As part of the design of the multi jet cooling system, there are multiple design variables that contribute indirectly to each objective function, as discussed in greater detail in Chapter 4. Minimizing the thermal approach of the system requires greater level of internal convection, which entails greater fluid flow through the system. At greater fluid flow, the system would exhibit greater pressure drop resulting in greater pumping power or greater energy cost over time. Therefore, a tradeoff between the two objective functions (R_{θ} and \dot{W}) should be explicitly identified, so the system designer can make the proper tradeoff analysis among the optimal designs of the multi-jet array impingement cooling system. Different types of optimization techniques such as Sequential Quadratic Programming, Heuristic optimization (Genetic algorithm) were explored and are discussed in further detail in the subsequent chapters (Chapters 4 and 5).

Once the objective functions were postulated, the next step was to determine the geometric parameters of the design contributing to the variance of these objective functions. To employ the corresponding optimization technique, one of the heat sink designs consisting of cones was considered. By considering this design, it was feasible to

explore the corresponding optimization technique since it has a limited number of parameters and a good space for optimization. In the case of the other designs, due to the high amount of surface area available for convective heat transfer, the optimal design was simply the heat sink with most surface area available for convective heat transfer.

Design parameters were divided into 2 subsets – manifold parameters and heat plate parameters (as shown in Figure 10). Diameter of the jet, Height of impingement (distance from the starting of jet to the heat plate), Outlet height, Tube height (length of the jet before impinging the heat transfer surface) were the manifold parameters. Angle of the cone and height of the cone were the heat plate parameters. Hence the mathematical formulation of the optimization can be represented as follows:

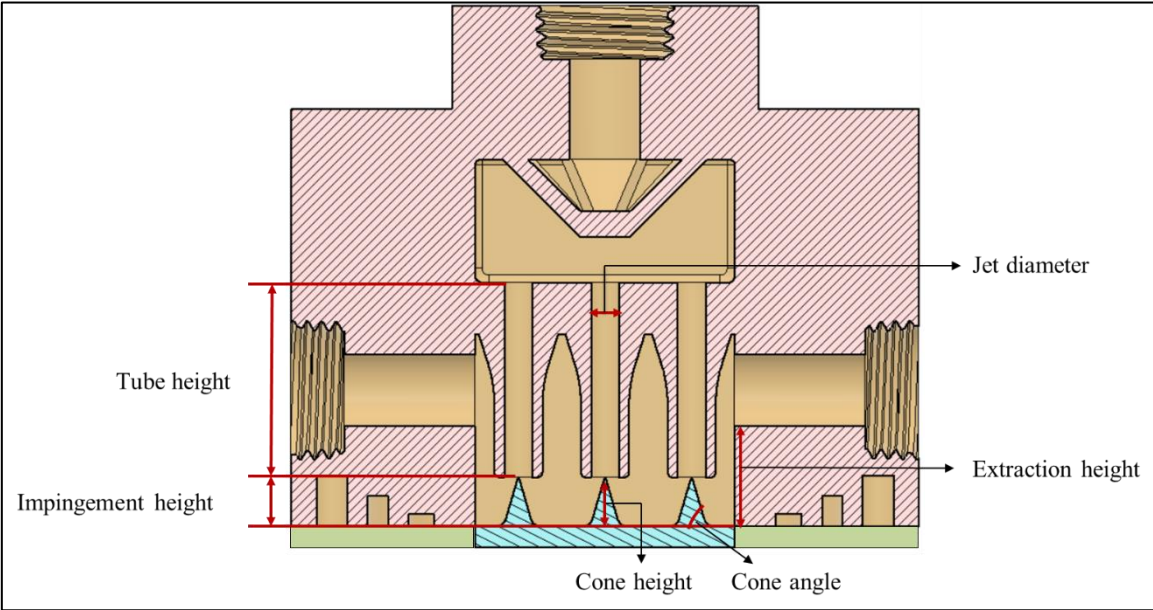


Figure 10 Design parameters of the multi-jet array cooling system

Objective functions:

$$\begin{bmatrix} J_1 \\ J_2 \end{bmatrix} = \begin{bmatrix} \text{Thermal Approach} \\ \text{Pumping Power} \end{bmatrix} \quad \begin{array}{l} \text{Min } J_1 (x_1, x_2, x_3, x_4, x_5, x_6) \\ \text{Min } J_2 ((x_1, x_2, x_3, x_4, x_5, x_6)) \end{array}$$

The design vector affecting J_1 and J_2 is given below (shown in Figure 10)

$$\begin{bmatrix} x_1 \\ x_2 \\ x_3 \\ x_4 \\ x_5 \\ x_6 \end{bmatrix} = \begin{bmatrix} \text{Jet Diameter} \\ \text{Tube height} \\ \text{Impingement Height} \\ \text{Extraction Height} \\ \text{Cone Height} \\ \text{Cone Angle} \end{bmatrix}$$

As the cones on the heat plate should not protrude into the jets, it was important that the cone height should not be greater than impingement height. Also, to avoid cones from merging or overlapping, a limit of cone height and cone angle was required and set accordingly. Constraints of the design parameters are shown in Table 3. To make the design study scalable, the area of the heat plate was fixed to 25.4 mm x 25.4 mm. By fixing the area, we could obtain the lower and upper bounds of the jet and cone parameters. Other bounds were fixed based on initial design explorations. Upper and lower bounds of the design parameters are shown in Table 2.

Table 2 List of design parameters and bounds

Parameter	Name	LB	UB
x ₁	Jet diameter	2 mm	5 mm
x ₂	Tube height	8 mm	15 mm
x ₃	Impingement height	3 mm	10 mm
x ₄	Extraction height	4 mm	10 mm
x ₅	Cone height	3 mm	7 mm
x ₆	Cone angle	50°	75°

Table 3 Design constraints

Constraint	Expression	Note
Height constraint	$x_5 \leq x_3$	Cone height should be lower than impingement height
Angle constraint	$1 \leq \frac{x_5}{\tan(x_6)} \leq 4.2$	Cone diameter should be less than 8.4 mm to avoid merging of cones

3.3. Model implementation algorithm

To optimize the objective for a given set of parameters and constraints, there was a need to develop empirical relations for the objective functions (J_1, J_2) in terms of design parameters ($x_1, x_2, x_3, x_4, x_5, x_6$). Since the governing equations for the jet impingement are not linear or algebraic in nature, the analytical model of the design could not be formulated in a straightforward fashion. So, a CFD simulation scheme for the multi jet cooler was set up. The value of the objective functions for different design vectors values were obtained from the computational fluid dynamics simulations.

The need to automate the optimization process was recognized in the early stages of the study. Figure 11 shows the algorithm used for the automation of the optimization process. Macros were written in Visual Basic to seamlessly transfer data between different modules

Design vectors were stored in an Excel file and imported into a commercial 3D modelling software, SOLIDWORKS to create multiple configurations of 3D models of multi jet cooler. All the design models were then exported using a macro script. Star-CCM+ was used to perform all the CFD simulations (the setup of the CFD simulations is discussed in detail in Chapter 4). The 3D models, which were obtained from SOLIDWORKS were imported into the design manager module of Star-CCM+. A macro script was written to automate the steps such as pre-processing, problem setup and post processing in the CFD simulations. Temperatures of the heat plate, fluid inlet and outlet temperatures, flow rate and pressure drop of the system were the output values obtained after the CFD simulations.

MATLAB was then used to perform a regression to obtain the objective functions. The optimization toolbox in MATLAB was used to optimize the design using the Sequential Quadratic Programming and genetic algorithms based on multi objective optimization (discussed in further detail in Chapter 4)

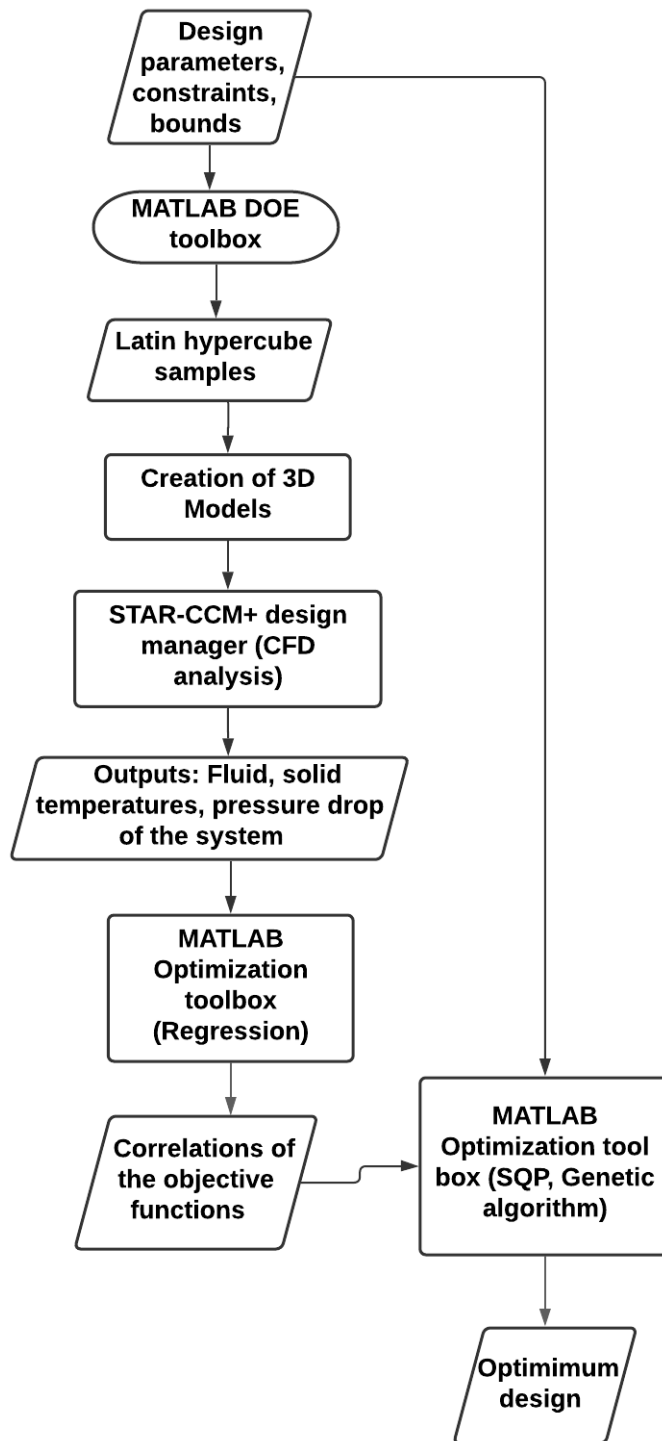


Figure 11 Optimization algorithm

4. NUMERICAL APPROACH: COMPUTATIONAL FLUID DYNAMICS, DESIGN OPTIMIZATION, TOPOLOGY OPTIMIZATION AND GRID INDEPENDENCE STUDY

4.1. Computational Fluid Dynamics in Multi-jet Cooling Systems

4.1.1. CFD and its advantages in the study of multi-jet cooling systems

Using physical experiments and tests to get essential engineering data for design can be expensive. When developing a design for an application, say liquid cooling system in the context of this thesis, we need to analyze and visualize the physical phenomenon, flow fields, temperature, and pressure distributions for various configurations. Using sensors and gauges in physical experiments, data can only be extracted at a limited number of locations in the system.

Richard Feynman once said *“It doesn't matter how beautiful your theory is, it doesn't matter how smart you are. If it does not agree with experiment, it is wrong. In that simple statement is the key to science”*. Keeping that in mind, even though there is no alternative for real life experiments, conducting numerous experiments without prior knowledge of the physics involved can be futile. In case of numerical techniques, partial differential equations representing the physics of the system are approximated using algebraic equations. CFD is a numerical technique which uses finite volume or finite element methods to approximate the partial differential equations such as Continuity, Navier-Stokes, and energy equations. CFD can be used to simulate a physical condition and isolate specific phenomena for the study.

Given the complexities and challenges associated with the simulation of multiple jet impingement cases involving various design configurations, a numerical simulation methodology was implemented. All numerical simulations including design of experiments based on space variable exploration, mesh generation and post processing have been performed using commercial CFD software Star-CCM+. Figure 12 shows a standard methodology for CFD analysis

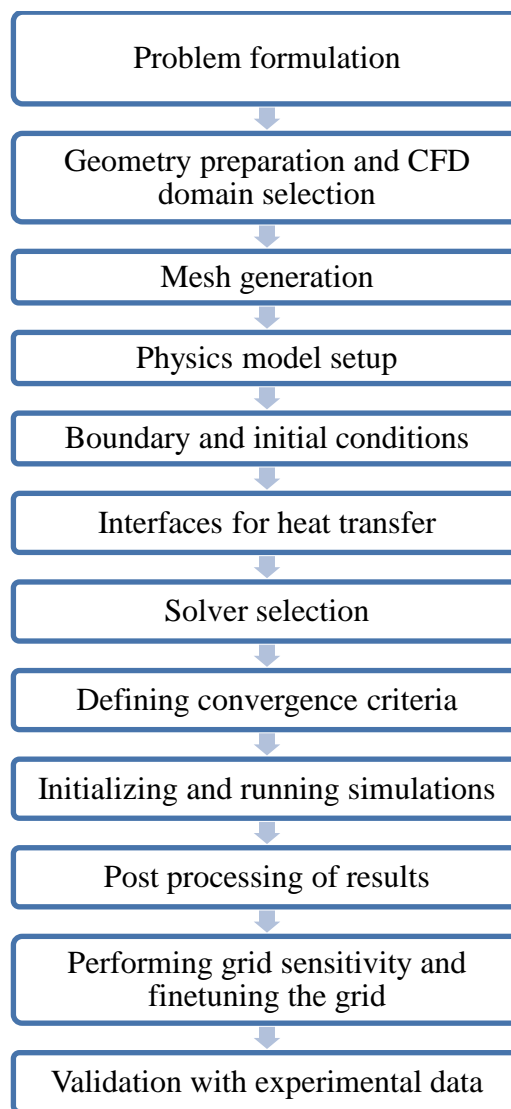


Figure 12 Standard methodology for CFD analysis

As discussed in Chapter 3, a novel geometry with 3x3 array of jets was considered for computational analysis. The objective of the study was to conduct numerical simulations to better understand and compare different parameters of the multi jet array system. The sections below include, flow and heat transfer parameters, mesh information, governing equations, boundary and initial conditions, solver selection and convergence criteria and post processing used in numerical models.

4.1.2. *Governing Equations in CFD analysis:*

Next step in the CFD process was to select and apply the correct governing equations. These governing equations are used to obtain the appropriate thermo-fluid flow properties. Discretization methods were used to convert the continuous system of equations to a set of discrete algebraic equations, which were used by numerical solvers in the CFD software. In the discretization process, the continuous domain was divided into a finite number of subdomains (cells). The unknown variables were stored at specific locations of the mesh (cell centroids in case of finite volume method). An integral or weak form of differential equations was used for spatial discretization.

The fundamental laws that govern the mechanics of fluids and solids are the conservation of mass, linear and angular momentum, and conservation of energy. The corresponding equations are shown below:

Conservation of mass:

$$\nabla \cdot \mathbf{v} = 0 \quad (11)$$

where \mathbf{v} is the continuum velocity.

Conservation of linear momentum:

$$\rho \nabla \cdot (\mathbf{v} \otimes \mathbf{v}) = \nabla \cdot \boldsymbol{\sigma} + \mathbf{f}_b \quad (12)$$

Where \otimes denotes the cross product, \mathbf{f}_b denotes the resultant of body forces (such as gravity) per unit volume acting on the continuum, and $\boldsymbol{\sigma}$ is the stress tensor. For a fluid, the stress tensor is written as the sum of normal and shear stresses given by Equation (13)

$$\boldsymbol{\sigma} = -p\mathbf{I} + \mathbf{S} \quad (13)$$

where p is the pressure, \mathbf{I} is the identity tensor and \mathbf{S} is the viscous stress tensor. Hence the linear momentum equation simplifies to

$$\rho \nabla \cdot (\mathbf{v} \otimes \mathbf{v}) = -\nabla \cdot (p\mathbf{I}) + \nabla \cdot \mathbf{S} + \mathbf{f}_b \quad (14)$$

Conservation of angular momentum:

Conservation of angular momentum requires the stress tensor to be symmetric

$$\boldsymbol{\sigma} = \boldsymbol{\sigma}^T \quad (15)$$

Conservation of energy:

Conservation of energy is derived from the first law thermodynamics applied over a control volume

$$\rho \nabla \cdot (\mathbf{E} \mathbf{v}) = \mathbf{f}_b \cdot \mathbf{v} + \nabla \cdot (\mathbf{v} \cdot \boldsymbol{\sigma}) - \nabla \cdot \mathbf{q} \quad (16)$$

Where E is the total energy per unit mass and \mathbf{q} is the heat flux

In addition to the above fundamental equations, other equations used in turbulence schemes were considered to predict the turbulence behavior of the fluid. Most fluids were characterized by irregularly fluctuating flow quantities. Often these fluctuations were at very small scales and high frequencies that resolving them in time and space usually comes at excessive computational costs. Instead of solving for exact governing equations of

turbulent flows (Direct Numerical Simulation or DNS), it is less expensive to solve for averaged quantities and approximate the impact of small fluctuating quantities.

Reynolds averaged Navier stokes (RANS) turbulence models provide closure relations that govern the transport of mean flow quantities. Each solution in the instantaneous Navier Stokes equations is decomposed into its mean and fluctuating components as shown in Equation 17.

$$\Phi = \bar{\Phi} + \Phi' \quad (17)$$

Where Φ represents velocity components, pressure, or energy. Ensemble averaging is done on the instantaneous Navier stokes equation resulting the equations below:

$$\nabla \cdot \bar{\mathbf{v}} = 0 \quad (18)$$

$$\rho \nabla \cdot (\bar{\mathbf{v}} \otimes \bar{\mathbf{v}}) = -\nabla \cdot \bar{\mathbf{p}} + \nabla \cdot (\bar{\mathbf{S}} + S_{RANS}) + \mathbf{f}_b \quad (19)$$

$$\rho \nabla \cdot (\bar{\mathbf{E}} \bar{\mathbf{v}}) = \mathbf{f}_b \cdot \bar{\mathbf{v}} + \nabla \cdot (\bar{\mathbf{S}} + S_{RANS})\bar{\mathbf{v}} - \nabla \cdot \bar{\mathbf{q}} - \nabla \cdot \bar{\mathbf{p}}\bar{\mathbf{v}} \quad (20)$$

The additional term which comes from the ensemble averaged Navier stokes and energy equations, is the turbulent stress tensor S_{RANS} . Eddy viscosity and Reynold's stress transport models are used to approximate the turbulent stress tensor. In this study, κ - ϵ eddy viscosity model was used to simulate the jet impingement cooling system at Reynolds numbers pertaining to the turbulent regime. The details of the turbulent scheme and solver selection is discussed in Chapter 4.

4.1.3. Fluid and Solid material selection

Water was used as the working fluid for CFD analysis as well as experimental validation. All the physical properties such as density, dynamic viscosity, thermal conductivity, and specific heat vary with respect to the temperature of the fluid. This temperature variation was considered by prescribing the properties of water as per IAPWS-IF97 (International Association for the Properties of Water and Steam, Industrial Formulation 1997). The IAPWS-IF97 model for water was in-built as part of the Star-CCM+ material database [46]. Table 4 shows the water properties at 300K.

Table 4 Physical properties of water at 300K

Physical property	Value
Thermal conductivity	0.62 W/(mK)
Specific heat	4819 J/(KgK)
Density	998 kg/m ³
Dynamic viscosity	0.00089 Pa-s

The upper and lower manifolds were 3D printed using ABS (Acrylonitrile Butadiene Styrene) with the molecular formula $(C_8H_8 \cdot C_4H_6 \cdot C_3H_3N)_n$. Physical properties of ABS at 300K are shown in Table 5 [46]. Since the heat transfer through plastic was insignificant, its temperature was not expected to vary by a large amount. Hence the physical properties were assumed to be constant with respect to temperature.

Table 5 Physical properties of ABS at 300K used in upper and lower manifold

Physical property	Value
Thermal conductivity	0.625 W/(mK)
Specific heat	1000 J/(KgK)
Density	1050 kg/m ³

In the numerical and experimental study, copper was used as the material for the heat sinks and heat spreader. Thermal conductivity, specific heat and density of copper was expected to change with respect to temperature. Hence a 2nd order polynomial function with respect to temperature was prescribed in Star-CCM+ for the physical properties of copper. Table 6 shows the physical properties at 300K [46].

Table 6 Physical properties of copper at 300K

Physical property	Value
Thermal conductivity	400 W/(mK)
Specific heat	386 J/(KgK)
Density	8920 kg/m ³

4.1.4. Solver selection for multi-jet fluid simulation

Once the governing equations were selected and material properties were assigned to respective fluid and solid components in the multi jet cooling system, CFD solution methods and solvers were selected in the commercial software Star-CCM+. Table 7 shows the different solver options used in the simulations.

Table 7 Solver options and models used in the CFD study

Parameters	Definition
Solver	3D, steady state, double precision
Viscous model	Laminar, κ - ϵ two layer all y^+ turbulence model
Flow and energy model	Segregated fluid and solid temperature model

Depending on the inlet volumetric flow rate, laminar and turbulent models were selected accordingly. The κ - ϵ turbulence model is a two-equation model that solves the transport equations for the turbulent kinetic energy κ and turbulent dissipation rate ϵ to determine the eddy viscosity. Two-layer approach is used in which the near wall computation is divided into two regions. In the layer next to the wall, ϵ and turbulent viscosity are specified as functions of wall distance. In the region far from the wall, transport equations are used to compute κ and ϵ . Wall y^+ which is the non-dimensional distance normal to the wall, was monitored during the simulation and the mesh size near the wall was selected such as to maintain a wall y^+ less than 1.

The CFD solution method chosen was an important factor to consider since it affected the accuracy of the numerical simulation. The solution method options used as part of this study are shown in Table 8. Segregated flow solver was selected for the CFD analysis for the study. It solves the integral equations of mass and momentum in a sequential manner. The segregated flow solver also employs a pressure-velocity coupling algorithm. The SIMPLE scheme was selected for pressure-velocity coupling with a 2nd order upwind scheme to model convection and diffusion flux on the cell faces in the transport equations. The velocity under-relaxation factor was set to 0.7 and was implemented in an implicit manner. Similarly, the implicit pressure under-relaxation was set to 0.3.

The segregated fluid and solid temperature model solved the total energy equation with respect to temperature as the solved variable. The under-relaxation factors for the energy equation in fluid and solid were set to 0.9 and 0.99, respectively.

Table 8 Solution method options used in the CFD study

Parameters	Definition
Pressure Velocity coupling	SIMPLE
Convection scheme	2 nd Order upwind
Velocity under relaxation for flow solver	0.7
Pressure under relaxation for flow solver	0.3
Fluid under relaxation for energy solver	0.9
Solid under relaxation for energy solver	0.99

4.1.5. Convergence criteria for numerical simulations

A relative convergence criterion was used to ensure adequate numerical results. The average surface temperature of the heat sink's bottom surface was used as a convergence criterion. Asymptotic convergence was used to determine whether the CFD simulation has stabilized for a particular range of the surface temperature during several iterations. Equation 21 shows the asymptotic convergence used in this study.

$$|\text{Max}(T(i), T(i - 1), \dots T(i - 10)) - \text{Min}((T(i), T(i - 1), \dots T(i - 10)))| \leq 10^{-4}$$

- (21)

T – average surface temperature of the heatsink' s bottom surface

i – iteration

The number of samples over which the asymptotic limit criteria was calculated was set to 10.

The range of the asymptotic values (Max -Min) was set to 10^{-4} .

4.2. Optimization study for multi-jet fluid system

4.2.1. Latin hypercube specification for design space of multi-jet fluid system

As part of the optimization process, multiple steps were undertaken to achieve the desired results. The first step was to create a design space with input design vectors and outputs such as thermal approach and pumping power for this study. The Latin hypercube sampling (LHS) approach was used for creating the design space. The LHS combined the input parameters with each other to maximize the minimum distance between generated points. This promoted an even distribution of the design points over the design space. Figure 13 shows an example of the LHS in case of two design parameters.

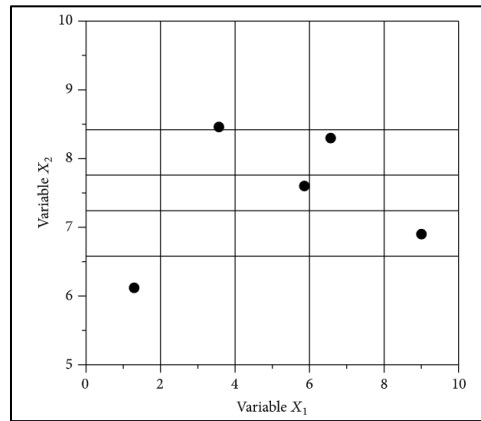


Figure 13 Latin hyper cube sampling design space for two design parameters (Reprinted from [47])

MATLAB DOE toolbox was used to create the LHS samples for this study. 100 Latin hypercube samples were created based on the lower, and upper bounds of each design variable as shown in Table 2, and the design constraints are shown in Table 3. The 3D models corresponding to the design vectors obtained through this process were

generated using SOLIDWORKS and used by the CFD software to simulate fluid and heat transfer behavior in each case under identical boundary conditions.

4.2.2. *Gaussian regression for input to output variables in multi-jet cooling system*

Once the Latin hypercube samples were created, the CFD simulations of all the 100 samples were conducted. Thermal approach (R_{θ}) and pumping power (\dot{W}) were the outputs of the CFD simulations. The next step in the optimization process was to formulate analytical equations for the objective functions (R_{θ} and \dot{W}) used in the study. Gaussian process regression (GPR) was used, which consists of non-parametric kernel-based probabilistic models. GPR has several benefits including the ability to work on small datasets and provide accurate predictions. The MATLAB Regression Learner toolbox was used to create the GPR models for the objective functions. The model properties are shown in Table 9.

Table 9 Gaussian Process Regression model properties

Parameters	Definition
Kernel function	Rational quadratic
Basis function	Linear
Cross validation	5 folds
R-square	0.99

Kernel, basis function and cross validation parameter options were selected in such a way as to obtain a maximum R-square or minimum root mean square errors for both objective functions.

4.2.3. Gradient based optimization techniques (Sequential Quadratic Programming)

As part of the optimization process, the Sequential Quadratic Programming (SQP) gradient-based optimizer was chosen since it performs well when using non-linear objective functions, as the ones obtained in this study. The gradient-based optimization technique used in the study was the steepest descent method, which uses the gradient vector at each point as the search direction in each iteration. The gradient vector is orthogonal to the plane tangent of the iso-surfaces of the function. It also indicates the direction of the maximum rate of change of the function at that point. For a function $f(x_1, x_2 \dots \dots x_n)$ the gradient is given by Equation 22.

$$\nabla f(x_1, x_2 \dots \dots x_n) = \frac{\partial f}{\partial x_1} \widehat{x}_1 + \frac{\partial f}{\partial x_2} \widehat{x}_2 + \dots + \frac{\partial f}{\partial x_n} \widehat{x}_n \quad (22)$$

Hessian matrix is a square matrix of second order partial derivatives of a scalar valued function as shown in Equation 23. It is used to calculate the local curvature of a multivariable function. The Hessian matrix of the function f is the Jacobian matrix of the gradient of the function as shown in Equation 24.

$$H(f) = \begin{bmatrix} \frac{\partial^2 f}{\partial^2 x_1^2} & \cdots & \frac{\partial^2 f}{\partial x_1 \partial x_n} \\ \vdots & \ddots & \vdots \\ \frac{\partial^2 f}{\partial x_n \partial x_1} & \cdots & \frac{\partial^2 f}{\partial^2 x_n^2} \end{bmatrix} \quad (23)$$

$$H(f(x)) = J(\nabla f(x)) \quad (24)$$

MATLAB optimization toolbox was used in the SQP approach. However, this method can only optimize single objective functions. Hence, a weighted average of R_θ (J_1) and \dot{W} (J_2) was considered for the single objective optimization. The mathematical formulation is shown as follows:

$$J^* = \lambda_1 \cdot J_1 + \lambda_2 \cdot J_2 \quad (25)$$

J^* – Weighted objective function

λ_1, λ_2 – Weights of J_1 & J_2 respectively

The constraints used in the SQP optimization are given in Table 3.

A weightage of 75% to thermal approach and 25% to pumping power was considered for this step given the relative importance of each factor in the electronic industry.

$$[\lambda_1, \lambda_2] = [0.75, 0.25] \quad (26)$$

Since the objective functions and feasible regions were not convex, there was no guarantee of finding the global optimum with gradient-based algorithms. With the SQP technique, the local optimum was guaranteed. For this reason, the SQP optimization was carried out using multiple start vectors obtained through random sample generation method using MATLAB programming. Results obtained using a multi-start approach are discussed in Chapter 5.

To make the optimization computationally more efficient, scaling of objective functions and the design parameters were done as well. This approach not only helps in terms of computational efficiency, but it also helps in reducing the computational time. In the case of objective functions (R_θ and W), scaling was done by finding the individual maximum values using the MATLAB optimization toolbox. Equation 27 represents the scaled mathematical formulation of the objective functions.

$$[J_1, J_2] = \left[\frac{J_1}{SF_1}, \frac{J_2}{SF_2} \right] \quad (27)$$

$$SF_1 = \text{Max}(J_1)$$

$$SF_2 = \text{Max}(J_2)$$

To scale the design variables, hessian matrix was used. The diagonal elements of the hessian matrix are shown in Equation 28.

$$H_{ii} = \frac{\partial^2 J^*}{\partial x_i^2} \quad (28)$$

The hessian matrix was calculated using a 2nd order central difference scheme as shown in Equation 29.

$$H_{ii} = \frac{\partial^2 J^*}{\partial x_i^2} = \frac{J^*(x_1, \dots, x_i + \Delta x_i, \dots, x_n) - 2J^*(x_1, \dots, x_i, \dots, x_n) + J^*(x_1, \dots, x_i - \Delta x_i, \dots, x_n)}{\Delta x_i^2} \quad (29)$$

Calculation of the hessian matrix was done using 2nd order central difference scheme since the objective functions and the Jacobian of the objective function were nonlinear equations and calculation of gradient analytically was not feasible. All the design variables were multiplied by a factor of $H_{ii}^{-0.5}$. The scaled design variable is shown in equation 30.

$$x_i^* = x_i * H_{ii}^{-0.5} \quad (30)$$

By using the method described above, an optimum design vector for the multi-jet liquid system was obtained. The results of this approach can be found in Chapter 5

4.2.4. Heuristic optimization technique in multi-jet fluid system

Heuristic technique is a computational procedure that determines the optimal solution by iteratively improving the solution with respect to a given measure. Genetic algorithm is an adaptive heuristic algorithm based on natural selection and genetics. The basic principle is based on survival of the fittest theory by *Charles Darwin*. The typical steps involved in the optimization process based on genetic algorithms are: a) choosing an

initial population of solutions b) calculating the fitness and how well the individual solution is c) performing crossover from the population

In the scope of this study, MATLAB Optimization toolbox was used to conduct multi-objective genetic algorithm-based optimization. The parameters and values used in the optimization process are shown in Table 10.

Table 10 Parameters used in multi-objective genetic algorithm

Parameters	Value/definition
No. of parameters	4
Initial population size	200
Function tolerance	10^{-4}
Constraint tolerance	10^{-4}
Maximum generations	1500
Creation function	'gacreationuniform'

4.2.5. Domain selection for optimization of cone pin heat sink using genetic algorithm

To simulate fluid and heat transfer behavior in a multi jet impingement system, the fluid domain within the manifold was used. Since the objective of the numerical simulation was to conduct a comparative analysis, a reduced domain without the upstream header was considered. Figure 14 shows the domain of the fluid and solid used in the numerical analysis of optimization study.

The domain consisted of 4 inlets and 1 outlet. Since the design was symmetrical with respect to x, z axes, 1/4th of the complete domain was considered in the study. Upper and lower manifolds were not considered in the CFD simulations since the heat loss through the plastic was assumed to be constant and negligible for all the designs due to the low thermal conductivity of the plastic (ABS). The height of the fluid domain was determined by the two design vector parameters, impingement height and tube height. Depending on the design vectors, the dimensions of the fluid domain changed accordingly and was always equal to the summation of impingement height and the tube height. The outlet position was extended far enough from the domain such as to avoid reverse flow and to achieve fully developed flow during the CFD simulation. Length of the outlet channel was set at 40 mm and kept constant for all the design vectors.

The copper heat plate had a constant thickness of 2 mm for all design vectors and was assumed to be uniformly heated from the bottom surface (details of the boundary conditions used in the numerical analysis is discussed in section 4.2.7).

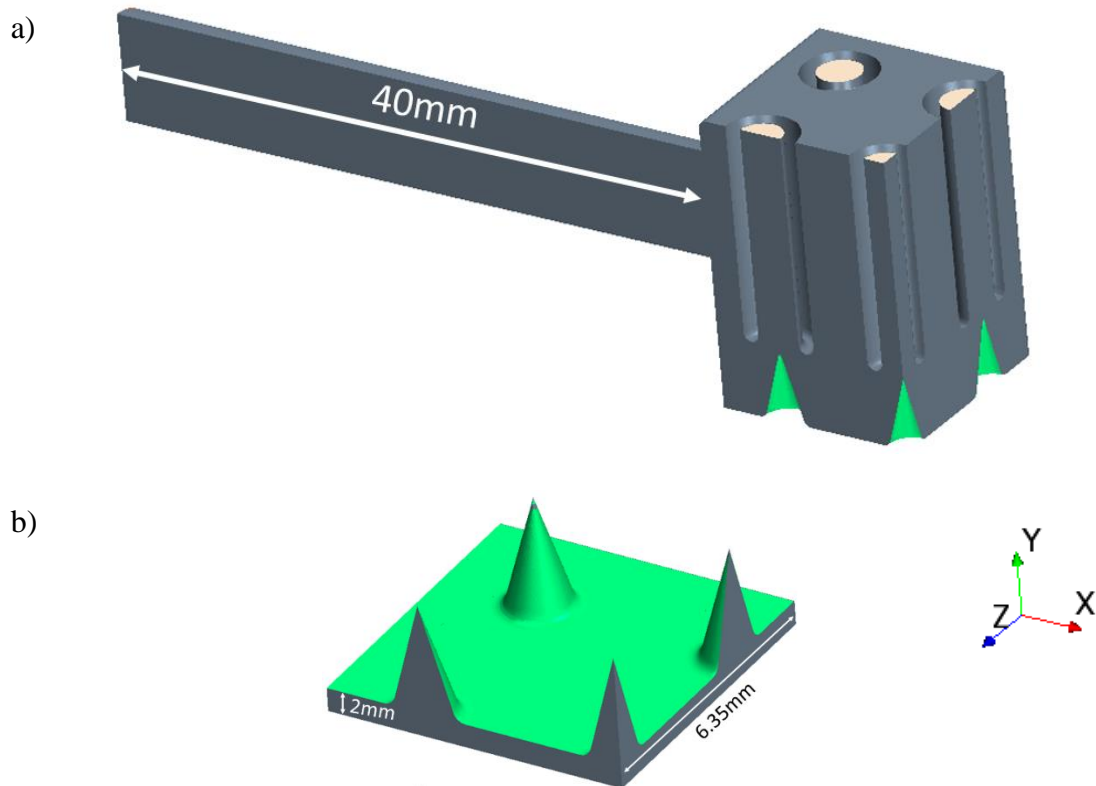


Figure 14 a) Fluid Domain b) Solid Domain

4.2.6. Mesh generation for multi-jet liquid system optimization study

A mesh is a discretized representation of a geometric domain. This domain generally includes real-world geometry, its content, and its surrounding environment. The CFD solver finds solutions to governing equations at the locations defined by the mesh. For finite volumes, CFD solver computes values at the center of each cell, where values are computed at cell nodes (typically used in solid mechanics). The typical mesh generation algorithm of a 3D domain consists of two different meshing schemes – surface mesh to remesh the initial surface of a geometry, and volume mesh to mesh the bulk of the geometry.

Among many parameters of the surface mesh, the main parameters controlled as part of the mesh generation in this study were, base size (indicates the target edge length of the triangular element), surface curvature (indicates the number of nodes to be present at the curved surfaces), and surface growth rate (indicates the maximum size ratio of connected mesh edges). Custom controls were also specified on certain faces which required additional refinement. Figure 15 shows the domain before and after the surface remesh. Values of the surface mesh parameters are given in Table 11.

Table 11 Parameters of the surface mesh

Parameter	Value
Base size	0.6mm
Surface curvature	50 points per circle
Surface Growth Rate	1.1

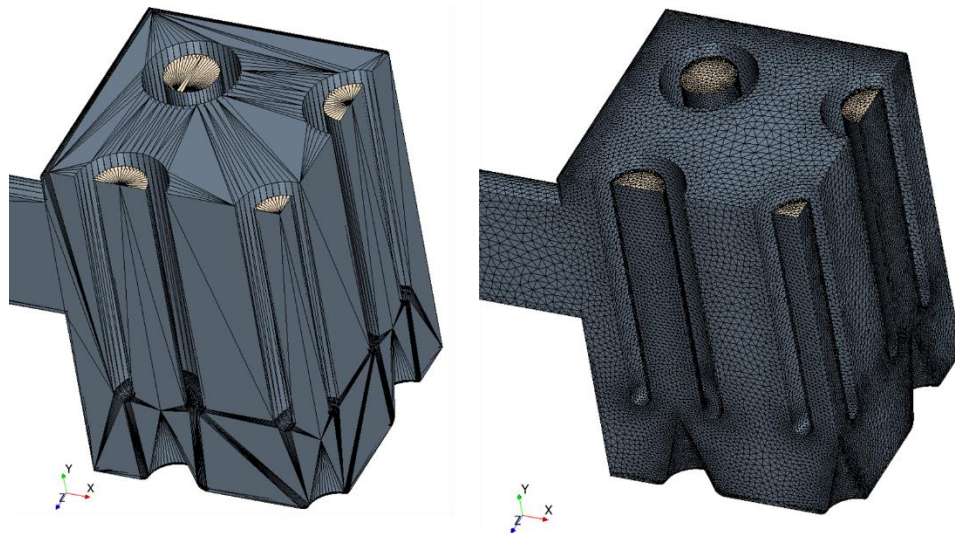


Figure 15 a) Fluid domain before surface mesh b) fluid domain with triangular surface mesh

Surface refinement was specified on the following faces: inlets, outlets, interface between solid and fluid to capture the heat transfer and fluid flow phenomena more efficiently.

Once the surface remeshing was completed, the next step in the mesh generation process was volume meshing. Polyhedral mesh elements were used since they provided balanced solutions for complex domains. In the case of polyhedral mesh, tetrahedral mesh elements were first generated for the input surface, and a dualization scheme was used to mark the centers of tetrahedral elements and midpoints on the boundary edges. Polyhedral elements were then generated starting from the boundary edges. Figure 16 shows the volume mesh cells inside the domain. Like surface mesh, volume mesh also had certain parameters associated with it. These are shown in Table 12.

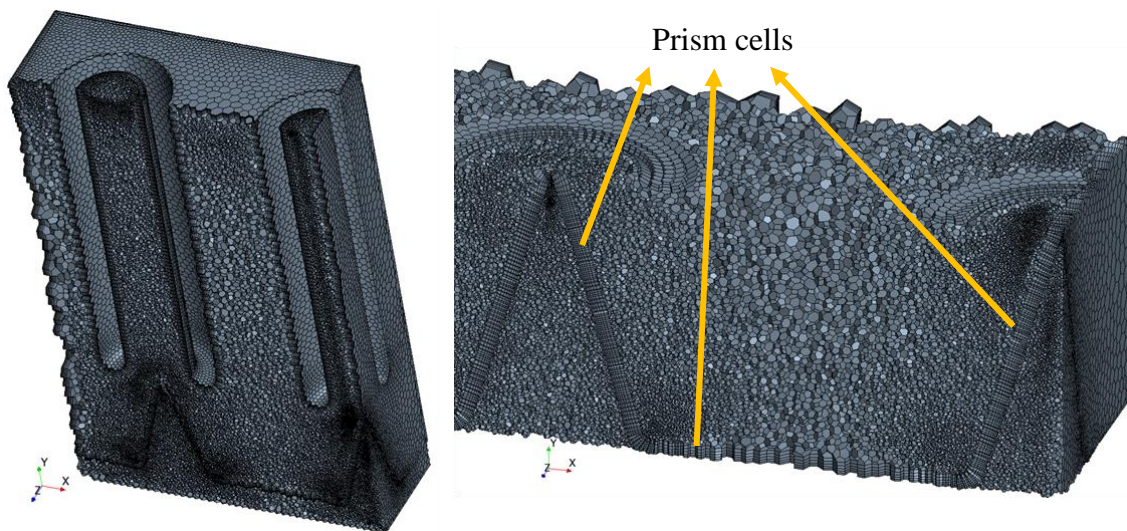


Figure 16 Volume mesh cells

Table 12 Parameters of the volume mesh

Parameter	Value
Base size of polyhedral cells	0.6 mm
No. of prism layers	6
Prism layer stretching	1.2
Prism layer total thickness	0.24 mm
Volume growth rate	1.0

Prism layer mesh model was used along with core volume mesh as shown in Figure 16 to capture the liquid boundary layer and to generate orthogonal prismatic cells next to the wall surfaces or boundaries, especially near the liquid solid interface. Figure 17 shows the interface region with and without the prism layer. This layer of cells was necessary to improve the accuracy of the flow solution.

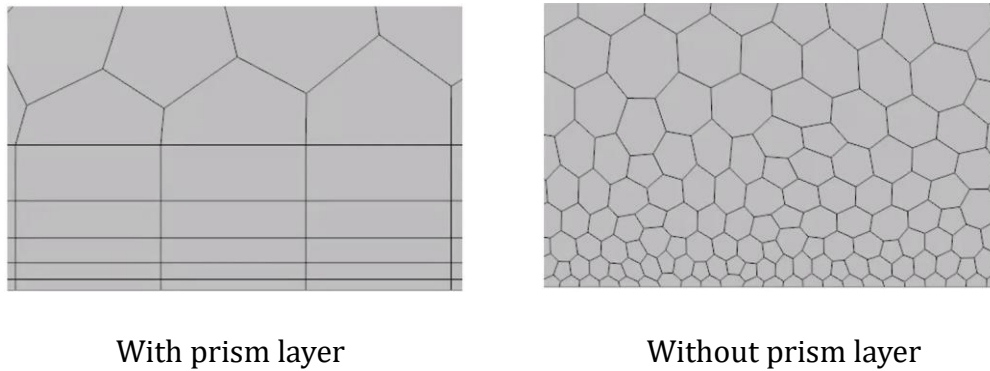


Figure 17 a) interface region with prism layer cells b) interface region without prism layer cells

Since the boundary layer thickness at each point in the flow regime is unknown initially, the number of prism cells and initial wall thickness were estimated using the Blasius solution (for flat plate) given by Equation 31. Reynolds number was calculated based on the maximum surface velocity in the domain estimated using the initial CFD simulation results.

$$t_b = 4.91 \frac{x}{\sqrt{Re_x}} \quad (31)$$

t_b – Thickness of the boundary layer

Re_x – Reynolds number with respect to a characteristic length of x

$$Re_x = \frac{\rho v_s x}{\mu} \quad (32)$$

v_s – Maximum surface velocity in the domain

Considering ‘ s ’ as jet-to-jet spacing and $x = s/2$, was estimated to be 0.2 mm (approx.). Based on the estimated boundary layer thickness, the prism layer stretching, which is the ratio of the thicknesses of adjacent prism layer cells, total thickness of the prism layer region and the number of prism layers were determined. The wall y^+ was monitored during the simulation to capture the first layer of the boundary layer accurately.

To capture turbulence using the κ - ϵ turbulence scheme, the first layer of the prism cells was kept within $y^+ < 5$ (details of the turbulence scheme are discussed in 4.1.4). The prism layer stretching parameter was selected considering the thickness of the first layer of the mesh as shown Table 12.

4.2.7. Boundary conditions for the optimization study

All the boundary conditions were kept constant during the optimization analysis of all the Latin hypercube samples. Table 13 shows the boundary condition values considered during the optimization study. Figure 18 shows the location of the inlet, outlet, and the symmetry planes.

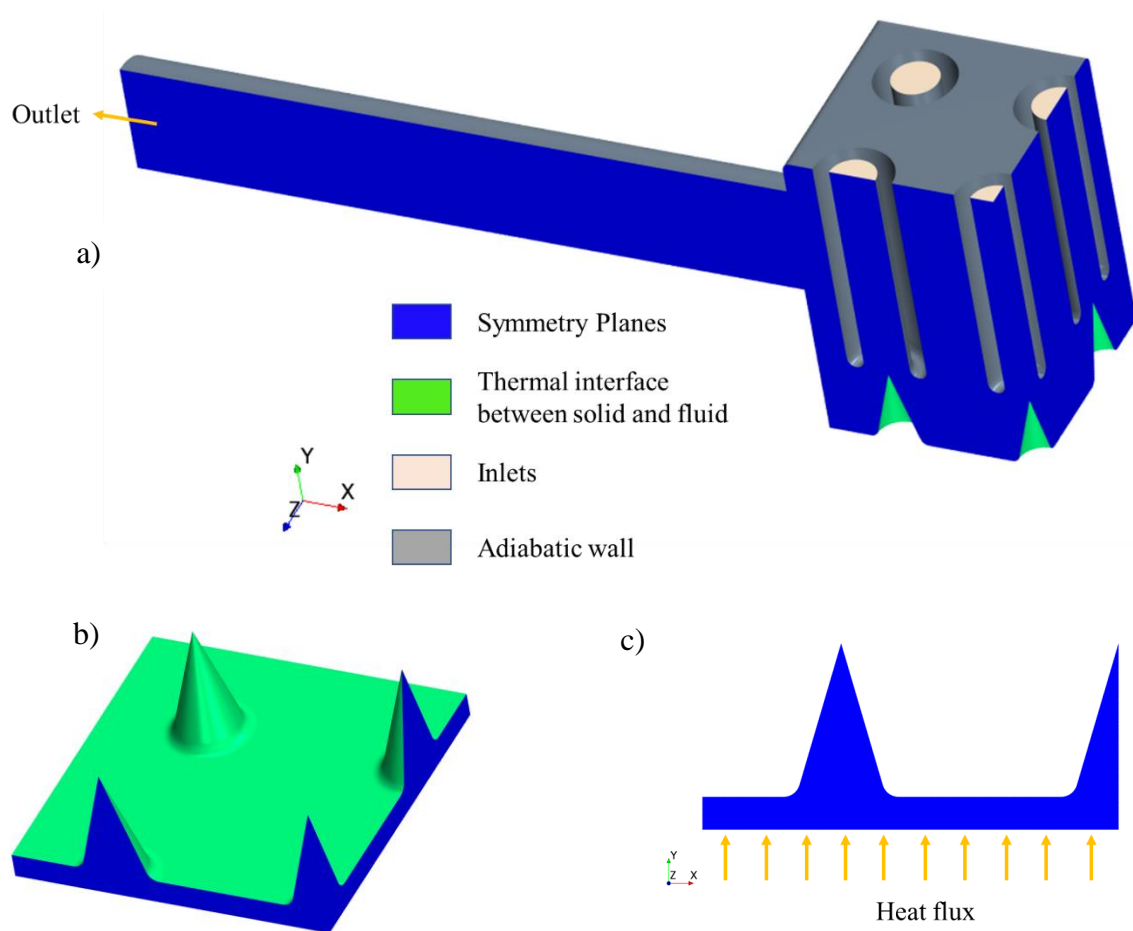


Figure 18 Location of a) boundary conditions in fluid domain and b) solid domain; c) heat flux direction on the heat sink bottom surface

Symmetry boundary condition was applied on the fluid and solid domain faces as shown in Figure 18. A symmetry plane boundary condition represents an imaginary plane of symmetry and was used to reduce the size of the computational domain in locations where geometry and flow were symmetric.

Table 13 Boundary conditions of fluid and solid domain

Faces	Physics specification	Value
Inlet	Mass flow inlet	0.01 kg/s
Outlet	Pressure outlet	0 Pa gauge pressure
Symmetry	Zero shear stress, Slip wall	
Adiabatic walls	No heat transfer	
Bottom surface of heat sink	Heat flux	15 W/cm ²

Mass flow inlet was applied to the inlet faces where the mass flow rate was divided according to the surface area of the face. The temperature of the inlet water was set at 300 K. All the outer faces excluding inlets, outlet, and bottom surface of heat sink, were adiabatic. The adiabatic boundary condition prevented any heat and mass transfer to occur at these faces.

4.3. Heat sinks comparative analysis

In addition to the optimization of conical pin heat sink, comparative analysis of various heat sinks as shown in Table 1 was conducted. The manifold obtained from the optimization of conical pin heat sink was taken and coupled with various pin fin heat sink configurations to understand the merits, demerits and factors affecting the heat transfer characteristics.

4.3.1. Domain selection for heatsink comparative analysis

To perform the comparative analysis of different heatsinks shown in Table 1, a detailed numerical domain was developed to mimic the experimental test setup. Figure 19 shows the cut section view of the components of the multi jet array impingement cooling system considered for CFD analysis.

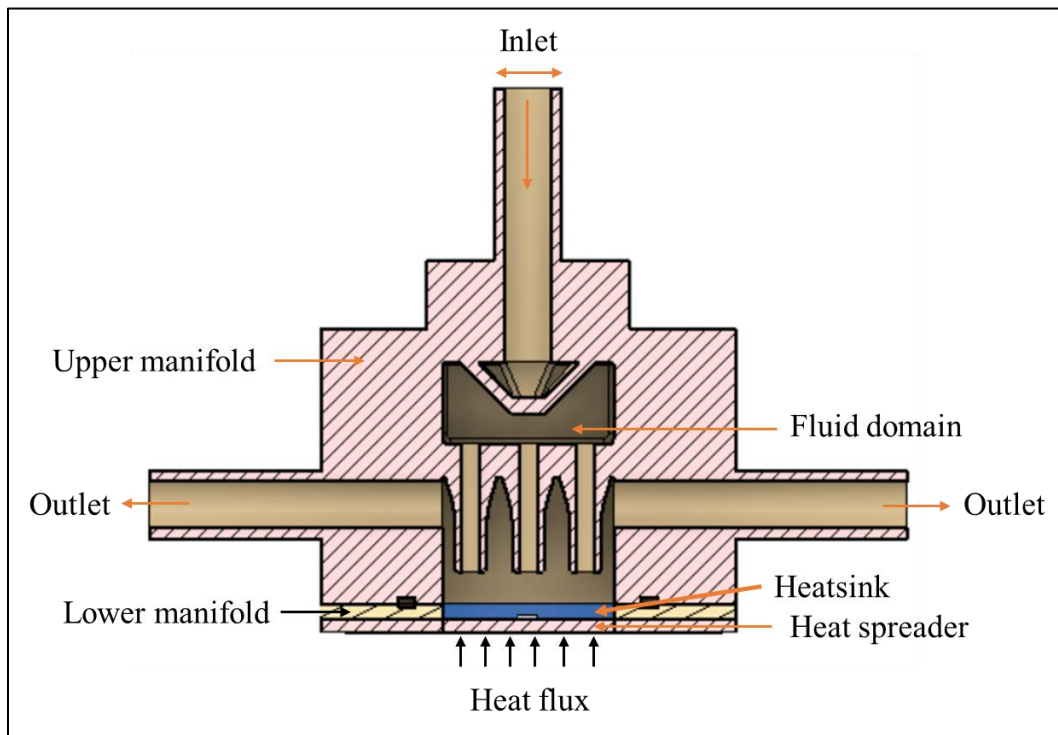


Figure 19 Components considered for comparative study of heatsinks

The CFD domain used in the comparative analysis study consisted of upper and lower manifolds, copper heat spreader, copper heat sink (various heat sink designs are shown in Table 1) and extracted fluid domain. The inlet and outlet extensions were chosen such that the numerical setup could resemble the experimental conditions. The material properties of each component considered for CFD analysis were discussed in section 4.1.3.

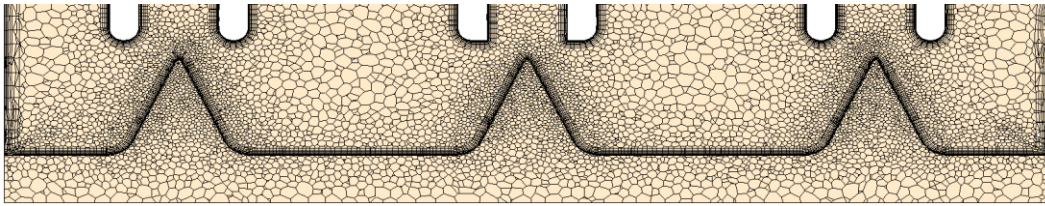
4.3.2. Mesh generation for comparative analysis of heat sinks

Similar approach as described in section 4.1.4 was implemented for mesh generation in case of comparative analysis. The surface and volume mesh parameters are shown in Table 14. Figure 20 shows the section view of volume mesh generated for all the heat sinks.

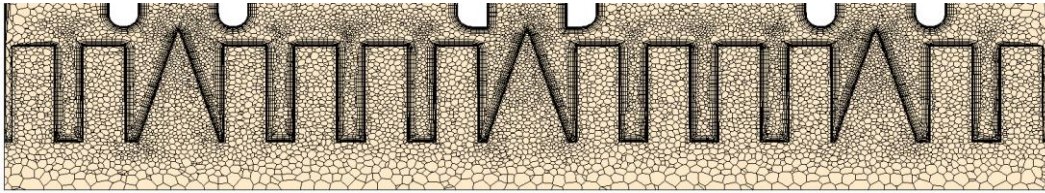
Table 14 Surface and volume mesh parameters in comparative analysis study

Parameter	Value
Base size	0.6 mm
Surface curvature	100 points per circle
Surface Growth Rate	1.2
Base size of polyhedral cells	0.4 mm
No. of prism layers	8
Prism layer stretching	1.25
Prism layer total thickness	0.3 mm
Volume growth rate	1.1

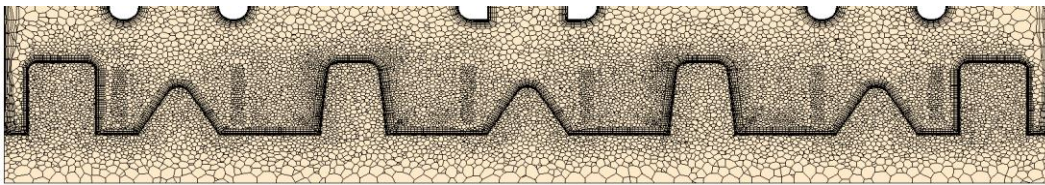
Conical pin fin:



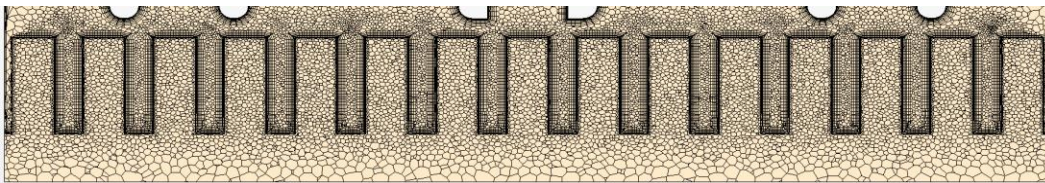
Conical and Square pin fins:



Radially aligned pin fin:



Square pin fin:



Rectangular pin fin:

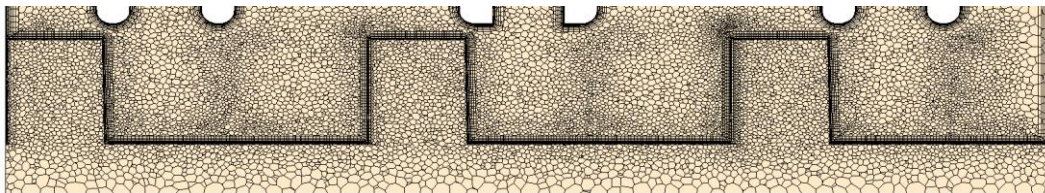


Figure 20 Cross section view of volume mesh generated for all heat sinks considered for

comparative analysis

4.3.3. Boundary conditions for heat sink comparative analysis

All the boundary conditions were kept constant during the comparative analysis of each heat sink. Since the CFD analysis was done to mimic the experimental setup, boundary conditions were chosen accordingly. The bottom surface of the heat spreader was given the same heat flux boundary condition. Thermal interfaces were created between all the components of the multi jet impingement system. Mass flow inlet boundary conditions were specified at the inlet with an inlet liquid temperature of 300 K. Pressure outlet boundary condition was specified at both the outlets with a gauge pressure of 0 Pa. Outer surfaces of the upper manifold, and lower manifolds were provided with adiabatic boundary conditions since the experimental setup was well insulated to prevent any heat loss to the surroundings.

A contact thermal resistance equivalent to 0.01 mm of thermal interface material was provided between heat spreader and heat sink. The value of the contact thermal resistance was calculated using Equation 33.

$$R_c \cdot A_s = \frac{l_{TIM}}{k_{TIM}} \quad (33)$$

R_c – contact thermal resistance $\left(\frac{K}{W}\right)$

A_s – Surface area of coverage = $6.45 \cdot 10^{-4} \text{ m}^2$

l_{TIM} – thickness of thermal interface material = 10^{-5} m

k_{TIM} – thermal conductivity of thermal interface material = $2.5 \frac{W}{m \cdot K}$

4.4. Topology optimization

Topology optimization was conducted using Star-CCM+ adjoint solver as part of the study. Adjoint solver can be used to get a deep understanding of the effects of different parameters on the geometry of the system design. The mesh morphing feature was used to modify the shape of the volume mesh to achieve an optimal shape. The adjoint solver accounts for the sensitivity of objectives (cost function) with respect to the input parameters such as design variables, boundary conditions, and surface sensitivity. Design parameters 'D', define the mesh coordinates of a shape $x(D)$. A mesh deformation strategy aims at deforming the baseline mesh based on gradients of the objective function with respect to $x(D)$ to develop new shapes. It uses a radial basis function morpher algorithm.

At first, the CFD simulation was run using coupled flow and energy solvers. Once the simulation meets an acceptable convergence criterion, the adjoint solver was activated. The cost function in this study was set for minimizing the average surface temperature of the heat sink bottom surface. The adjoint solver then computed the sensitivity of the objective function with respect to the surface mesh. The final step was deforming the mesh according to the sensitivities calculated by the adjoint solver. For this, a user defined field function, Equation 34 was created to morph the mesh geometry. The field function was based on first order steepest descent approach with a given step size.

$$[X^*] = [X] + k \cdot [M] \quad (34)$$

$[X^*]$ – matrix of deformed surface mesh displacement

$[X]$ – matrix of current surface mesh displacement

k – step size

[M] – Mesh sensitivity matrix

The algorithm for adjoint optimization or topology optimization approach is shown in Figure 21.

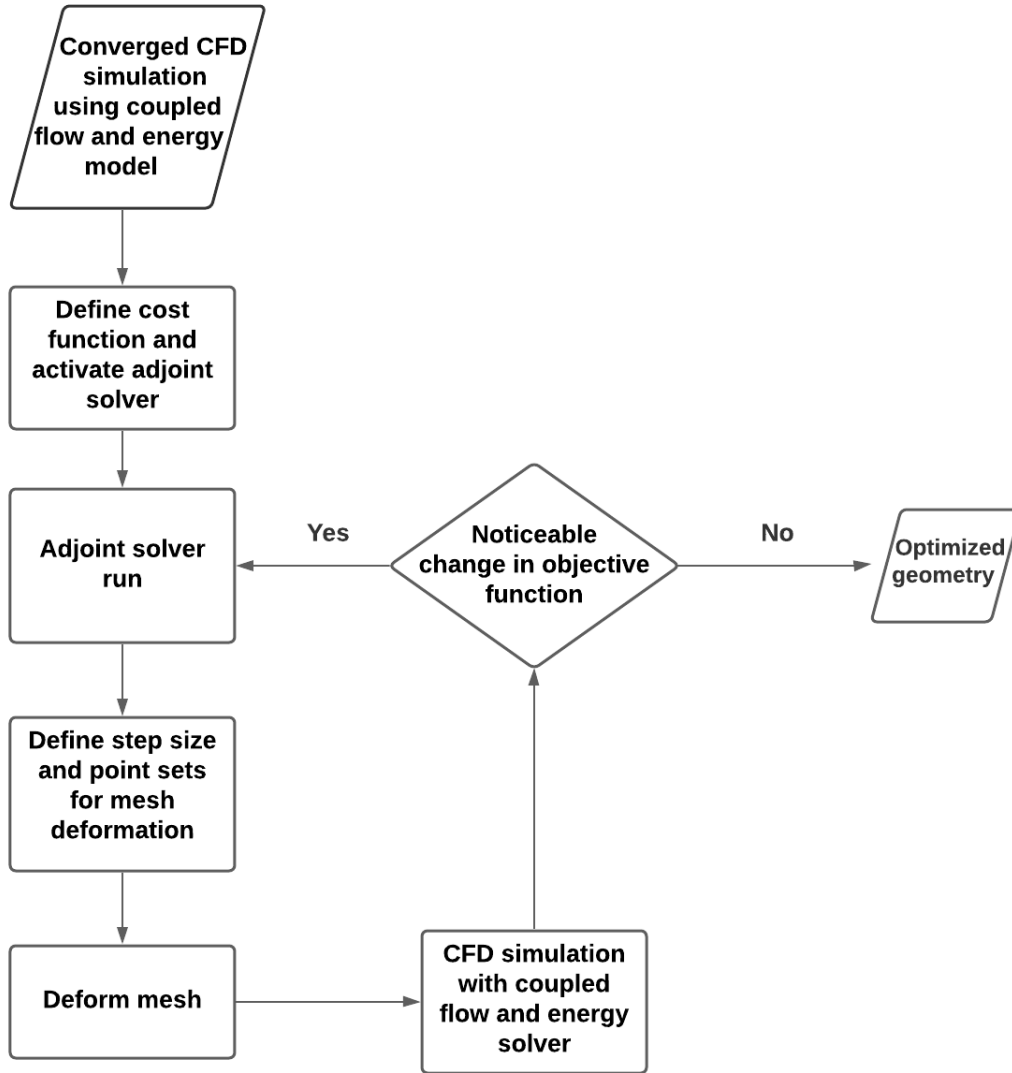


Figure 21 Adjoint solver-based topology optimization algorithm

With the use of the adjoint solver in Star CCM+, the optimal topology of conical pin heat sink was obtained and discussed in further detail in Chapter 5.

4.5. Methodology and algorithm for grid independence study of multi-jet impingement cooling system

In order to obtain reliable CFD results, the simulations needed to be independent of the grid or mesh. This was achieved by performing a grid independence study. The polygonal meshing algorithm was used to generate multiple surface and volume refinements. As part of the refinement process, the normalized base size given by Equation 35 was used.

$$\delta = \left(\frac{V_d}{N}\right)^{1/3} \quad (35)$$

where,

δ – normalized base size

V_d – volume of the mesh domain

N – number of mesh elements in the CFD domain

To ensure that the simulation results were grid independent, the grid convergence index (GCI) was calculated for each set of results. The algorithm for calculating the grid convergence index (GCI) is shown in Figure 22. GCI is an ASME standard way to report grid convergence quality [48].

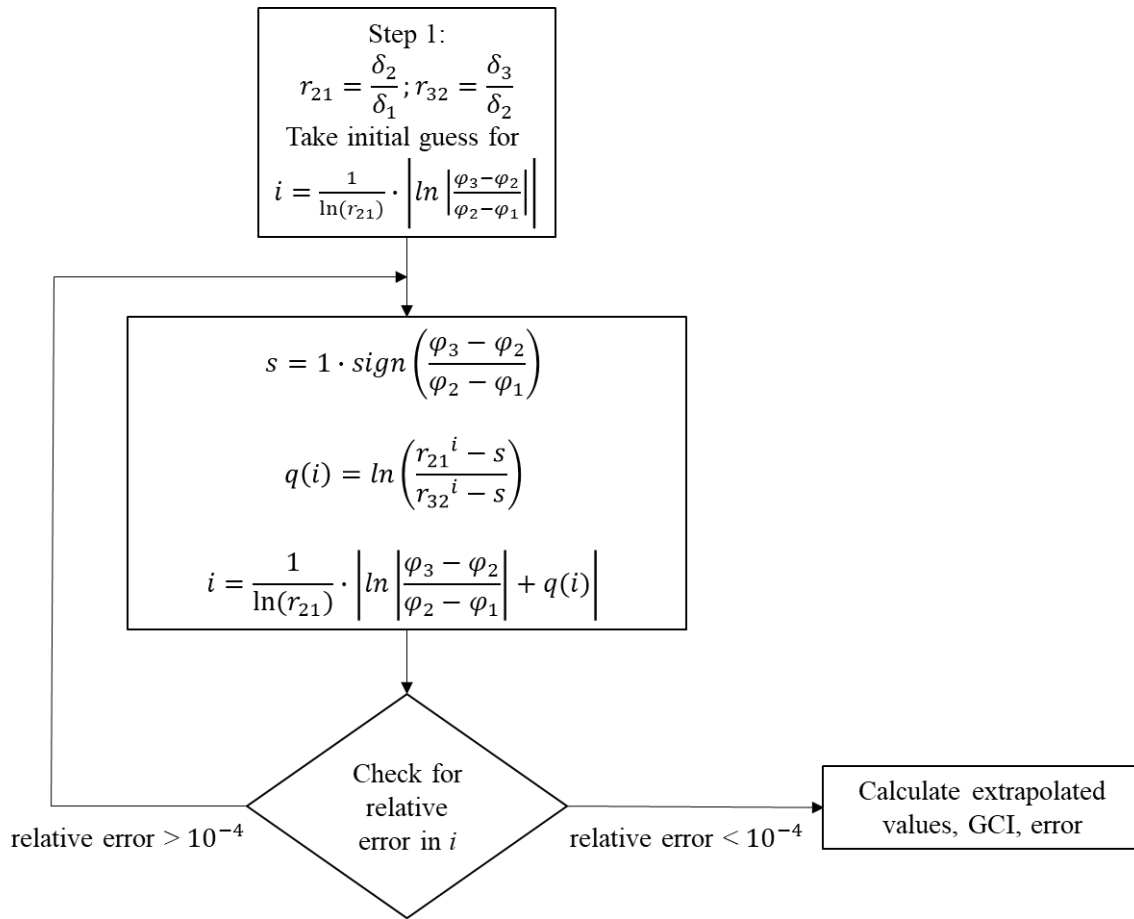


Figure 22 Grid convergence index algorithm (Adapted from [48])

where,

δ_m –normalized base size given by Equation 35 for m^{th} grid

φ_m –function considered for grid convergence (temperature of heat sink bottom surface)

for m^{th} grid

Once the numerical simulation results attained the defined convergence using GCI, extrapolated function values (heat sink bottom surface temperature) were calculated based on the following equations.

$$\varphi_{\text{ext}} = \frac{r_{21}^i \cdot \varphi_1 - \varphi_2}{r_{21}^{i-1}} \quad (36)$$

$$\text{GCI} = \frac{F_s}{r_{21}^{i-1}} \cdot \frac{\varphi_2 - \varphi_1}{\varphi_1} \quad (37)$$

where,

F_s –factor of safety (generally $F_s = 1.25$)

The convergence results including CGI values are shown in the next chapter

5. RESULTS AND DISCUSSION

In this chapter, the simulation results for all the jet impingement cases are presented and discussed based on the main objectives of the study. As part of the CFD simulations, first a grid independence study was conducted to ensure that the results were grid independent. The grid independent results including GCI results in case of flat plate heat sink configuration are presented. Furthermore, the optimized grid CFD pressure drop results were compared with the experimental data provided by Nikhil Pundir [45]. Also, the effect of the flow distributor structure on uniform flow distribution is discussed.

The results and discussion of parametric analysis or design space exploration study are presented as well. Effects of various design parameters on the thermal and pressure drop characteristics are discussed in detail. Furthermore, single, and multi-objective optimization studies were conducted on the conical pin heat sink configuration. The results of topology optimization of the conical heat sinks are discussed in detail as well.

Another major aspect of this study was the comparative analysis of various heat sink configurations shown in Table 1. Numerical simulation results obtained as part of the comparative analysis study are discussed in detail in this chapter as well.

5.1. Numerical grid independence in the case of flat plate heat sink system design

As mentioned in section 4.5, the normalized base size of 4 different grid sizes was calculated as an input to the grid convergence algorithm. Table 15 shows the mesh count and normalized base size of the individual meshes.

Table 15 Mesh count and normalized base size for grid independence study of flat plate heat sink

S. No	Mesh count	Normalized base size
1	607125	0.626 mm
2	846603	0.560 mm
3	1375613	0.477 mm
4	1759406	0.439 mm

The CFD simulations were conducted for a flat plate heat sink configuration with the boundary conditions and CFD domain discussed in section 4.3. Figure 23 shows the CFD results of heat sink bottom surface temperature with respect to mesh count for multiple flow rates. The grid convergence and extrapolated temperature results obtained using the algorithm shown in Figure 23 at various flow rates are shown in Table 16.

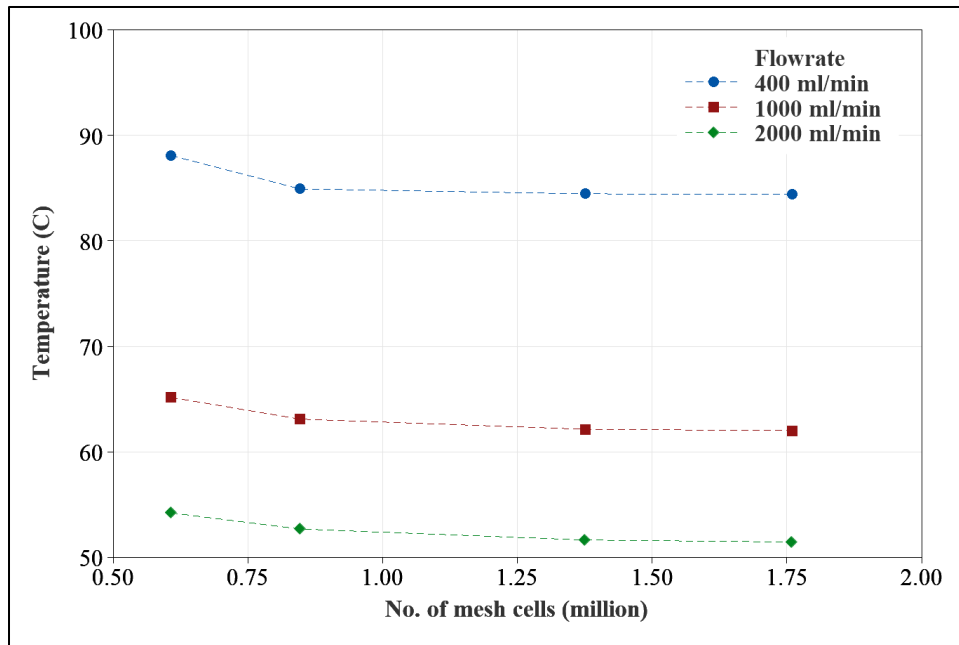


Figure 23 Average temperature of heat sink bottom surface with respect to number of mesh elements

Table 16 GCI and extrapolated temperature values at various flow rates

Flowrate	Parameter		
	GCI_i	GCI_{i+1}	Extrapolated temperature
400 ml/min	5.3 %	1.9 %	84.15 °C
1000 ml/min	11.8 %	2.1 %	61.26 °C
2000 ml/min	23.4 %	3.4 %	50.08 °C

As shown in Table 16, the refinement of grid led to desirable GCI values.

5.2. Experimental validation of pressure drop in case of flat plate heat sink

Figure 24 shows the experimental and CFD simulation data of pressure drop across the multi-jet array cooling system in case of flat plate heat sink configuration.

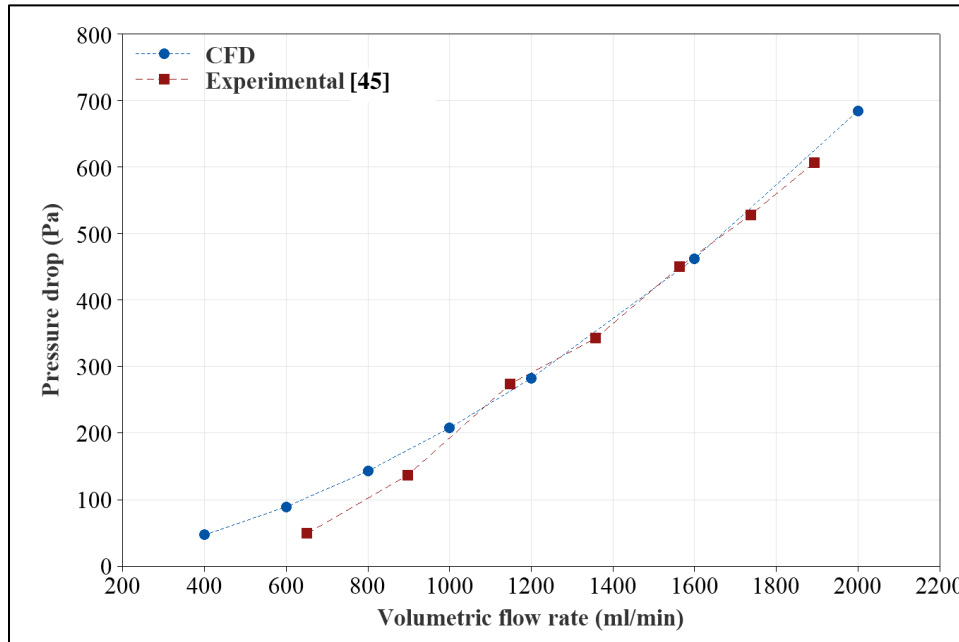


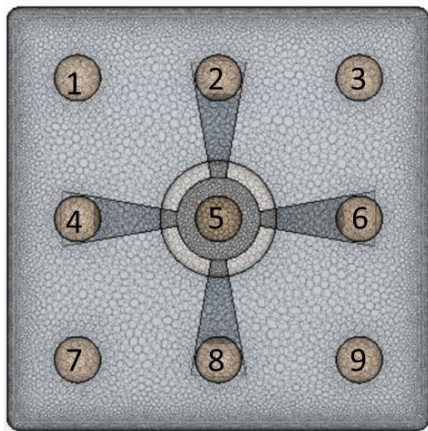
Figure 24 Pressure drop across the multi-jet impingement cooling system with flat plate heat sink

Figure 24 shows that the numerical results agreed well with the experimental results. CFD results were marginally over predicting the pressure drop across the system at lower flow rates.

5.3. Validation of effectiveness of using flow distributor structure across cylindrical jets in multi-jet cooling system

As discussed in section 3.1, a flow distributor was used in the upstream header to maintain uniform flow through the nine cylindrical jets as shown in Figure 9. A fluid domain with 1 inlet and 9 outlets was considered for the CFD simulations. The position of outlets and cut section is shown in in Figure 25. Mass flow rate at the inlet was set at 0.01 kg/s (with an equivalent volume flow rate of 600 ml/min). Velocity contours are shown in Figure 26. As Figure 26 shows, the velocity contours are relatively uniform when a flow distributor is used. Figure 27 shows the variation of flow rate across the nine jets with respect to the outlet position.

a) Positions of jets



b) Position of cut section

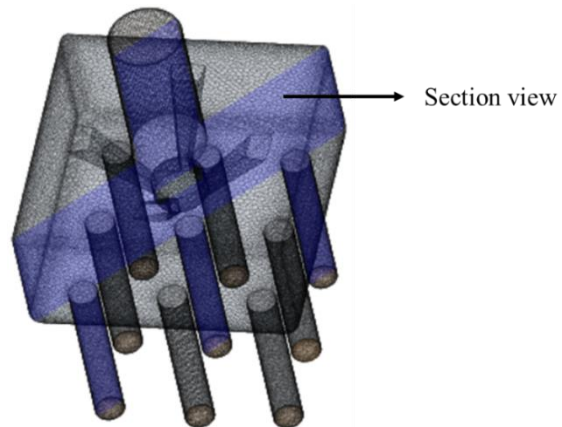


Figure 25 Positions of a) jets, and b) cut section

a) Without flow distributor

b) With flow distributor

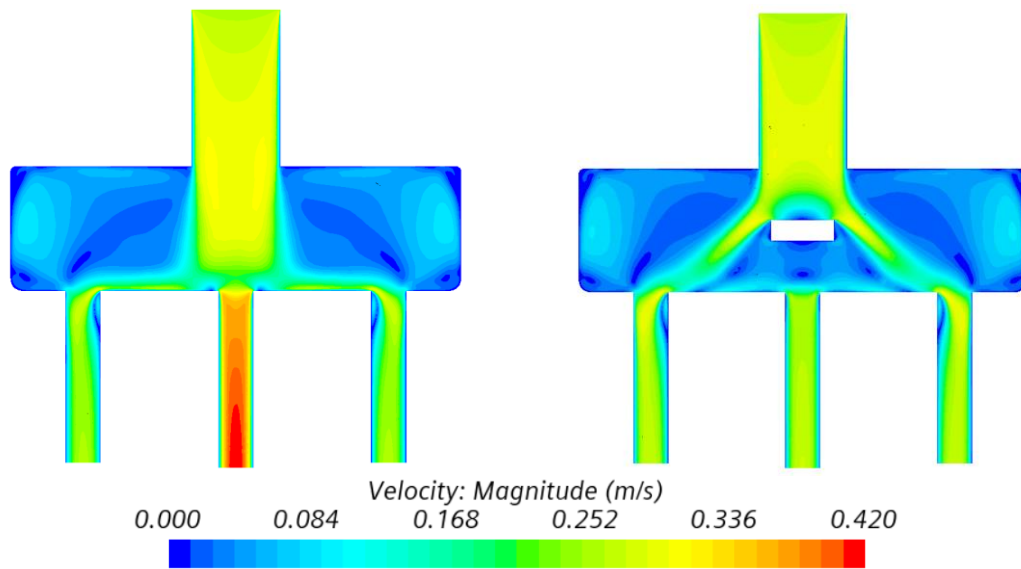


Figure 26 Velocity contours of the cut section a) without flow distributor and b) with flow distributor

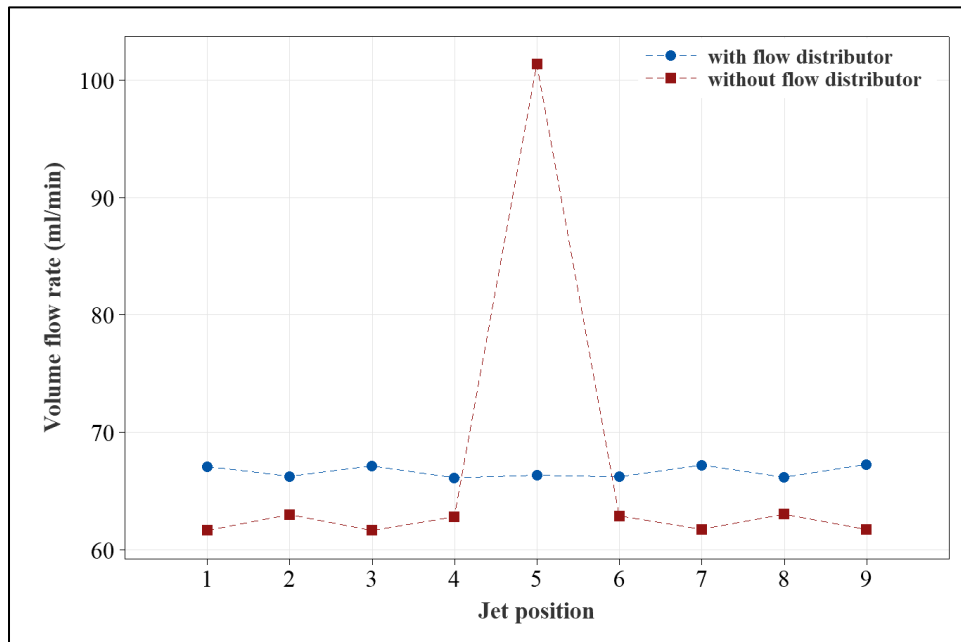


Figure 27 Variance of volumetric flow rate across the nine cylindrical jets

As Figure 27 shows, the flow distributor structure generates uniform flow rate across the nine cylindrical jets.

5.4. Parametric analysis of the conical pin heat sink in multi-jet cooling system

Initial design space exploration or parametric analysis was carried out to understand the effect of each individual parameter on the heat transfer and flow characteristics of the multi jet array impingement cooling system. The parameters considered for this study are shown in Table 2. CFD simulations were conducted with the boundary conditions and solver settings discussed in sections 4.1.4 and 4.2.7. Since the thermal approach and pumping power were chosen as the objective functions for the parametric and optimization studies, the numerical results were presented in terms of these objective functions. Heat transfer coefficient based on liquid-side surface area was also compared with respect to the design parameters. In addition, temperature and velocity contours of the designs corresponding to the minimum and maximum thermal approach values are shown for each case. Furthermore, to simplify the optimization part of the study, the parameters which did not affect the objective functions were not considered in the single objective and multi-objective optimization.

5.4.1. Effect of jet diameter on thermal approach and pumping power

The jet diameter was varied ranging from the lower bound to upper bound. The corresponding design vectors are shown below.

$$\begin{bmatrix} x_1 \\ x_2 \\ x_3 \\ x_4 \\ x_5 \\ x_6 \end{bmatrix} = \begin{bmatrix} \text{Jet Diameter} \\ \text{Tube height} \\ \text{Impingement Height} \\ \text{Extraction Height} \\ \text{Cone Height} \\ \text{Cone Angle} \end{bmatrix} = \begin{bmatrix} \mathbf{2 \text{ mm} - 5 \text{ mm}} \\ 14 \text{ mm} \\ 4.5 \text{ mm} \\ 8.5 \text{ mm} \\ 4 \text{ mm} \\ 60^\circ \end{bmatrix}$$

Figure 28 shows the variation of thermal approach (R_θ) and pumping power (\dot{W}) with respect to jet diameter (d_j). Figure 28 shows that, the thermal approach increases with increase in jet diameter. The convective heat transfer coefficient at the solid liquid interface is directly proportional to the velocity of fluid. The jet velocity is inversely proportional to jet diameter for the same volumetric flow rate. With the increase in jet diameter, the jet velocity decreases, and the heat transfer coefficient decreases, as shown in Figure 29. The increase in the thermal approach of the system is attributed to decrease in heat transfer coefficient in this case as shown in Figure 29. Figures 30a and 30b show the velocity contours of the cross-section and Figures 30c and 30d show the temperature contours of the solid and liquid interface.

The pressure drop across the multi-jet cooling system is inversely proportional to the jet diameter for the same volumetric flow rate. Since pumping power of the multi jet cooling system is directly proportional to pressure drop across the system for the same volumetric flow rate, pumping power also decreases with increase in jet diameter as shown in Figure 28.

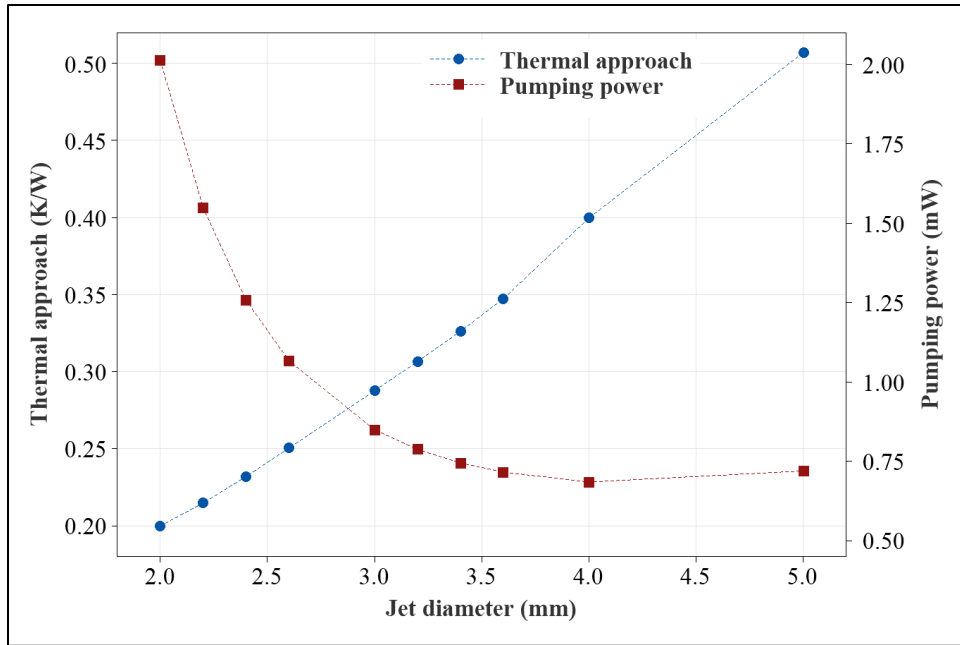


Figure 28 Variation of thermal approach and pumping power with jet diameter

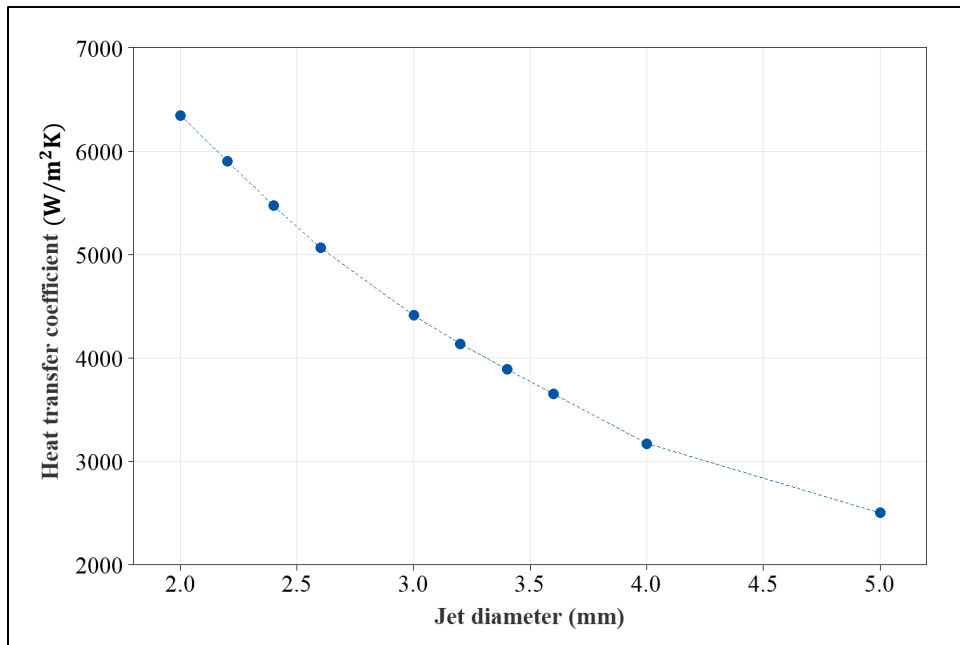
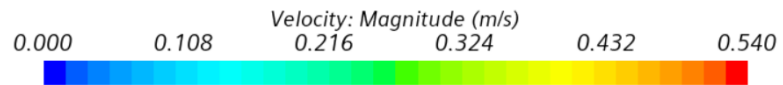
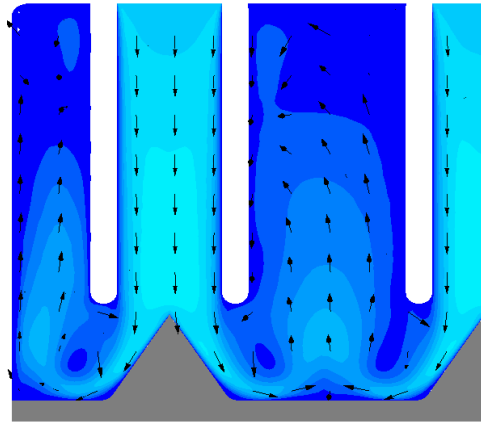
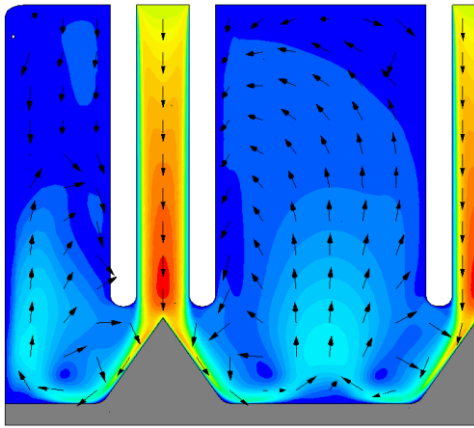


Figure 29 Variation of heat transfer coefficient with jet diameter

a) $d_j = 2 \text{ mm}$

b) $d_j = 4 \text{ mm}$



c) $d_j = 2 \text{ mm}$

d) $d_j = 4 \text{ mm}$

$$T_{s,avg} = 46.3 \text{ } ^\circ\text{C} ; \sigma = 1.34 \text{ } ^\circ\text{C}$$

$$T_{s,avg} = 66.7 \text{ } ^\circ\text{C} ; \sigma = 1.42 \text{ } ^\circ\text{C}$$

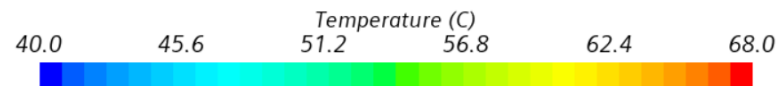
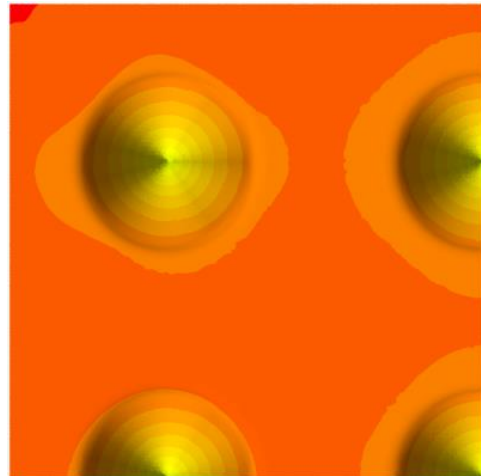
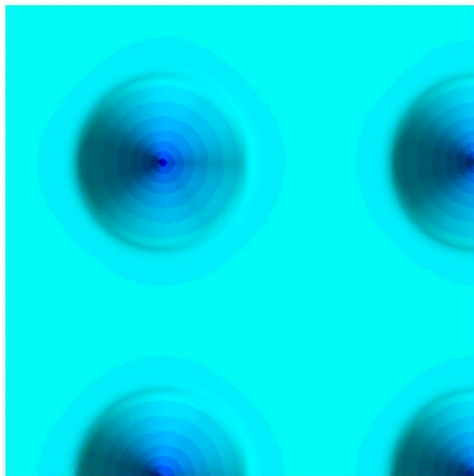


Figure 30 Velocity contours of cross section for Jet diameter of a) 2 mm b) 4 mm
Temperature contours of solid-liquid interface for Jet diameter of c) 2 mm d) 4 mm

5.4.2. Effect of impingement height on thermal approach and pumping power

The impingement height or jet-to-target spacing was varied from the lower bound to the upper bound. Design vectors corresponding to this study are shown below:

$$\begin{bmatrix} x_1 \\ x_2 \\ x_3 \\ x_4 \\ x_5 \\ x_6 \end{bmatrix} = \begin{bmatrix} \text{Jet Diameter} \\ \text{Tube height} \\ \text{Impingement Height} \\ \text{Extraction Height} \\ \text{Cone Height} \\ \text{Cone Angle} \end{bmatrix} = \begin{bmatrix} 2.6 \text{ mm} \\ 14 \text{ mm} \\ 3.5 \text{ mm} - 7 \text{ mm} \\ 8.5 \text{ mm} \\ 3 \text{ mm} \\ 60^\circ \end{bmatrix}$$

Figure 31 shows the effect of impingement height (h_{im}) on thermal approach (R_θ) and pumping power (\dot{W}). It can be observed that the thermal approach increases with increase in impingement height as shown in Figure 31. Due to the increase in impingement height, fluid velocity decreases due to availability of space between the heat sink pin and the outlet of the cylindrical jet. Since heat transfer coefficient is directly proportional to the fluid velocity at the surface, it decreases with increase in impingement height as shown in Figure 32. Figure 34 shows the velocity and surface temperature contours for impingement heights of 3.5 mm and 7.5 mm. Figure 31 also shows that the variation of pumping power with respect to the impingement height is not significant.

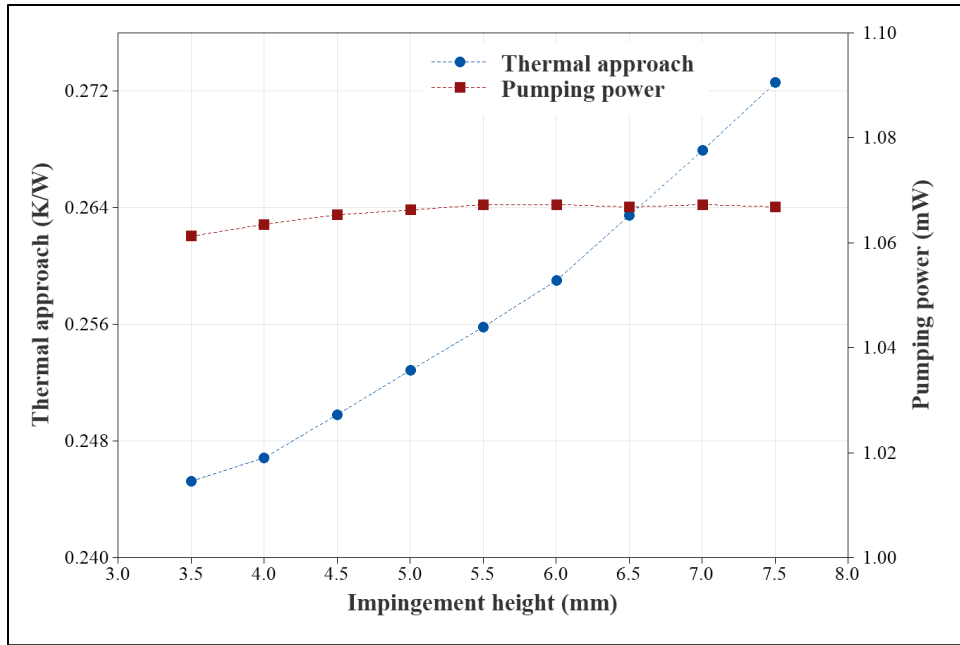


Figure 31 Variation of thermal approach and pumping power with impingement height

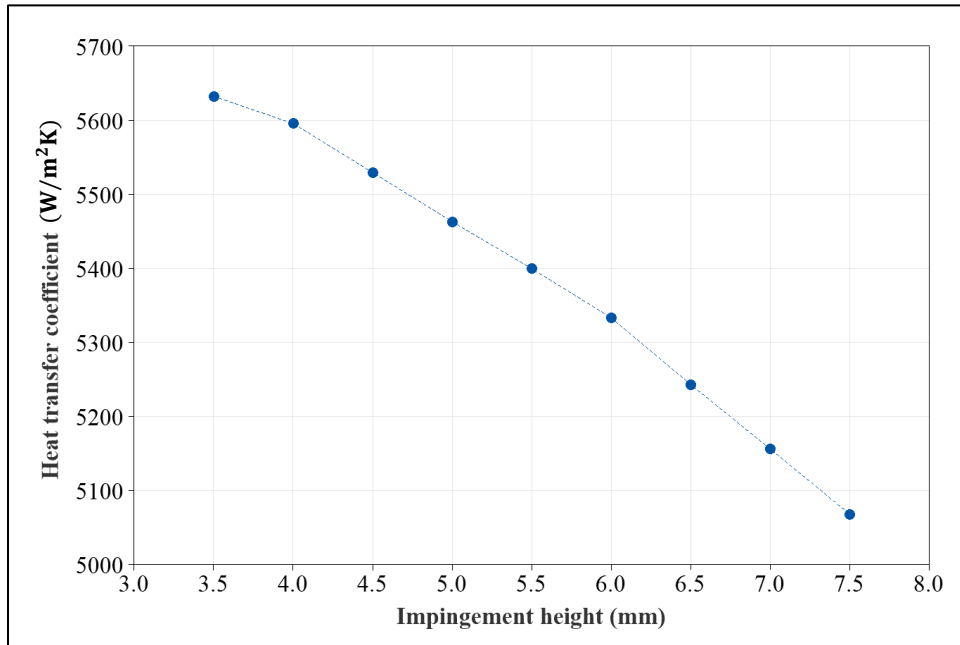
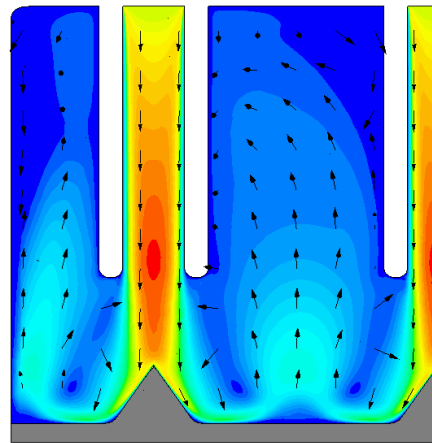
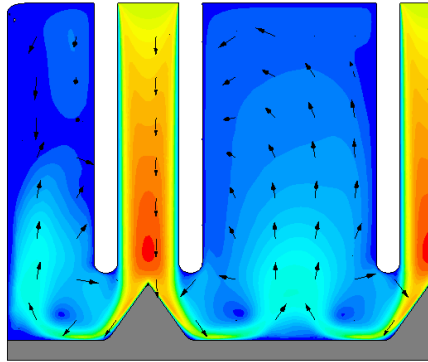


Figure 32 Variation of heat transfer coefficient with impingement height

a) $h_{im} = 3.5$ mm

b) $h_{im} = 7.5$ mm



c) $h_{im} = 3.5$ mm

d) $h_{im} = 7.5$ mm

$T_{s,avg} = 51.7$ °C ; $\sigma = 1.04$ °C

$T_{s,avg} = 54.4$ °C ; $\sigma = 1.12$ °C

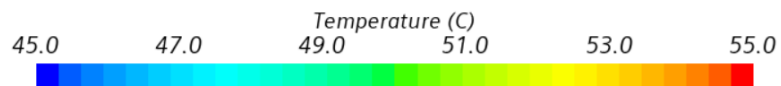
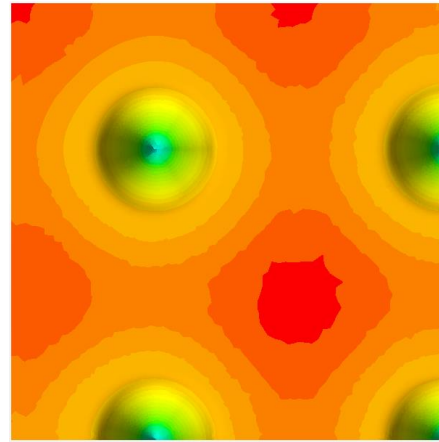
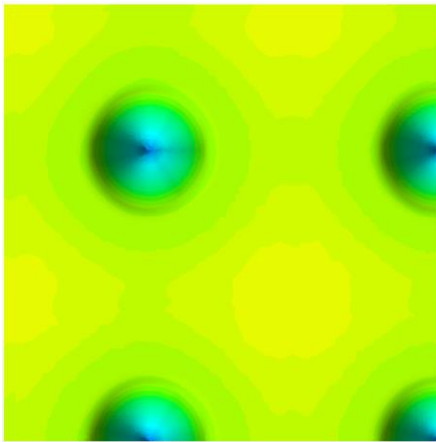


Figure 33 Velocity contours of cross section for impingement height of a) 3.5 mm b) 7.5 mm; Temperature contours of solid-liquid interface for impingement height of c) 3.5 mm

d) 7.5 mm

5.4.3. Effect of cone height on thermal approach and pumping power

Further CFD simulations were conducted in which the cone height was varied from the lower bound to the upper bound. The design vectors corresponding to this study are shown below.

$$\begin{bmatrix} x_1 \\ x_2 \\ x_3 \\ x_4 \\ x_5 \\ x_6 \end{bmatrix} = \begin{bmatrix} \text{Jet Diameter} \\ \text{Tube height} \\ \text{Impingement Height} \\ \text{Extraction Height} \\ \text{Cone Height} \\ \text{Cone Angle} \end{bmatrix} = \begin{bmatrix} 2.6 \text{ mm} \\ 14 \text{ mm} \\ 4 \text{ mm} - 7 \text{ mm} \\ 8.5 \text{ mm} \\ 1 \text{ mm} - 6 \text{ mm} \\ 60^\circ \end{bmatrix}$$

Figure 34 shows the effect of cone height (h_c) on thermal approach (R_θ) and pumping power (\dot{W}). It was observed that the thermal approach reaches a minimum at a cone height of 3.5 mm. However, the heat transfer coefficient was found to be inversely proportional to the cone height as shown in Figure 35. Thermal approach, which is an indicator of overall convective heat transfer across the multi-jet cooler system depends on two parameters, the heat transfer coefficient, and the liquid-side surface area between fluid and solid interface. Even though the heat transfer coefficient was found to be monotonously decreasing with cone height, due to the increase in surface area, thermal approach attains a minimum at a cone height of 3.5 mm. This trend was found to be consistent with various impingement heights as shown in Figures 34 and 35. Pumping power was found not to vary significantly with cone height. Figure 36 shows the velocity and temperature contours for cone heights of 1.5 mm and 3.5 mm.

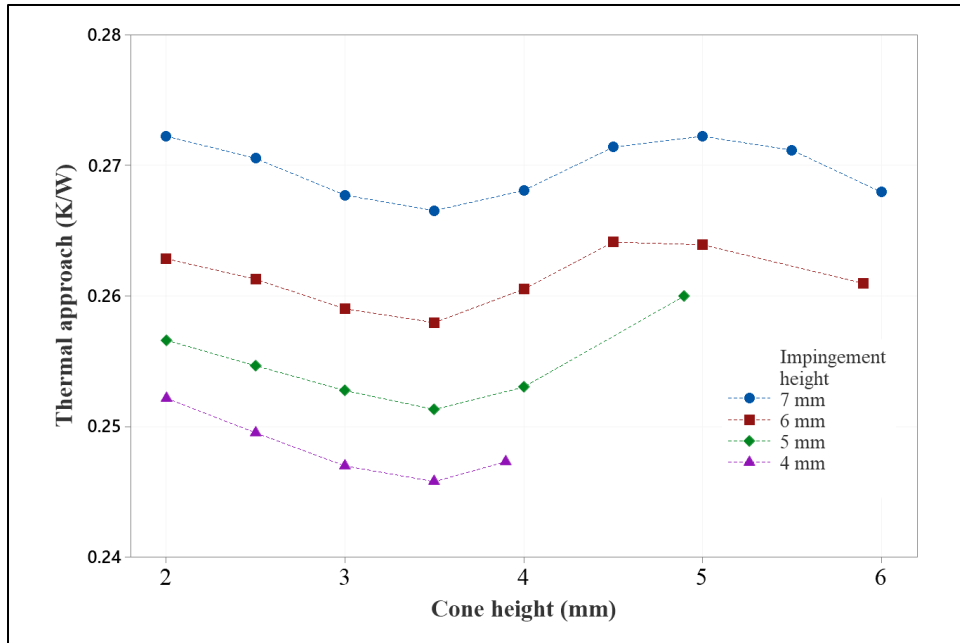


Figure 34 Variation of thermal approach and pumping power with cone height

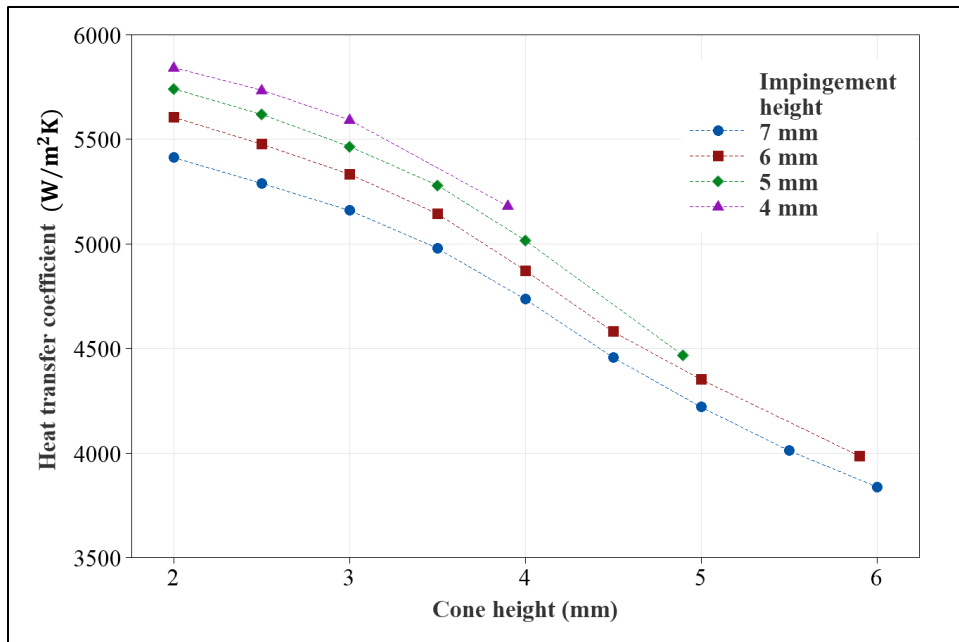
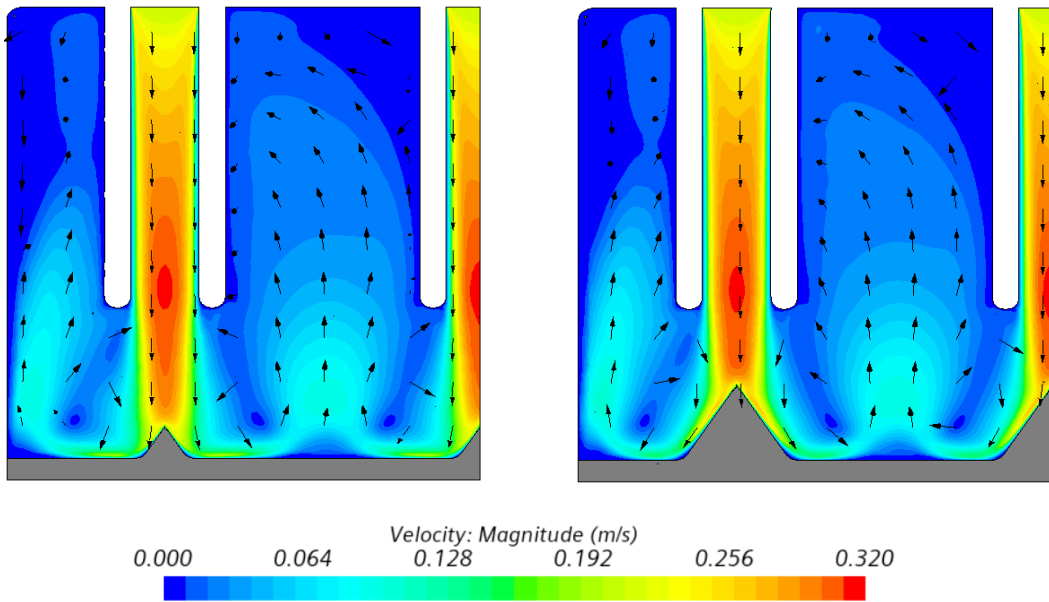


Figure 35 Variation of heat transfer coefficient with cone height

a) $h_c = 1.5$ mm

b) $h_c = 3.5$ mm



c) $h_c = 1.5$ mm

d) $h_c = 3.5$ mm

$T_{s,avg} = 54.6$ °C ; $\sigma = 0.65$ °C

$T_{s,avg} = 53.4$ °C ; $\sigma = 1.27$ °C

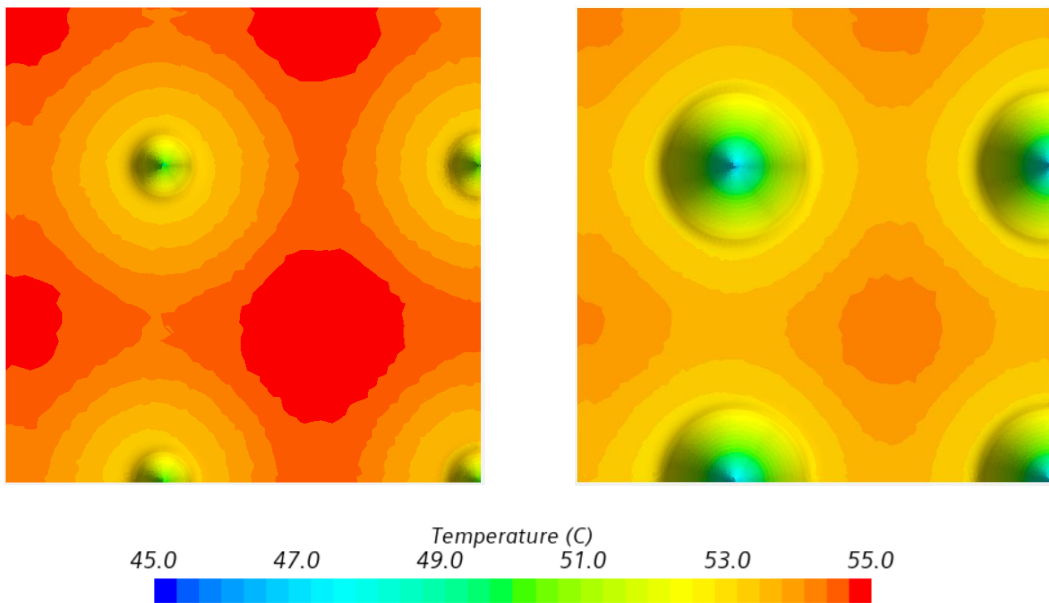


Figure 36 Velocity contours of cross section for cone height of a) 1.5 mm b) 3.5 mm;
Temperature contours of solid-liquid interface for cone height of c) 1.5 mm d) 3.5 mm

5.4.4. Effect of cone angle on thermal approach and pumping power

Similar to the cone height, cone angle was also varied from the lower bound to upper bound. The design vectors corresponding to this study are shown below:

$$\begin{bmatrix} x_1 \\ x_2 \\ x_3 \\ x_4 \\ x_5 \\ x_6 \end{bmatrix} = \begin{bmatrix} \text{Jet Diameter} \\ \text{Tube height} \\ \text{Impingement Height} \\ \text{Extraction Height} \\ \text{Cone Height} \\ \text{Cone Angle} \end{bmatrix} = \begin{bmatrix} 2.6 \text{ mm} \\ 14 \text{ mm} \\ 4.5 \text{ mm} \\ 8.5 \text{ mm} \\ 4 \text{ mm} \\ 50^\circ - 75^\circ \end{bmatrix}$$

Figure 37 shows the effect of cone angle (θ_c) on thermal approach (R_θ) and pumping power (\dot{W}). Due to the change in liquid-side surface area between the solid and liquid interface, the variation of thermal approach with cone angle attains a maximum at a 55° as shown in Figure 37. The heat transfer coefficient was found to increase monotonically with cone angle as shown in Figure 38. Pumping power was found not to vary significantly with cone angle. Figure 39 shows the velocity and temperature contours for cone angles of 55° and 75° .

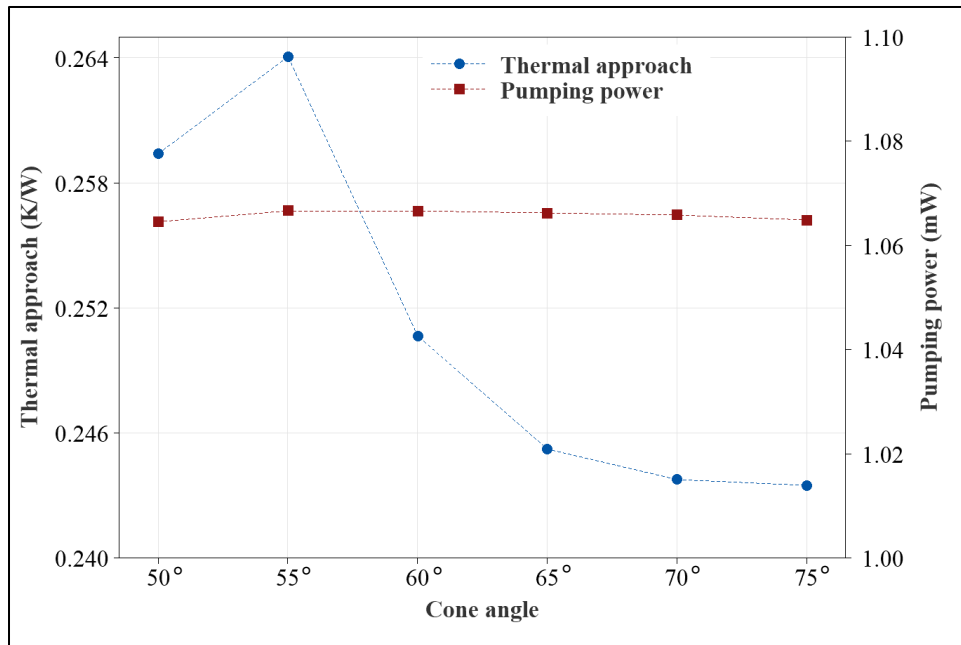


Figure 37 Variation of thermal approach and pumping power with cone angle

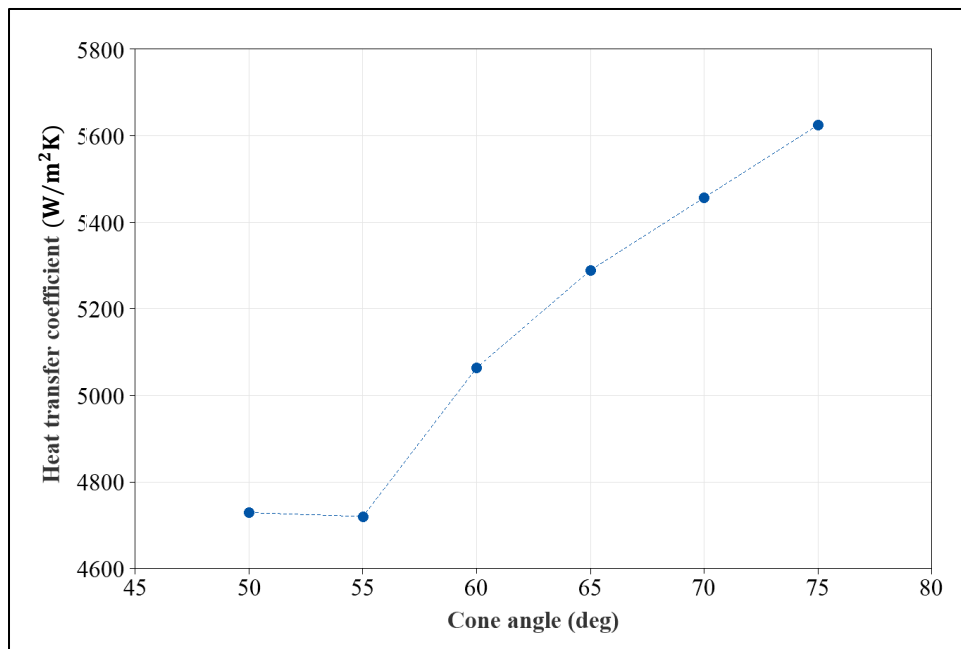
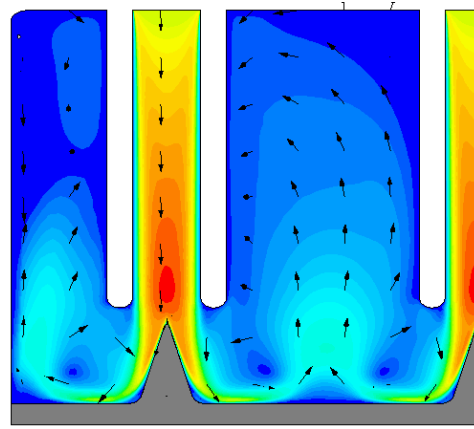
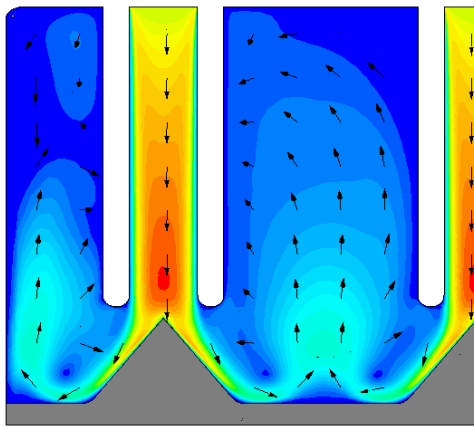


Figure 38 Variation of thermal approach and pumping power with cone angle

a) $\theta_c = 55^\circ$

b) $\theta_c = 75^\circ$



c) $\theta_c = 55^\circ$

d) $\theta_c = 75^\circ$

$T_{s,avg} = 53.6 \text{ }^\circ\text{C}$; $\sigma = 1.32 \text{ }^\circ\text{C}$

$T_{s,avg} = 51.6 \text{ }^\circ\text{C}$; $\sigma = 1.57 \text{ }^\circ\text{C}$

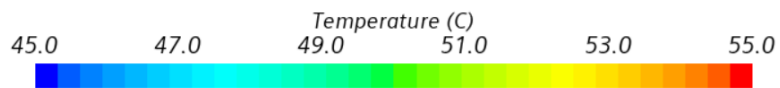
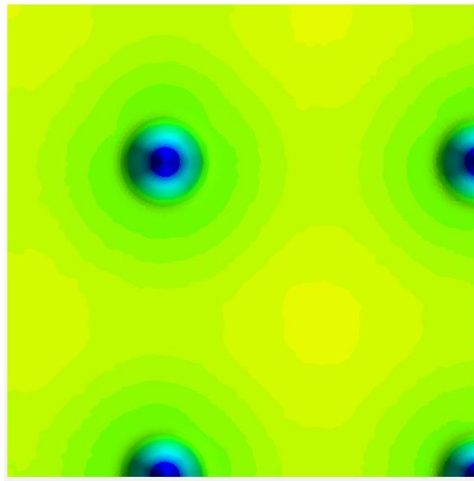
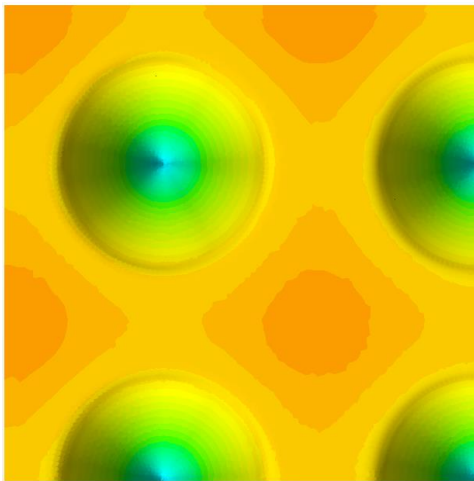


Figure 39 Velocity contours of cross section for cone angle of a) 55° b) 75° ;

Temperature contours of solid-liquid interface for cone angle of c) 55° d) 75°

5.5. Optimization analysis of conical pin fin heat sink and upper manifold

Sections 5.4.1 to 5.4.4 show the effects of various design parameters on the objective functions: thermal approach and pumping power. In addition to the above studies, the effect of tube height and extraction height on thermal approach and pumping power was studied as well. However, this effect was not found to be significant. Hence, to simplify the optimization aspect of the study, four parameters, namely: jet diameter, impingement height, cone height and cone angle were considered for both single objective and multi-objective optimization. The tube height and extraction height were fixed at 14 mm and 8.5 mm, respectively. The obtained results are discussed below.

5.5.1. *Single objective optimization of conical pin fin heat sink and upper manifold using sequential quadratic programming*

As discussed in section 4.2.3, the weighted objective function given by Equation 18 was optimized by using the ‘fmincon’ function in MATLAB Optimization toolbox. The scaling factors described in Equation 20 of the objective functions obtained using maximizing J_1 and J_2 individually are given below:

$$\max [J_1, J_2] = [SF_1, SF_2] = [0.588, 2.71]$$

Similarly, diagonal elements of the Hessian matrix were used to scale the input parameters as shown in Equation 23. The diagonal elements of the Hessian matrix obtained are given below:

$$H_{ii} = [0.1428, 6.44 \cdot 10^{-4}, 2.68 \cdot 10^{-5}, 2.29 \cdot 10^{-3}]$$

The results of the scaled objective function and design parameters obtained using sequential quadratic programming approach are shown in Figure 40. As indicated in section 4.2.3, the multi-start approach was implemented since there was no guarantee of obtaining a global maximum.

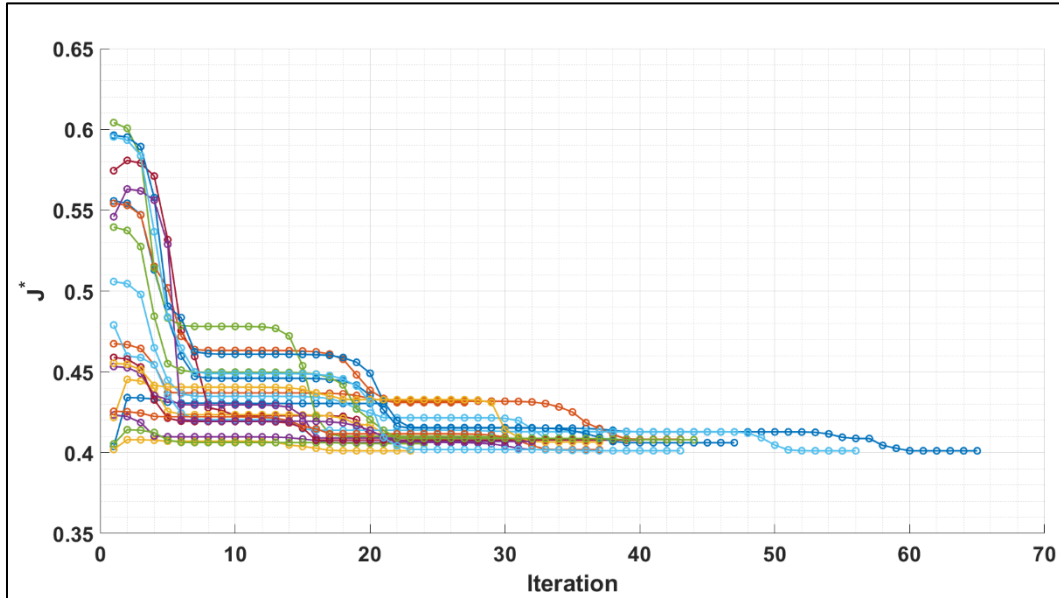


Figure 40 Single objective optimization with multi-start approach

As shown in Figure 40, although multiple local optimums were achieved, they all are significantly close to each other. The minimum value of the objective function obtained and the design vector corresponding to it are given below:

$$J^* = \lambda_1 \cdot J_1 + \lambda_2 \cdot J_2 = 0.401$$

$$\begin{bmatrix} x_1 \\ x_2 \\ x_3 \\ x_4 \\ x_5 \\ x_6 \end{bmatrix} = \begin{bmatrix} \text{Jet Diameter} \\ \text{Tube height} \\ \text{Impingement Height} \\ \text{Extraction Height} \\ \text{Cone Height} \\ \text{Cone Angle} \end{bmatrix} = \begin{bmatrix} 2.76 \text{ mm} \\ 14 \text{ mm} \\ 5.17 \text{ mm} \\ 8.5 \text{ mm} \\ 5.17 \text{ mm} \\ 73.5^\circ \end{bmatrix}$$

5.5.2. *Multi-objective optimization of conical pin fin heat sink and upper manifold using genetic algorithm*

As discussed in section 4.2.4 the scaled objective functions and input design vectors were optimized using multi-objective genetic algorithm. The result is a pareto graph of various equally acceptable design vectors. Figure 41 shows the pareto front graph obtained using multi-objective genetic algorithm approach. A design vector based on relative importance of the two objective functions thermal approach and pumping power was chosen as the optimal design.

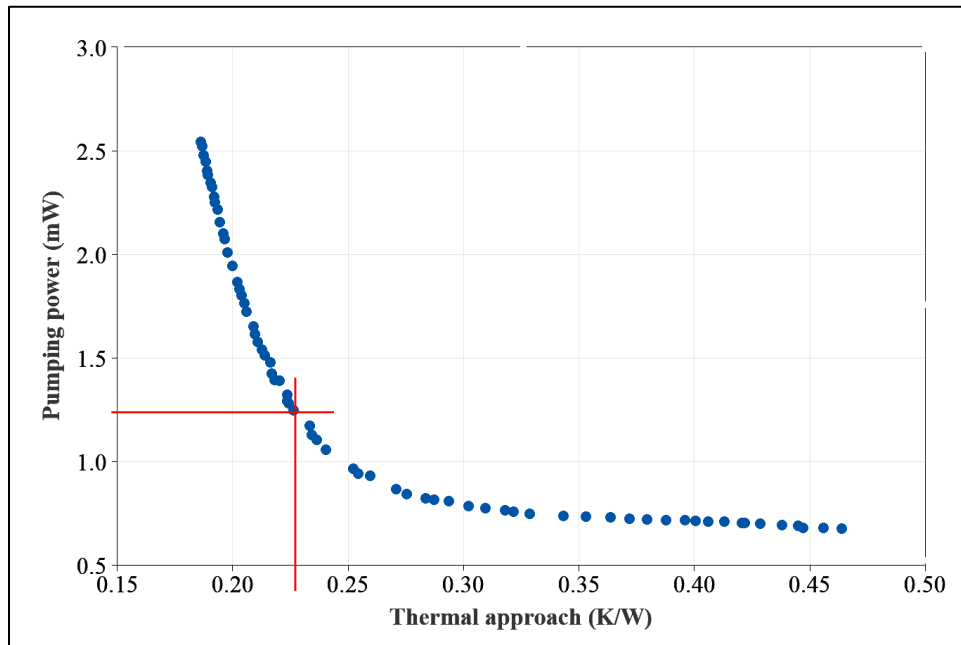


Figure 41 Pareto front of multi-objective optimization of conical pin fin heat sink

The optimal design vector chosen from the pareto graph and the corresponding objective function values are shown below

$$[J_1, J_2] = [0.234 \frac{K}{W}, 1.13 \text{ mW}]$$

$$\begin{bmatrix} x_1 \\ x_2 \\ x_3 \\ x_4 \\ x_5 \\ x_6 \end{bmatrix} = \begin{bmatrix} \text{Jet Diameter} \\ \text{Tube height} \\ \text{Impingement Height} \\ \text{Extraction Height} \\ \text{Cone Height} \\ \text{Cone Angle} \end{bmatrix} = \begin{bmatrix} 2.77 \text{ mm} \\ 14 \text{ mm} \\ 4.82 \text{ mm} \\ 8.5 \text{ mm} \\ 4.69 \text{ mm} \\ 73.6^\circ \end{bmatrix}$$

Figure 42 shows the 3D design of the optimized manifold and heat sink using the multi-objective optimization approach.

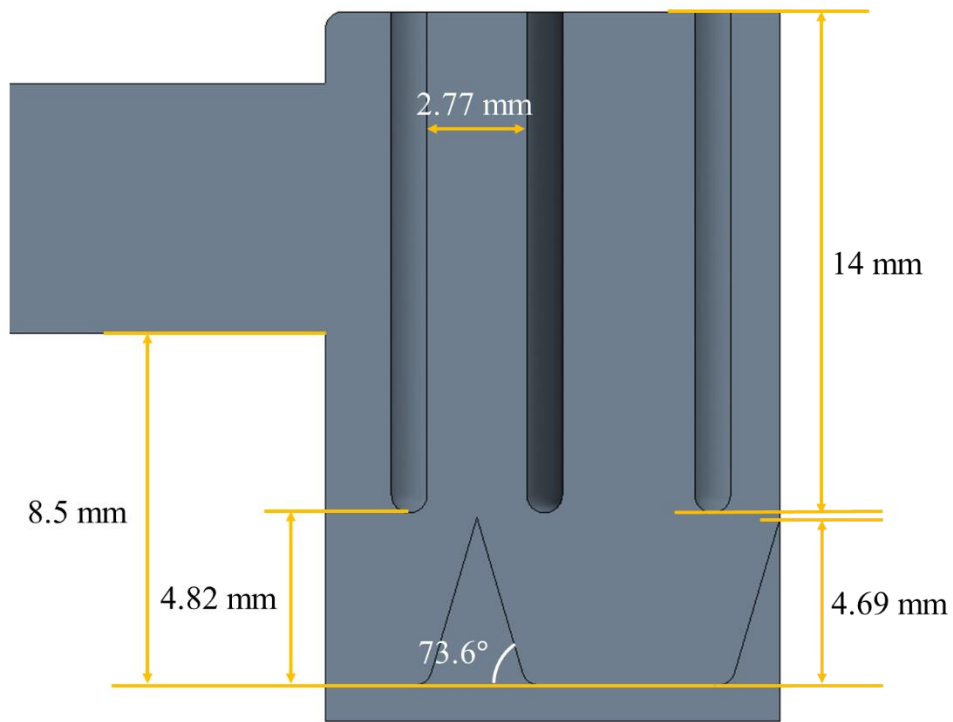


Figure 42 Optimized manifold and heat sink parameters using multi-objective genetic algorithm

After successfully finding the optimum values for the objective functions using the multi-objective genetic algorithm approach, the results were compared with sequential quadratic programming approach as shown in Table 17.

Table 17 Comparison of optimized design vectors between sequential quadratic programming and genetic algorithm approaches

Parameter	Sequential Quadratic Programming	Multi-objective genetic algorithm
Jet diameter	2.76 mm	2.77 mm
Tube height	14 mm	14 mm
Impingement height	5.17 mm	4.82 mm
Extraction height	8.5 mm	8.5 mm
Cone height	5.17 mm	4.69 mm
Cone angle	73.5°	73.6°

5.6. Comparative analysis of heat sink designs

The manifold parameters obtained in section 5.5.2 were considered for the comparative analysis of all the designed heat sinks. CFD simulations were conducted for flow rates ranging from 400 ml/min to 2000 ml/min, and heat fluxes ranging from 4 W/cm² to 36 W/cm². All the other boundary conditions were held constant as discussed in section 4.3.

Figure 43 shows the effect of volume flow rate on thermal approach for all the heat sink configurations. Thermal approach was found to reduce with increasing flow rate across the multi-jet cooling system irrespective of the heat sink configuration. This can be attributed to the increase in heat transfer coefficient with volume flow rate for the same amount of liquid-side surface area. Figure 44 shows the variation of heat transfer coefficient and Nusselt number with respect to Reynolds number. A minimum thermal approach of 0.04 K/W was achieved for a flow rate of 2000 ml/min in case of square pin fin heat sink configuration.

Another important observation which can be made from Figures 43 and 44 is the variation of thermal approach, heat transfer coefficient and Nusselt number across various heat sinks. Figure 44 shows that the maximum heat transfer coefficient and Nusselt number values are attained in case of flat plate heat sink followed by conical pin heat sink. This can be attributed to the greater momentum transfer of the fluid, which is highest in the case of flat plate heat sink.

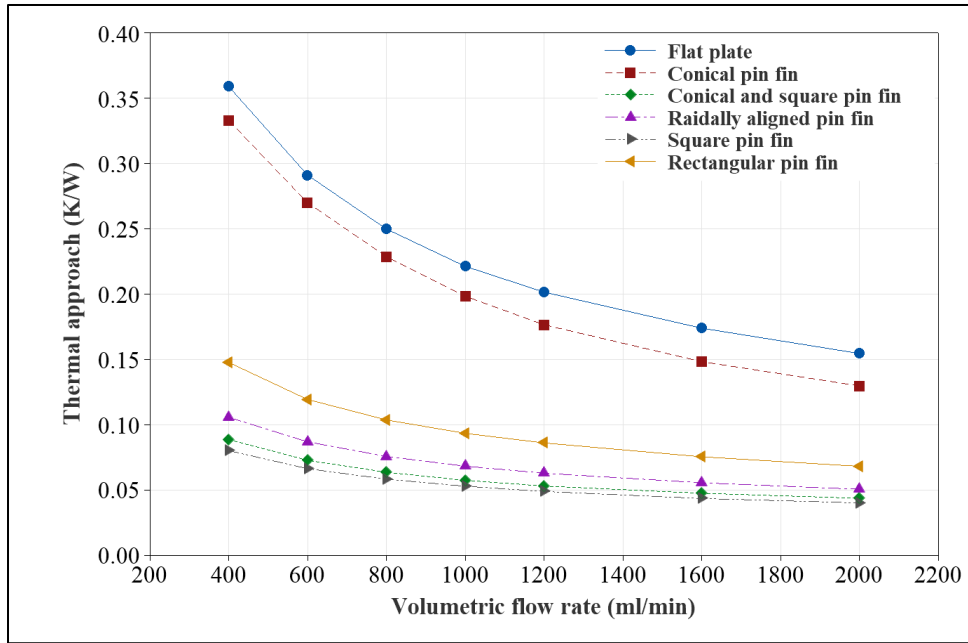


Figure 43 Variation of thermal approach with respect to volumetric flow rate

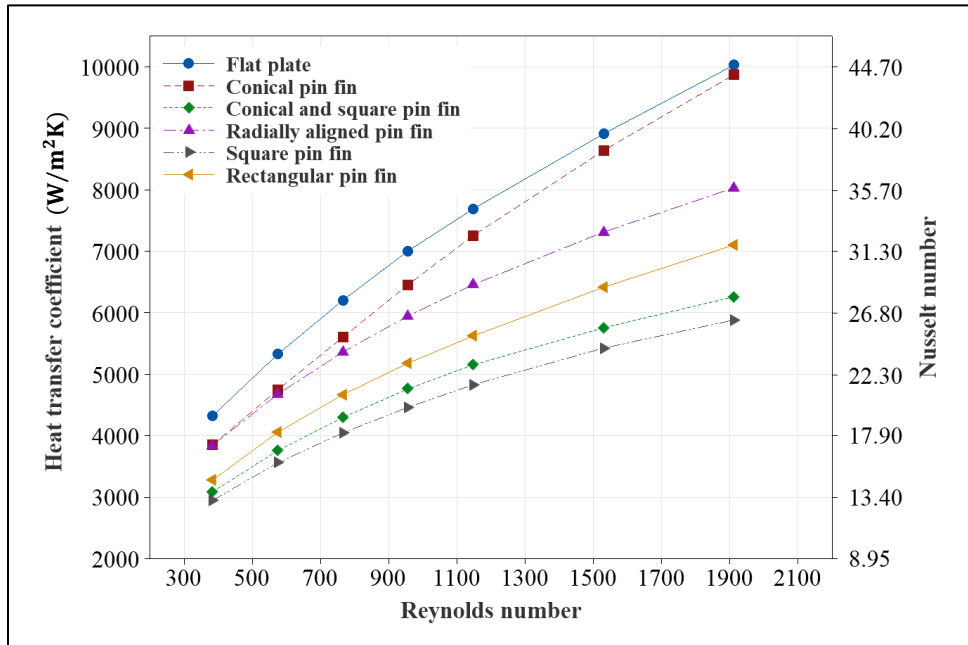
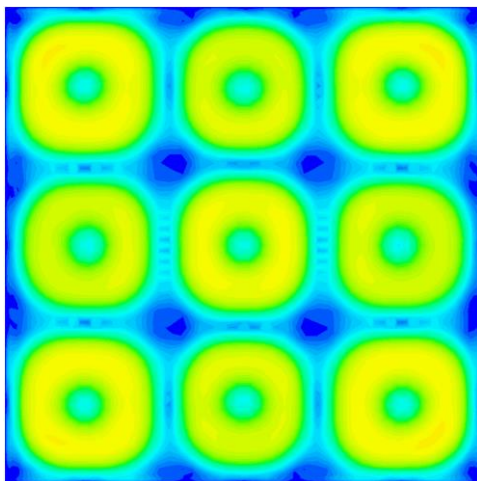


Figure 44 Variation of heat transfer coefficient and Nusselt number with respect to Reynolds number

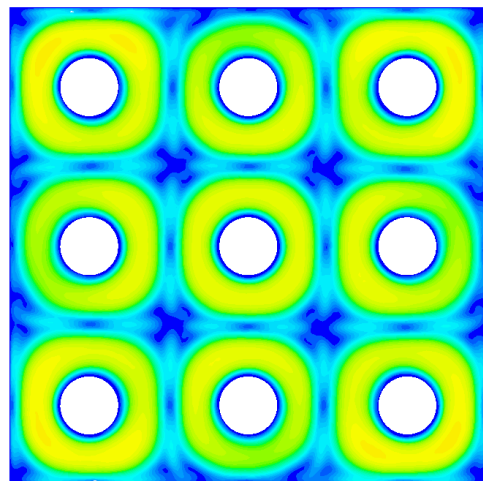
As Figures 43 and 44 show, the square pin fin case shows the lowest thermal approach and lower heat transfer coefficient among all the cases. However, since thermal approach is inversely proportional to the strength of the convective process, it is evident that the magnitude of thermal approach is inversely proportional to surface area as shown in Table 18. Hence, there are two different factors which affect the overall thermal approach of the system which are the heat transfer coefficients and liquid-side surface area.

Figure 45 shows the surface velocity contours, 0.25 mm above the base surface, for all heat sink configurations at a volumetric flow rate of 600 ml/min. The velocity contours show the obstruction to fluid flow in case of complex pin fin geometries especially square pin fin (Figure 45e), and Conical with square pin fin (Figure 45c) compared to flat plate heat sink

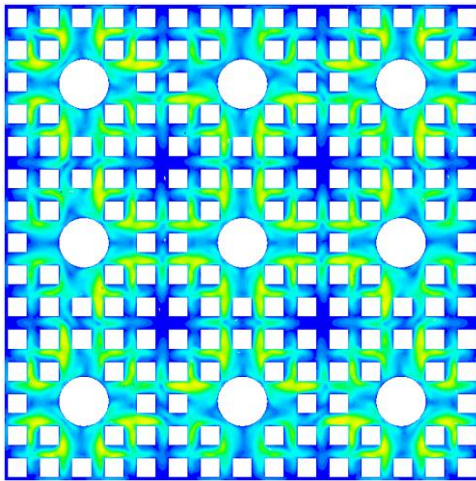
a) Flat plate



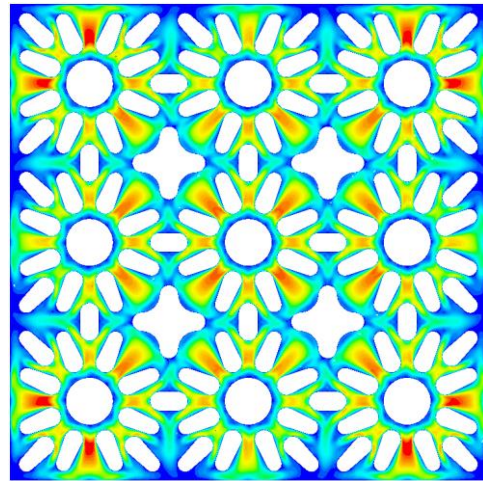
b) Conical pin fin



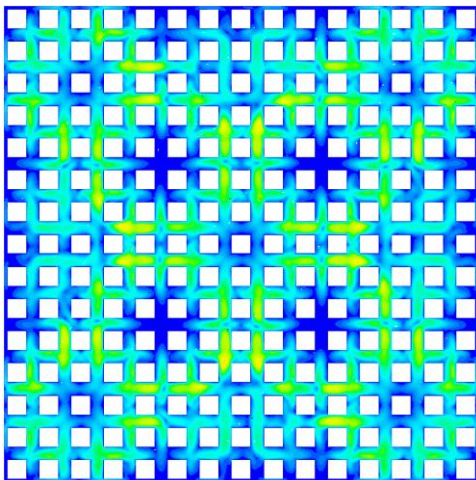
c) Conical and square pin fin



d) Radially aligned pin fin



e) Square pin fin



f) Rectangular pin fin

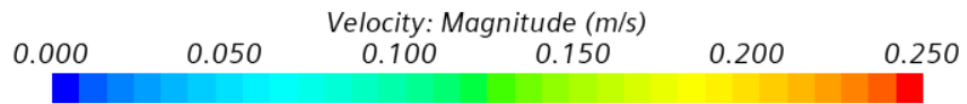
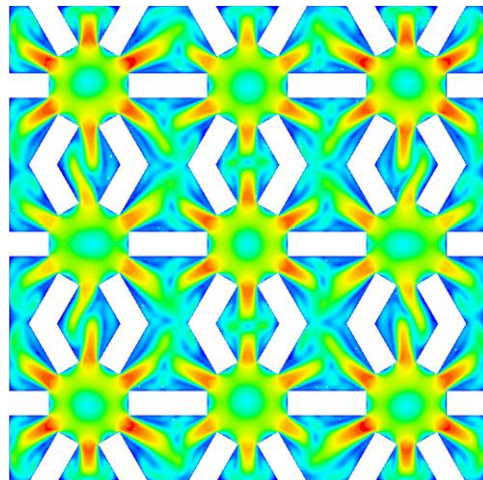


Figure 45 Surface velocity contours for different heat sink configurations for a volumetric flow rate of 600 ml/min

Table 18 shows that the average fluid velocity at a vertical distance of 0.25 mm was greater for the flat plate case than for others, which clearly indicates that the surface features (i.e., cones and pins) diminish the strength of momentum transfer near the solid interface

Table 18 Average fluid velocity and standard deviation at a vertical distance of 0.25 mm for a volumetric flow rate of 600 ml/min

Heat sink configuration	Average fluid velocity	Standard deviation
Flat plate	0.105 m/s	0.054 m/s
Conical pin fin	0.096 m/s	0.054 m/s
Conical and square pin fin	0.056 m/s	0.043 m/s
Radially aligned pin fin	0.086 m/s	0.062 m/s
Square pin fin	0.051 m/s	0.040 m/s
Rectangular pin fin	0.098 m/s	0.056 m/s

However, the lower heat transfer coefficient was compensated by increase in surface area in case of square pin fin, rectangular pin fin and radially aligned pin fin configurations. Hence, there are two different factors which affect the overall thermal approach of the system which are the heat transfer coefficients and liquid-side surface area.

To understand this effect in a better way, thermal approach, heat transfer coefficient and Nusselt number were plotted with respect to liquid-side surface area at multiple flow rates. Figure 46 shows the variation of thermal approach with liquid-side

surface area. It was found that thermal approach decreases with surface area due to the increase in convective heat transfer. However, this increase flattens out beyond a particular value. This shows that the advantage of higher surface area can only be significant until a particular value beyond which further increase is insignificant. Table 19 shows the liquid-side surface areas of different heat sink configurations discussed in this section.

Table 19 Liquid-side surface area for different heat sink configurations

Heat sink configuration	Liquid-side surface area
Flat plate (FP)	6.45 cm ²
Conical pin fin (CP)	7.81 cm ²
Rectangular pin fin (RP)	20.69 cm ²
Radially aligned pin fin (RAP)	24.66 cm ²
Conical and square pin fin (CSP)	36.64 cm ²
Square pin fin (SP)	42.45 cm ²

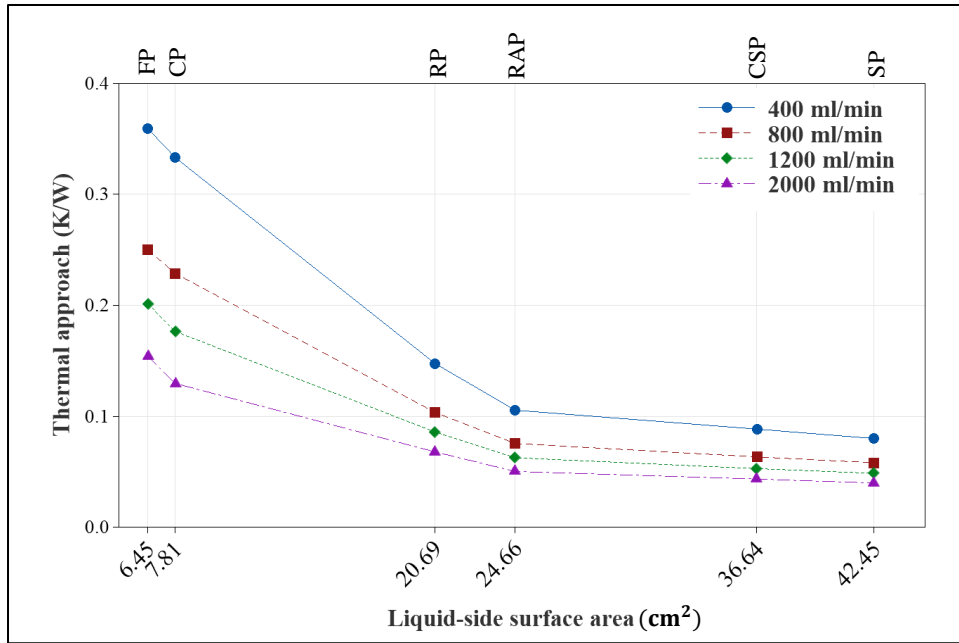


Figure 46 Variation of thermal approach with liquid-side surface area

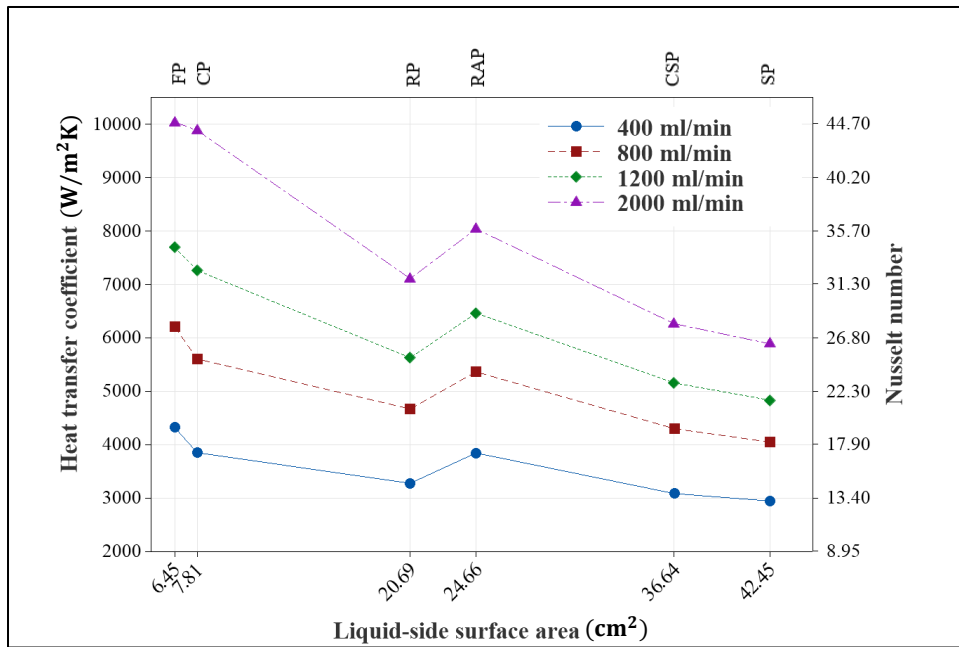


Figure 47 Variation of heat transfer coefficient and Nusselt number with liquid-side surface area

As shown in Figure 47, heat transfer coefficient and Nusselt number does not monotonically decrease with respect to liquid-side surface area. This shows the importance of design and the topology of the surface on heat transfer coefficient. A lower heat transfer coefficient can be attributed to lower surface velocities or lower momentum transfer due to the presence of fins. This can be reduced by modifying the topology of the surface.

To understand the effect of surface topology on the thermal approach, two cases a) and b) with square pins as shown in Table 20 were considered. As shown in Table 20, SP (a) consists of pin fins with a pin height of 4 mm however, the number of pins was adjusted such as to have the same surface area as that of the radially aligned pin fin (RAP). SP (b) consists of pin fins with a pin height of 2.1 mm such that the surface area is the same as of the RAP.

Table 20 Comparison of radially aligned and square pin fin configurations

Heat sink configuration	Pin height	Number of pins	Liquid-side surface area
Radially aligned pin fin (RAP)	4 mm	Cones: 9 Square pins: 99 Total: 108	24.66 cm ²
Square pin fin (SP) (a)	4 mm	121	24.66 cm ²
Square pin fin (SP) (b)	2 mm	225	24.66 cm ²

Figure 48 shows the variation of thermal approach with respect to volumetric flow rate for the configurations mentioned in Table 20 (RAP, SP (a), SP(b)).

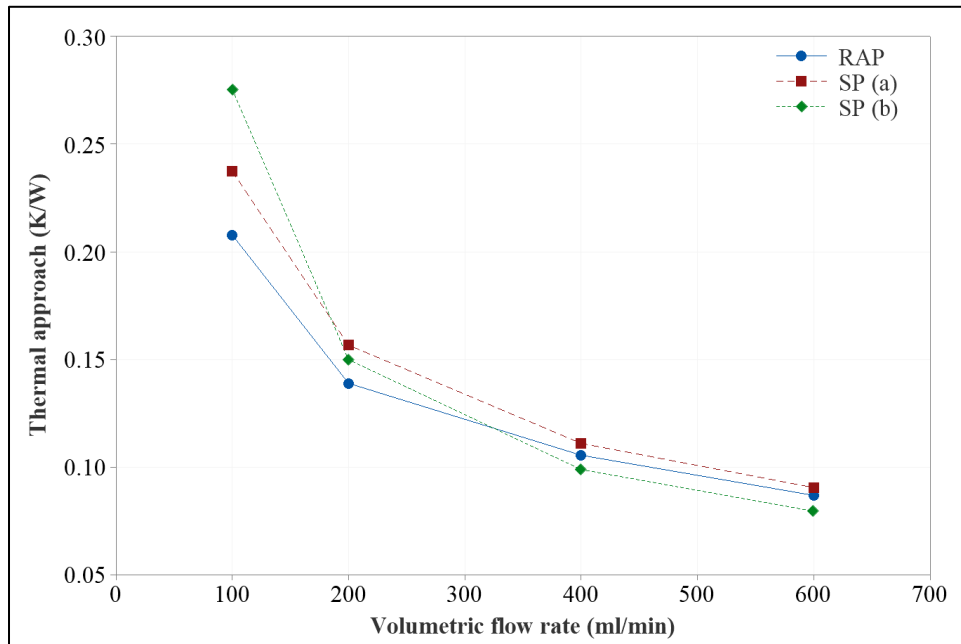


Figure 48 Comparison of radially aligned and square pin fin configurations

Figure 48 shows that radially aligned pin fin has the lowest thermal approach at lower flow rates whereas square pin fin with lower pin heights has lower thermal approach at higher flow rates. The simulation results suggest that pin orientation and alignment affect thermal performance even when the surface area is held constant.

In addition to the above, heat transfer coefficient and Nusselt number were plotted at various heat fluxes for a given volumetric flow rate as shown in Figure 49. It was observed that they did not vary by a significant amount with respect to applied heat flux.

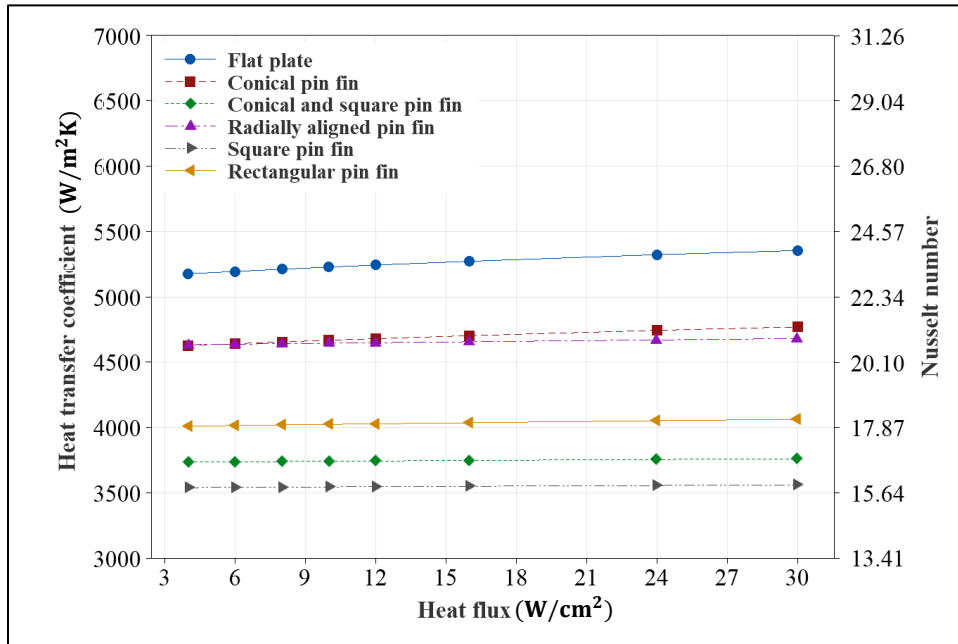


Figure 49 Variation of heat transfer coefficient and Nusselt number with input heat flux at a volumetric flow rate of 600 ml/min

In addition to the heat transfer characteristics, pumping power and friction factor were plotted as shown in Figures 50 and 51.

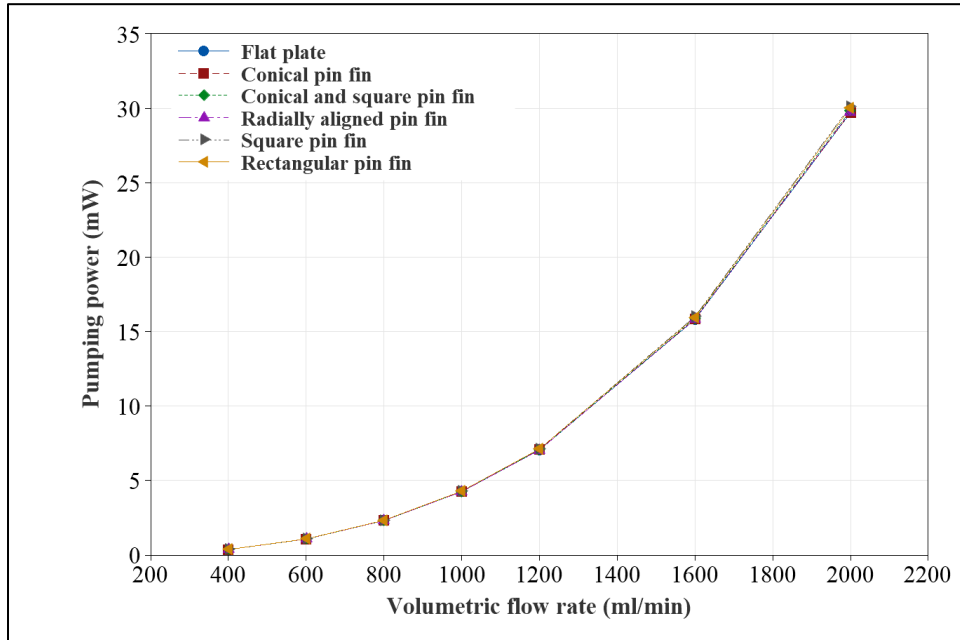


Figure 50 Variation of pumping power with respect to volumetric flow rate

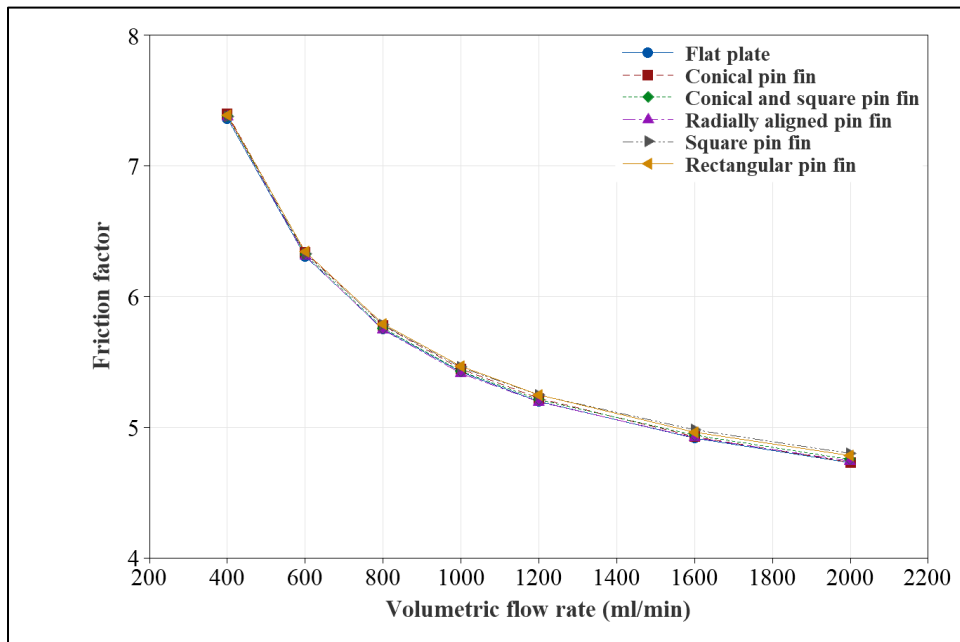


Figure 51 Variation of friction factor with respect to Reynolds number

It was observed that the variation of pumping power and friction factor with respect to various heat sink configurations is minimal. This shows that the pumping power is primarily dependent on manifold parameters.

The manufacturing cost of each heat sink is directly proportional to the volume of the heat sink. Hence it is necessary to study the nature of the normalized thermal approach, defined in section 3.2, with respect to different flow rates for all the heat sink configurations.

It can be seen from Figure 52 that the conical pin fin heat sink has a lower thermal approach than flat plate only beyond 800 ml/min.

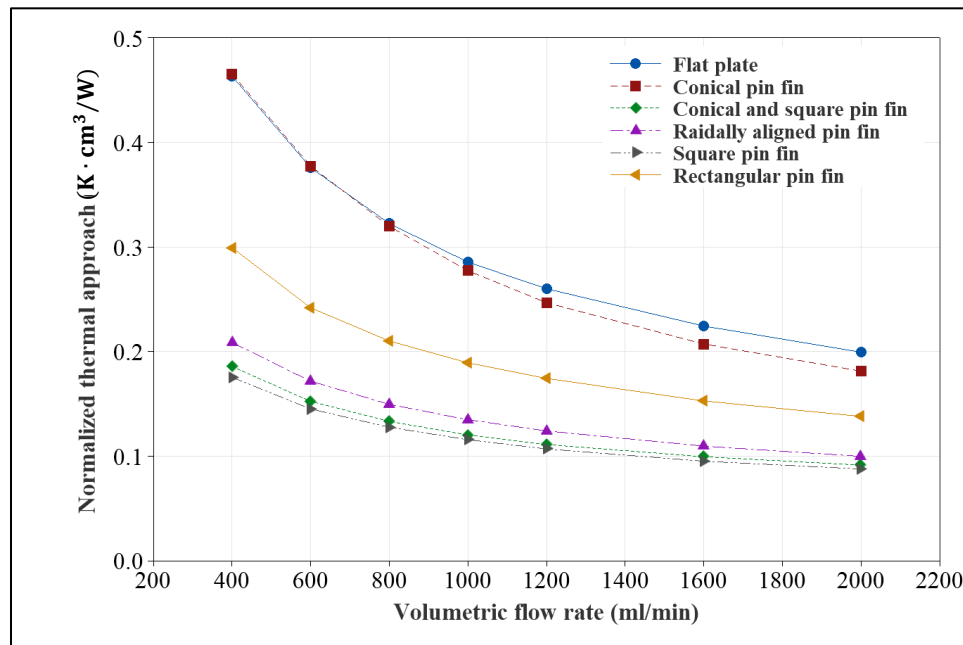


Figure 52 Variation of normalized thermal approach with respect to volumetric flow rate

This indicates that it is only beneficial to use conical pin fin heat sinks for heat transfer enhancement compared to flat plate heat sinks beyond 800 ml/min of volumetric flowrate.

Furthermore, the thermal approach enhancement factor (EF) given by Equation 33, which is the ratio of thermal approach in case of finned heat sinks to flat plate was plotted as shown in Figure 53. A maximum enhancement factor of 4.5 was achieved in case of square pin fin heat sink at a volumetric flow rate of 400 ml/min.

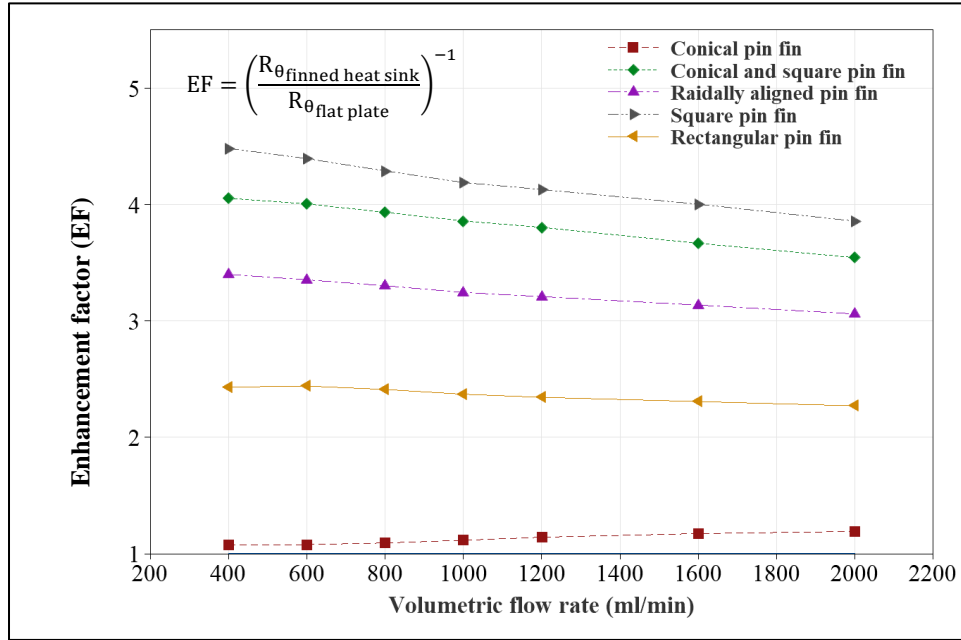


Figure 53 Variation of enhancement factor with respect to volumetric flow rate

Finally, the obtained thermal approach and pumping power results are normalized as shown in Equations 1a and 1b for all the heat sink configurations. Figure 54 shows the normalized thermal approach and pumping power of heat sinks considered as part of this study, with respect to the benchmarking data available in research papers as shown in Figure 7. The heat sink configurations considered as part of study are found to have considerably lower thermal approach and pumping power values indicating better heat transfer and fluid flow characteristics.

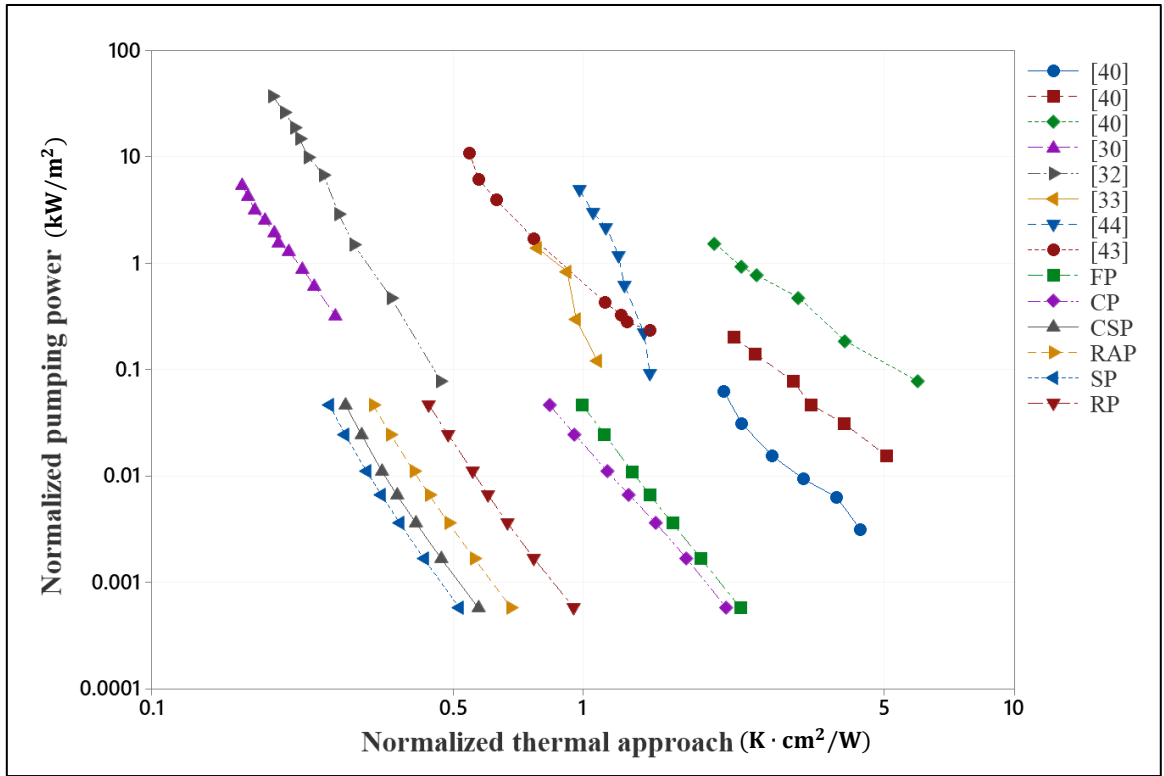


Figure 54 Comparison of normalized thermal approach and pumping with benchmarking data

5.7. Topology optimization of conical pin fin heat sink

As discussed in section 4.4, topology optimization methodology was implemented on conical pin fin heat sink. Figure 55 shows the conical pin fin heat sink after implementing the shape optimization approach.

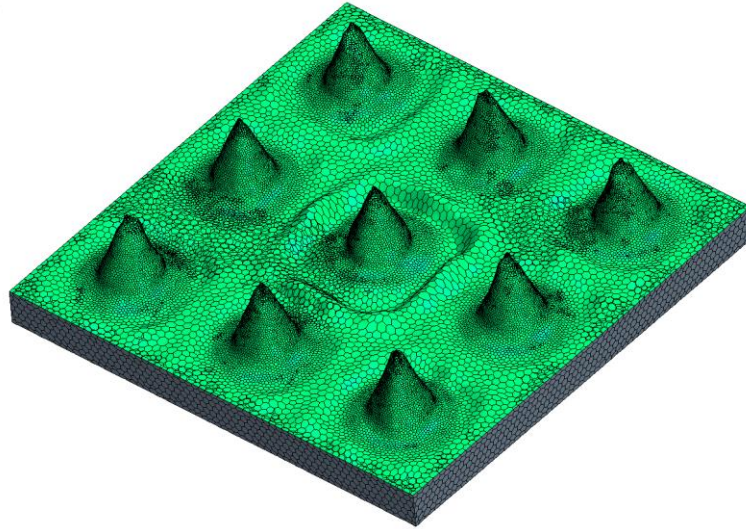


Figure 55 Topology optimized conical pin fin heat sink

Figure 56 shows the surface temperature contours of heat sink before and after shape optimization for a heat flux of 15 W/cm^2 and an inlet volumetric flow rate of 300 ml/min . As shown in Figure 56, shape optimized heat sink provides better thermal performance compared to the original configuration. An enhancement of 9.3% in thermal approach was observed with the shape optimization without any increment in pressure drop. Figure 57 shows the comparison of heat transfer coefficient along the diagonal of the heat sink bottom surface. It is evident from Figure 57 that the topology optimized geometry has higher heat transfer coefficient value compared to the original heat sink.

a) Original heat sink

b) Shape optimized heat sink

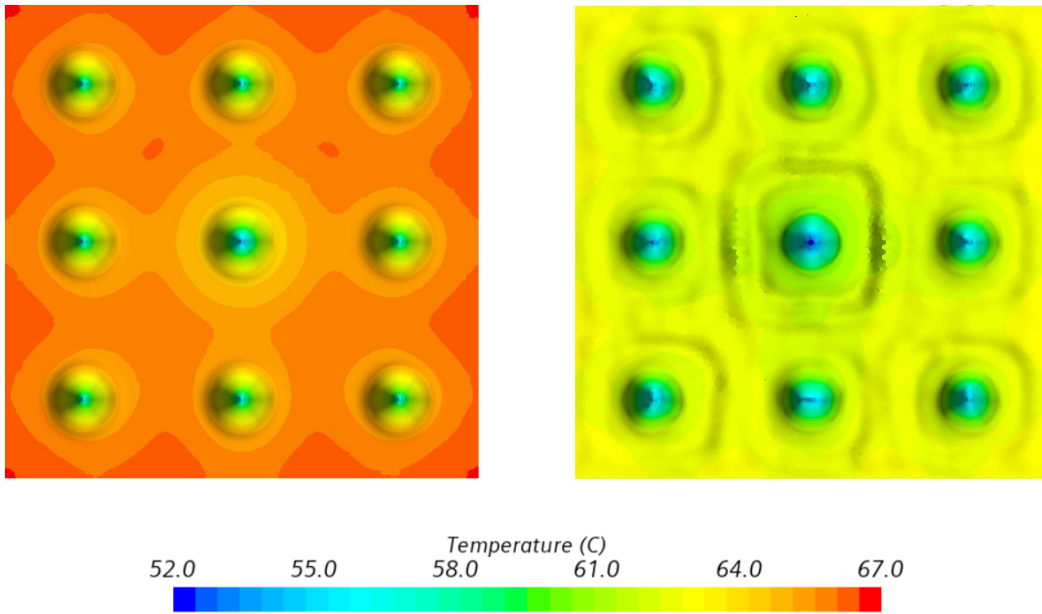


Figure 56 Surface temperature contours of topology optimized heat sink

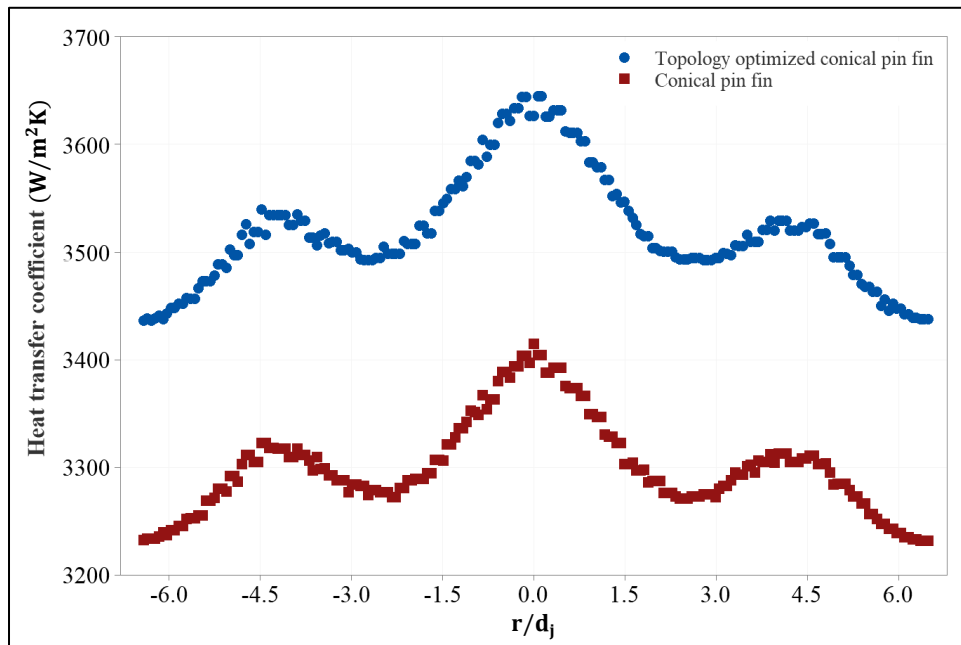


Figure 57 Comparison of heat transfer coefficient in case of topology optimized heat sink for a heat flux of 15 W/cm^2 and an inlet volumetric flow rate of 300 ml/min

6. CONCLUSIONS AND SCOPE FOR FUTURE WORK

6.1. Conclusions

The main objectives of this study were to understand the coupled effects of manifold and heat sink design parameters on heat transfer and pressure drop characteristics of a multi-jet cooling system. This was achieved by performing a design of experiments study and optimizing the design using gradient based and heuristic optimization techniques. The obtained manifold was then coupled with various heat sink configurations to understand the effects of increase in surface area and surface topology on the heat transfer characteristics. Furthermore, topology optimization was performed, and the methodology was demonstrated on the conical pin fin heat sink. The major observations as part of this study are as follows:

- The design of experiments study showed that thermal approach increases with jet diameter. However, pressure drop across the system was found to decrease with jet diameter.
- The thermal approach of the system was directly proportional to the impingement height.
- The thermal approach did not vary monotonously with cone angle and cone height. This is mainly attributed to two factors: heat transfer coefficient and surface area. Optimum values of cone height and cone angle were found at which the thermal approach was at a minimum.
- Pressure drop across the system was mainly dependent on the jet diameter as opposed to other design parameters

- Single objective optimization using sequential quadratic programming and multi-objective optimization using genetic algorithm was performed. The design vectors corresponding to the optimum configuration was found to be similar in both the cases
- Comparative analysis of heat sinks showed that the thermal approach of the system is inversely proportional to volumetric flow rate.
- Square pin fin configuration was found to have the lowest thermal approach value (0.04 K/W at 2000 ml/min) with the liquid-side surface area being the major contributing factor.
- Heat transfer coefficient was found to be the highest in case of flat plate configuration due to maximum momentum transfer. However, the thermal approach of this system was the highest since the liquid-side surface area was at its lowest in case of flat plate configuration.
- It was also observed that the topology of the surface plays a major role in momentum transfer of the fluid along the target surface thereby increasing the heat transfer coefficient.
- Enhancement factor which is the inverse ratio of thermal approach of heat sink and thermal approach of the flat plate was plotted with respect to volumetric flow rate. A maximum enhancement factor of 4.5 was achieved in the case of square pin fin configuration.

- Pumping power and friction factor were not found to vary by a significant amount with respect to heat sink configuration. The maximum pumping power was found to be 30 mW for a volumetric flow rate of 2000 LPM.
- Topology optimization of the conical pin heat sink led to a 9.3% decrease in thermal approach.

6.2. Scope for future work

- Further studies need to be conducted to understand the effect of variable pin heights in case of square pin fin and rectangular pin fin configurations
- All the CFD simulations were performed for single phase conditions with water as working fluid. However, future studies should explore the two-phase heat transfer characteristics at higher heat fluxes with other working fluids
- Different manufacturing techniques other than 3D printing should be explored in the future studies as a cost-effective way of manufacturing heat sinks with intrinsic designs
- Further topology optimization studies should be conducted and use generative design to produce thermally efficient heat sink configurations

REFERENCES

1. Electronics cooling. <https://rh.gatech.edu/news/455491/liquid-cooling-moves-chip-denser-electronics>
2. Guo, T., Rau, M. J., Vlachos, P. P., & Garimella, S. V. (2017). Axisymmetric wall jet development in confined jet impingement. *Physics of Fluids*, 29(2), 025102.
3. Garimella, S. V., & Nenaydykh, B. (1996). Nozzle-geometry effects in liquid jet impingement heat transfer. *International Journal of Heat and Mass Transfer*, 39(14), 2915-2923.
4. Ibrahim, M. B., Kochuparambil, B. J., Ekkad, S. V., & Simon, T. W. (2005). CFD for jet impingement heat transfer with single jets and arrays. Paper presented at the 359-373.
5. Forouzanmehr, M., Shariatmadar, H., Kowsary, F., & Ashjaee, M. (2015). Achieving heat flux uniformity using an optimal arrangement of impinging jet arrays. *Journal of Heat Transfer*, 137(6), 061002.
6. Wen, Z., He, Y., Cao, X., & Yan, C. (2016). Numerical study of impinging jets heat transfer with different nozzle geometries and arrangements for a ground fast cooling simulation device. *International Journal of Heat and Mass Transfer*, 95, 321-335.
7. Rau, M. J., Dede, E. M., & Garimella, S. V. (2014). *Local single- and two-phase heat transfer from an impinging cross-shaped jet*.
8. Choo, K., Friedrich, B. K., Glaspell, A. W., & Schilling, K. A. (2016). The influence of nozzle-to-plate spacing on heat transfer and fluid flow of submerged jet impingement. *International Journal of Heat and Mass Transfer*, 97, 66-69.
9. Brignoni, L. A., & Garimella, S. V. (2000). Effects of nozzle-inlet chamfering on pressure drop and heat transfer in confined air jet impingement. *International Journal of Heat and Mass Transfer*, 43(7), 1133-1139.
10. Tepe, A. Ü, Uysal, Ü, Yetişken, Y., & Arslan, K. (2020). Jet impingement cooling on a rib-roughened surface using extended jet holes. *Applied Thermal Engineering*, 178, 115601.
11. Bandhauer, T. M., Hobby, D. R., Jacobsen, C., & Sherrer, D. (2018). Thermal performance of micro-jet impingement device with parallel flow, jet-adjacent fluid removal. Paper presented at the V001T11A004.
12. Rattner, A. S. (2017). General characterization of jet impingement array heat sinks with interspersed fluid extraction ports for uniform high-flux cooling. *Journal of Heat Transfer*, 139(8), 082201.

13. Ndao, S., Lee, H. J., Peles, Y., & Jensen, M. K. (2012). Heat transfer enhancement from micro pin fins subjected to an impinging jet. *International Journal of Heat and Mass Transfer*, 55(1), 413-421.
14. Andrews, G. E., Hussain, R. A. A. Abdul, & Mkpadi, M. C. (2004). Enhanced impingement heat transfer: The influence of impingement X/D for interrupted rib obstacles (rectangular pin fins). *Journal of Turbomachinery*, 128(2), 321-331.
15. Wiriyasart, S., & Naphon, P. (2019). Liquid impingement cooling of cold plate heat sink with different fin configurations: High heat flux applications. *International Journal of Heat and Mass Transfer*, 140, 281-292.
16. Dobbertean, M. M., & Rahman, M. M. (2016). Numerical analysis of steady state heat transfer for jet impingement on patterned surfaces. *Applied Thermal Engineering*, 103, 481-490.
17. Tang, Z., Li, H., Zhang, F., Min, X., & Cheng, J. (2019). Numerical study of liquid jet impingement flow and heat transfer of a cone heat sink. *International Journal of Numerical Methods for Heat & Fluid Flow*, 29(11), 4074-4092.
18. Ramphueiphad, S., & Bureerat, S. (2018). Synthesis of multiple cross-section pin fin heat sinks using multiobjective evolutionary algorithms. *International Journal of Heat and Mass Transfer*, 118, 462-470.
19. Husain, A., Kim, S., & Kim, K. (2013). Performance analysis and design optimization of micro-jet impingement heat sink. *Heat and Mass Transfer*, 49(11), 1613-1624.
20. Shah, B. G. Sammakia, H. Srihari, & K. Ramakrishna. (2004). *A numerical study of the thermal performance of an impingement heat sink-fin shape optimization*
21. Yang, L., Min, Z., Parbat, S. N., & Chyu, M. K. (2017). Optimization of hybrid-linked jet impingement cooling channels based on response surface methodology and genetic algorithm. Paper presented at the V05AT11A002.
22. Ndao, S., Peles, Y., & Jensen, M. K. (2009). Multi-objective thermal design optimization and comparative analysis of electronics cooling technologies. *International Journal of Heat and Mass Transfer*, 52(19), 4317-4326.
23. Yildizeli, A., & Cadirci, S. (2020). Multi-objective optimization of multiple impinging jet system through genetic algorithm. *International Journal of Heat and Mass Transfer*, 158, 119978.
24. Yang, Y., & Peng, H. (2008). Numerical study of pin-fin heat sink with un-uniform fin height design. *International Journal of Heat and Mass Transfer*, 51(19), 4788-4796.

25. Dede, E. M., Joshi, S. N., & Zhou, F. (2015). Topology optimization, additive layer manufacturing, and experimental testing of an air-cooled heat sink. *Journal of Mechanical Design*, 137(11), 111403.
26. Koga, A. A., Lopes, E. C. C., Villa Nova, H. F., Lima, C. R. d., & Silva, E. C. N. (2013). Development of heat sink device by using topology optimization. *International Journal of Heat and Mass Transfer*, 64, 759-772.
27. Negi, D. S., & Pattamatta, A. (2015). Profile shape optimization in multi-jet impingement cooling of dimpled topologies for local heat transfer enhancement. *Heat and Mass Transfer*, 51(4), 451-464.
28. E. M. Dede. (2010). Multiphysics optimization, synthesis, and application of jet impingement target surfaces. Paper presented at the - *2010 12th IEEE Intersociety Conference on Thermal and Thermomechanical Phenomena in Electronic Systems*, 1-7.
29. T. Wei, H. Oprins, V. Cherman, J. Qian, I. De Wolf, E. Beyne, & M. Baelmans. (2019). *High-efficiency polymer-based direct multi-jet impingement cooling solution for high-power devices*.
30. T. Brunschwiler, H. Rothuizen, M. Fabbri, U. Kloter, B. Michel, R. J. Bezama, & G. Natarajan. (2006). Direct liquid jet-impingement cooling with micron-sized nozzle array and distributed return architecture. Paper presented at the - *Thermal and Thermomechanical Proceedings 10th Intersociety Conference on Phenomena in Electronics Systems, 2006. ITherm 2006*. 196-203.
31. K. Gould, S. Q. Cai, C. Neft, & A. Bhunia. (2015). *Liquid jet impingement cooling of a silicon carbide power conversion module for vehicle applications*.
32. T. Acikalin, & C. Schroeder. (2014). Direct liquid cooling of bare die packages using a microchannel cold plate. Paper presented at the - *Fourteenth Intersociety Conference on Thermal and Thermomechanical Phenomena in Electronic Systems (ITherm)*, 673-679.
33. Whelan, B. P., Kempers, R., & Robinson, A. J. (2012). A liquid-based system for CPU cooling implementing a jet array impingement waterblock and a tube array remote heat exchanger. *Applied Thermal Engineering*, 39, 86-94.
34. J. Robinson, W. Tan, R. Kempers, J. Colenbrander, N. Bushnell, & R. Chen. (2017). A new hybrid heat sink with impinging micro-jet arrays and microchannels fabricated using high volume additive manufacturing. Paper presented at the - *2017 33rd Thermal Measurement, Modeling & Management Symposium (SEMI-THERM)*, 179-186.
35. Y. Han, B. L. Lau, G. Tang, X. Zhang, & D. M. W. Rhee. (2017). *Si-based hybrid microcooler with multiple drainage microtrenches for high heat flux cooling*.

36. E. G. Colgan, B. Furman, M. Gaynes, W. S. Graham, N. C. LaBianca, J. H. Magerlein, R. R. Schmidt. (2007). *A practical implementation of silicon microchannel coolers for high power chips.*
37. Y. Han, B. L. Lau, X. Zhang, Y. C. Leong, & K. F. Choo. (2014). *Thermal management of hotspots with a microjet-based hybrid heat sink for GaN-on-si devices.*
38. Kim, S. H., Shin, H., & Kim, S. (2019). Numerical study on cooling performance of hybrid micro-channel/micro-jet-impingement heat sink. *Journal of Mechanical Science and Technology*, 33(7), 3555-3562.
39. Wu, R., Hong, T., Cheng, Q., Zou, H., Fan, Y., & Luo, X. (2019). Thermal modeling and comparative analysis of jet impingement liquid cooling for high power electronics. *International Journal of Heat and Mass Transfer*, 137, 42-51.
40. J. Jörg, S. Taraborrelli, G. Sarriegui, R. W. De Doncker, R. Kneer, & W. Rohlf. (2018). *Direct single impinging jet cooling of a mosfet power electronic module.*
41. T.-W. Wei, H. Oprins, V. Cherman, Z. Yang, K. Rivera, G. Van der Plas, . . . M. Baelmans. (2020). Demonstration of package level 3D-printed direct jet impingement cooling applied to high power, large die applications. Paper presented at the - 2020 *IEEE 70th Electronic Components and Technology Conference (ECTC)*, 1422-1429.
42. M. Tsunekane, & T. Taira. (2007). *Design and performance of compact heatsink for high-power diode edge-pumped, microchip lasers.*
43. R. Skuriat, & C. M. Johnson. (2008). Thermal performance of baseplate and direct substrate cooled power modules. Paper presented at the - 2008 4th IET Conference on Power Electronics, Machines and Drives, 548-552
44. Olesen, K., Bredtmann, R., & Eisele, R. (2006). "ShowerPower" New Cooling Concept for Automotive Applications.
45. N. Pundir, "Experimental Investigation of multi-jet impingement cooling system with optimized heat sinks," M.S. thesis, Texas A&M University, 2021.
46. Star-CCM+. <https://support.sw.siemens.com/documentation>
47. Liu, Z., Li, W., & Yang, M. (2015). Two general extension algorithms of latin hypercube sampling. *Mathematical Problems in Engineering*, 2015, 450492.
48. Procedure for estimation and reporting of uncertainty due to discretization in CFD applications. (2008). *Journal of Fluids Engineering*, 130(7), 078001.